UNIVERSITÀ DEGLI STUDI DI BERGAMO
SCHOOL OF ENGINEERING
DEPARTMENT OF ENGINEERING AND APPLIED SCIENCES
DOCTORAL PROGRAMME IN ENGINEERING AND APPLIED SCIENCES

OPTIMIZATION OF SOLAR THERMAL POWER PLANTS

Doctoral Dissertation of:
Elisa Ghirardi

Supervisor:
Prof. Giuseppe Franchini

The Chair of the Doctoral Program:
Prof. Valerio Re

2020 – XXXIII

Abstract

The energy demand expected increase and the even more impacting greenhouse effect promote many effort to increase the renewable contribute in several electric markets and is expected to increase further in the next years. The increasing penetration of PV and wind energy, that are for definition unpredictable and variables, in several markets is forcing the power plants (both fossil and renewable) to operate with a high level of flexibility and a high dispatchability is becoming a requirement as important as a low price. In spite of a higher LCOE, Concentrated Solar Power (CSP) plants are recognized as the favorite way to produce electricity thanks to the availability of an embedded long-term storage system that allows supplying thermal energy when the irradiation is low (or fluctuating) and can extend (or shift) the operation of the plant according to the power demand variability.
This thesis proposes the assessment of the central receiver system (CRS), considered the best option over CSP technologies. Nevertheless, many aspects still penalize the tower systems, mainly the higher installation costs and the lower energy density. The optimal design of the heliostat layout and the selection of the optimal geometrical/design parameters (tower height and receiver dimensions, among all) are fundamental to improve the performance of CRS, independently of the operation mode of the plant (connected or not to the grid). The implementation of a complete code for the design and the simulation of the heliostat field has enabled detailed optimization; changing the design period and the objective function is possible to handle the production flexibility. It was found that the shape of the heliostat field, according to a different design solar altitude, highly influences the seasonal trend of the efficiency. Assuming March solar noon as a design condition ensures a more constant efficiency throughout the year and guarantees the minimum LCOE. Also, the receiver

shows a great influence, especially for small plants where the cavity configuration allows to reduce the investment cost; however, the efficiency is maximized in the summer season and a strong penalty takes place in winter months.

Successively, the capacity of a solar tower system operating in island-mode to fulfill the power demand is investigated, compared with the most mature PTC technology. The detailed analysis of the first part has been applied to evaluate the load-following capability of the CSP system. The implemented algorithm determines the best combination of solar field, thermal storage and power block to meet two different profiles of demand. The CRS exhibits better dispatchability properties: the aperture area and the investment cost are minimized for both the load.

Finally, the integration of the CRS is investigated in a fully renewable production system (PV + Wind turbines + CSP) where 90% of the load must be satisfied. It was proved that, in the more viable solution, the CSP provides a typical base-load supply, thanks to the low-cost storage, whilst the PV and WF have a marginal contribution, as peaking plants, but contribute to limit the LCOE rising.

Contents

Introduction

Energy is one of the most prominent human needs (together with water) but today the electricity production account for 35% of overall GHG emission [1]. The growing energy demand and more rigorous environmental constraints are leading the power production sector to increase the share of renewable energy sources. The utilization of solar energy has grown significantly in the last decades, especially thanks to the photovoltaic technology [2]. The development of PV has contributed to reduce the solar electricity cost. Nevertheless, when the grid requires a more dispatchable production, PV plants become critical because of a difficult modulation of the power production, as well shown by Gauché et al. [3] and Quaschning [4]. The necessary flexibility can be guaranteed only through systems with energy storage. Concentrated Solar Power (CSP) plants generally have embedded Thermal Energy Storage (TES) systems, which result more affordable if compared to batteries [5]. Despite of a LCOE currently higher than PV, Report EIA 2018 [6] indicates Concentrated Solar Power plants as the most promising solar technology. CSP plants can ensure a smooth and dispatchable power on-demand even when the irradiation is scarce or fluctuating, as documented by Magrassi et al. in [7], avoiding excessive stresses on the grid due to demand peaks [8]. Furthermore, CSP plants operate similarly to traditional fossil-fuel power generation plants (with a power block based on a steam Rankine cycle) allowing Combined Cooling, Heating and Power (CCHP) solutions: thus solar radiation can be converted into final energy with a high overall efficiency, improving the competitiveness of CSP systems, as proved by Khaliq [9] and Ravelli et al. [10].

Recently, many efforts are voted to increase the competitiveness of CSP, first of all the project for a new generation of CSP (CSP GEN3) of NREL and SANDIA laboratories; their goal of improving efficiency and reducing component

cost includes increasing solar circuit temperatures beyond 700°C and replacing the steam turbine with a supercritical CO_2 Brayton cycle [11]. However, in the vision of Internet of Energy, it is underlined that the high investment cost is considered acceptable in context with high renewable penetration and the dispatchability becomes the priority of the grid [12]. This thesis has studied in detail the behavior of the CSP and how it is possible to influence it, for different operating conditions; particular attention is given to production flexibility in order to include the plant as the main source of electricity, in a completely renewable scenario or for isolated applications where the only objective is to satisfy demand.

Among the CSP plant configurations, the Central Receiver System (CRS, also called Solar Tower) is the option with the highest potential [13]. Brumana et al. in [14] showed that CRS perform better than linear systems (Parabolic Trough Collectors, PTC) in isolated or weakly interconnected grids. This is due to higher operating temperatures (ensuring a higher cycle efficiency) and smaller seasonal variations in the solar-to-thermal efficiency. The main constraint of CRS plants remains the high investment cost, that nowadays is limiting the tower plants to large-scale and high-irradiance-level applications, as reported by Singhai et al. in [15] and [16]. Although the level of solar irradiance has a huge impact on the power generation costs [17], decreasing the capital costs remains the main road to lower the LCOE. As reported in the analysis of Telsnig et al. [18], the solar field represents up to 50% of the total investment and reducing the heliostat cost could be crucial, as documented by Emes et al. in [19]. Moreover, the heliostat field is the subsystem with the highest energy losses, typically more than 40% [20]. Despite several models available in the literature (as reported in the review carried out by Barberena et al. in [21]), the procedure to obtain the optimal design of the heliostat field is still an open question. With the aim of increasing the competitiveness of the CRS, the critical points of technology are addressed in first place. Some authors suggested new system configurations to enhance the field efficiency, like the multi-tower configuration proposed by Arbes [22], the secondary receiver investigated by Kiwan and Khammas [23] and Schöttl et al. [24], or the field distribution on a hillside terrain [25]. All these solutions lead to limited efficiency improvement, but significant reduction of investment costs. Many studies have demonstrated that improve the heliostat efficiency can enhance by 10% the energy delivered by the field [26]. Since the best layout is a trade-off of the losses occurring in the ray path from the sun to the receiver (shading, blocking and the other optical factors), different solutions could lead to very similar results in terms of overall efficiency, as reported by Collado and Guallar in [27].

The best configuration of the heliostat field must include the tower-receiver subsystem to maximize the energy conversion efficiency: in fact, Yu et al. in [28] showed how coupling the two systems plays a fundamental role in the

conversion from radiative to thermal power. The optimization of the whole system is often considered too expensive and several codes focus on a reduced set of variables. Saghafifar and Gadalla [29] proposed a field layout optimization according to different patterns (spiral or radial staggered). Farges et al. [30] studied the optimization of the heliostat geometry, given the dimensions of tower and receiver. Srilakshmi et al. Sometimes investigated the optimization of the tower height for given heliostat layouts in [31]. Only few works explicitly include tower and receiver dimensions in the optimization of the layout pattern, like Carrizosa et al. in [32]. A complete approach is presented by Collado in [33], where a double-step optimization process leads to the design of the whole solar field minimizing the LCOE. To improve the plant design, it is important to detect which are the main factor affecting the field efficiency [34]. The first aim of this thesis is to identify the critical variables and their influence on the optimum layout; particular attention is given to:

- the effect of the design periods on the performance throughout the year.
- the consequence of different target function during the optimization.
- the assessment of the best heliostat size, according with an economic evaluation.
- the design of the receiver for a pre-determined solar field, respecting physical and economic constraints.

A new model for optimizing and simulating solar tower plants, based on an in-house Matlab® code, has been developed and validated. The main geometrical parameters of the tower system are varied during the design process in order to maximize the efficiency and considering the cost of each component, the minimization of the cost of electricity (i.e. LCOE) could help to increase the development of the CRS system. The analysis has been carried out for two field sizes comparable with a small standalone application (almost 5 MW_e) and with a commercial scale plant (greater than 100 MW_e).

Despite the low level of LCOE of photovoltaic represent an attractive solution, Cole et al. highlight that increasing the capacity of non-dispatchable system will require a different approach for the balance of the electricity grid [35]: a production system that ensure a sufficient flexibility is preferable to a cheapest, especially in the MENA region where a smart grid technology is not yet implemented, as remind by Okedu and Salmani in [36]. The storage system for PV stationary application is still not competitive with the thermal energy storage, despite the recent batteries cost reduction, as depicted by IRENA [37]. As already mentioned, the beneficial effect of TES represent a key factor for the adoption of CSP in the production system; moreover, the reliability

of the associated energy facilitated the integration of other non-programmable renewables, such as solar PV and wind turbines. In this way the global share of green power plants is increased [38]. The second aim of this work is to assess the potential of CRS system under different operative condition and with particular stress on the load-following capability: the ability to instantly meet the electric demand of a district or a region. The analysis provided by Chen et al. [39] underlines that the design of a central receiver system and the interaction of each subsystem (solar field + receiver + storage + power block) is non trivial and different opinion about design condition or the solar multiple (SM) are present in literature. Luo et al. define 12 parameters for the design of the whole system and with a sensitivity analysis the interaction between the subsystem is defined: the capacity of the storage and the solar multiple are the only parameters that are strictly related [40]. Awan et al. [41] developed a method to maximize the produced energy, minimizing the LCOE, of a CRS system by changing the value of SM and storage. A combined optimization of genetic and teaching learning algorithms is used by Khosravi et al. [42] to determine the best design point DNI together with the sizing parameters. Some authors pointed out on the importance of the dispatch strategies, such as Wagner et al. [43] that determine the TES utilization in order to ensure the best operation, depending on weather and market prices.

Due to limited and inadequate capacity of the infrastructures for generation and transmission with fossil fuel, blackouts are frequent in MENA and the capacity expansion of renewable is more important with the rising power demand. The adoption of hybrid renewable energy systems (HRES) is the only way to consistently reduce the fossil contribution and results to be more suitable especially in application where the extension of the grid connection is not feasible [44]. The hybrid generation of electricity starts from small application in very isolated location such as the communication tower or the temporary facilities of non-governmental organization (NGO), typically powered by a Diesel genset coupled with photovoltaic field and battery [45], until large scale project like The RedSea resort [46], in the Kingdom of Saudi Arabia, with 100% carbon neutrally electricity production with high level of energy storage.

The variability of the resources forces a more accurate design process where the performance prediction and the size of the component become crucial. In the second part of this thesis, different configurations of renewable systems are compared to reduce the contribute of fossil fuel to 10% of the electric demand. The main objective of the study are to:

- Analyze the load-following capability of CRS system for installation in island-mode
- Evaluate the capability of CRS system in a power mix system (with PV, wind turbine and batteries)

For all the case considered, a detailed optimization has been provided to determine the optimal field size (for the three technologies), storage capacities (TES and batteries) and nominal power of the steam turbine to minimize the LCOE of the plant and ensuring the balance between energy supply and demand. Aware that the severe penalty of efficiency due to partial load and the not rapid ramp rate, the steam Rankine cycle has been adopted in this thesis according to the most diffuse commercial CSP configuration. However, since the work is focused on the solar field operation, an ideal load-following capability of the turbine has been supposed, and only off design considerations on the efficiency are treated.

Part I

Heliostat field layout optimization

CHAPTER 1

Central receiver system performance model

1.1 Introduction

In recent years, several frameworks were proposed for the field generation, including the most acclaimed ones such as DELSOL3, Campo code, MUEEN algorithm and heliostat minimum radial spacing. Saghafifar et al. [47] showed that a pattern-free strategy leads to a more irregular field and maintenance operations become more difficult. Furthermore, this approach is highly time consuming since the coordinates of each mirror have to be optimized, as reported by Carrizosa [48]. To make the problem less complex, a geometrical pattern is frequently imposed: Lutchman et al. [49] showed that the arrangement of the entire field is possible with a set of few variables. In that way, Les et al. [50] conclude that the resulting layout "is more suitable to real plants". Pattern strategies are usually preferred and one of the most reliable methods is the radial staggered: Collado and Guallar [51] have shown the strength and the consistency of this method. Compared to free variable optimization, the pattern distribution leads to a slightly reduced optical efficiency, as proved in [52] by Carrizosa et al., but the computational cost is much lower as Kim et al. documented in [53]. Besarati and Yogi Goswani proposed in [54] a methodology to attenuate the rigidity of this method: the patterns are applied to an over-sized field and then the most efficient heliostats are selected.

In the comparative review of the existing codes for the assessment of the he-

liostat fields carried out by Garcia et al. [55] two different methodologies are presented: ray-tracing and integration (fully analytical) methods. The former requires a high computational effort. The performance of the field is statistically approximated with the behavior of a random set of solar rays: as reported by Huang and Yu in [56], a huge number of rays must be considered to ensure a good accuracy. Analytical methods assume that the ray behavior can be approximated with a normal distribution, resulting from the superposition of each optical error [57]. In a complete review of optimization algorithms [58], Cruz et al. conclude that the best method depends on the aim of the work, given the time consuming restrictions. In an optimization study the performance of thousands of different layouts must be evaluated: the selected method must be as simple and as fast as possible, by sacrificing the accuracy of more detailed models [59]. Only when a more realistic forecast of the plant operation is required, a modification of the analytical method is suggested [60]. Due to the computational constraints, some simplifications are often necessary, limiting the accuracy of the simulation. Lipps [61] and analogously Kistler [62] proposed a zoning approach in the eighties. The heliostat field is divided into cells and the optimization is based on the efficiency evaluated in the center of each cell [63]. The annual performance of each heliostat does not depend only on the solar time and its own position and orientation, but also on the relative location of the neighboring heliostats, which cause shadows and blocking [64]. The shading and blocking factor is the most computationally expensive parameter [53] and one of the main sources of losses of a non-optimized layout [59]. Two different approaches were introduced for the calculation of the block and shadow losses: the projection method, developed by Sassi in 1983, and the heliostat discretization method. The Sassi's method [65] has been widely used in many applications, but some assumptions, like the heliostat parallelism, compromise the accuracy of the model [66]. More recently, some authors, like Cruz et al. in [60], propose some modifications of analytical methods to make the performance prediction more accurate. Wang et al. suggested a more reliable method for the evaluation of the shading and blocking factor [67]. Eddhibi et al. [68] showed the impact of shading and blocking losses on the field design and the influence of atmospheric extinction is analyzed in detail by Polo [69].

The total energy delivered by the field is affected by the heliostat positions, but Gadalla and Saghafifar documented the strong influence of the target point geometry [70] and the receiver thermal losses (convective and radiative) proportional to the absorbing area, can be significant. The receiver operation is limited by the maximum allowable flux limit, generally about of 1-1.2 MW/m^2 [71] and the evaluation of receiver performance must include the flux calculation on its surface. The flux evaluation implies that not only the optical performance of the single heliostat, but also the energy associated to the reflected beam must be considered. Analogously to heliostat field models,

ray-tracing and integration (fully analytical) methods are available for the flux calculations and even if with Monte Carlo version it is possible to reduce the approximation of ray-tracing, the analytical methods ensure the evaluation of the peak flux levels with a small deviation (less than 2%) saving more computational time [55]. In the most diffuse methods, UNIZAR and HFLCAL models [72, 73], a convolution approach is applied and the solar flux is projected on the receiver surface from the image plane [74]. Alternative solutions, as the one presented by Wagner and Wendelin in [75], are available; however, HFLCAL is considered the best compromise between simplicity and accuracy [76].

In this work the development of a comprehensive model for generating and simulating the heliostat field is presented. The goal is to achieve a good compromise between accuracy and computational effort. The model is included in an optimization procedure for the design of the mirror's layout.

1.2 Heliostat field model

The developed heliostat model can be divided in two parts: a preliminary field generation and the optical efficiency calculation.

1.2.1 Field generation

A radial staggered layout heliostat field is assumed, since the high efficiency of this scheme has been widely proved [51]. The heliostats are placed in rings around the central tower. The mirrors in the outer ring are placed between two heliostats of the inner ring: this distribution reduces the shadowing and blocking effects, as documented by Li et al. [77]. The entire field is divided in rows having constant angular spacing between contiguous heliostats. As the distance from the tower increases, the azimuthal spacing gradually enlarges: once an extra mirror can be placed between two adjacent heliostats in the same row, the number of mirrors per row doubles up [63].

Every heliostat is represented, as reported in figure 1.1, by a circumference (DM) which indicates the section of field covered by the heliostat horizontal projection. The DM value includes an extra-security distance, namely d_{sep} added to the heliostat diagonal DH (Eq.1.1). The research proposed by Collado in [33] has shown that this clearance can be neglected.

$$DM = DH + d_{sep} \tag{1.1}$$

The radial distance between consecutive rows is evaluated according to eq. 1.2, where $\mathrm{dR_i}$ is a design parameter determining the row spacing, with a minimum

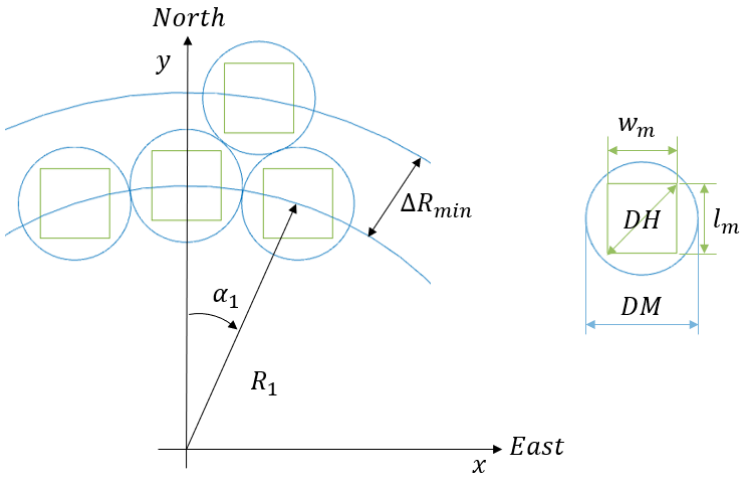

Figure 1.1: *Fundamental definition in radial staggered heliostat field.*

value of $cos30°$ (eq. 1.3) [51].

$$\Delta R_i = dR_i \cdot DM \tag{1.2}$$

$$\Delta R_{min} \simeq DM \cdot cos30° \tag{1.3}$$

The rows with the same number of mirrors define a group. The azimuthal distance along each row is determined as a function of R_{group}, the radius of the first ring of each group (R_1, R_2, ...), as shown in eq. 1.4,1.5 for the first three groups.

$$\Delta\alpha_i = 2\ asin[DM/2R_i] \simeq DM/R_i \tag{1.4}$$

$$\Delta\alpha_{i+1} = \Delta\alpha_1/2 \simeq DM/R_2 \Rightarrow R_2 = 2 \cdot R_1 \tag{1.5}$$

$$\tag{1.6}$$

In the present work, the first radius is defined as function of the tower height (eq. 1.7), as suggested by Kistler [62] in order to maximize the efficiency.

$$R_1 = 0.75 \cdot H_t \tag{1.7}$$

For every group, the number of heliostats per row is related to R_{group} and DM according to eq. 1.8

$$N_{hi} = 2\pi R_i/DM \tag{1.8}$$

$$\tag{1.9}$$

Collado and Guallar [64][33] observed that the radial distance can be kept constant along the group without penalizing the performance of the field. Consequently, the number of rows in each group can be calculated as Li et al.

proposed in [77] (eq. 1.10):

$$Nrows_i = (R_{i+1} - R_1)/\Delta R_i \cong round\,(R_i/\Delta R_i) \tag{1.10}$$

$$\tag{1.11}$$

ΔR_1 is set to give the densest solution (equal to ΔR_{min}), as this zone has the lowest blocking effect [64]. The other radial increments are matter of this study.

1.2.2 Performance model

The heliostat optical efficiency at time t in position (x,y) is calculated according to eq. 1.12 [77]. The equation considers the following losses: the mirror reflectivity ρ, the cosine effect f_{cos}, the atmospheric attenuation f_{att}, the spillage factor f_{spill} and the shadowing and blocking effect f_{sb}. The factors included in the eq. 1.12 are explained in detail in the next subsections, except for the reflectivity that is assumed to be constant (0.9).

$$\eta_{opt}(x,y,t) = \rho(t) \cdot f_{cos}(x,y,t) \cdot f_{att}(x,y,t) \cdot f_{sb}(x,y,t) \cdot f_{spill}(x,y,t) \tag{1.12}$$

Cosine factor

The cosine factor is the cosine of the angle θ measured between the incident sun-rays and the normal of the heliostat surface [54][70]. $\vec{S}$ and $\vec{T}$ are defined as the vectors pointing to the sun and to the receiver surface from the heliostat center, respectively. The normal to the surface of the heliostat (eq. 1.13) can be defined by the reflection law relationship, as reported in [78]. The cosine factor (eq. 1.14), according to the optics law, can be expressed using only the incident and reflected vectors.

$$\vec{n} = \frac{1}{2\cos\theta} \frac{\vec{S} + \vec{T}}{\left|\vec{S} + \vec{T}\right|} \tag{1.13}$$

$$f_{cos} = \cos\theta = \cos\left(acos\left(\frac{\vec{S} \cdot \vec{T}}{\parallel \vec{S} \parallel \parallel \vec{T} \parallel} \right)/2 \right) \tag{1.14}$$

Atmospheric attenuation

The atmospheric attenuation factor (eq. 1.15) considers scattering and absorption of the reflected rays, due to the presence of water vapor or aerosol in the atmosphere. The equation evaluates the beam losses as function of the distance

between the center of the heliostat and the aim point on the receiver (d_{hr}) [79].

$$f_{att} = \begin{cases} 0.99326 - 0.1046 \cdot d_{hr} + 0.017 \cdot d_{hr}^2 - 0.002845 \cdot d_{hr}^3 & d_{hr} \leq 1km \\ exp(-0.0001106 \cdot d_{hr}) & d_{hr} > 1km \end{cases} \tag{1.15}$$

Shading and blocking factor

The radiation reflected onto the receiver can be reduced by shading and blocking effects: these optical interferences, caused by the nearby heliostats, leads to a reduction of the effective reflective area. When shading phenomena occur, adjacent mirrors can create shaded areas on the considered surface. In case of blocking, a fraction of a reflected beam is intercepted on the way to the receiver. The shading and blocking factors can be considered as the portion of the mirror area that reflects successfully the radiation to the receiver. These factors must be considered together to avoid overestimating losses, and must be re-calculated throughout the day because the sun position and the mirror orientation are constantly changing [77]. Only a limited subset of mirrors can interfere with the reflection of each heliostat; identifying first the neighboring heliostats can improve the process of loss evaluation. In this work, the method presented by Besarati in [54] is adopted (Fig. 2): the first three heliostats closer to the heliostat in the direction of sun rays are selected for the shading investigation (orange circles), whilst the direction of the reflected beam is considered for the blocking effect (blue circles). The search space is function of the representative dimension DM and the distance between adjacent rows (ΔR_i).

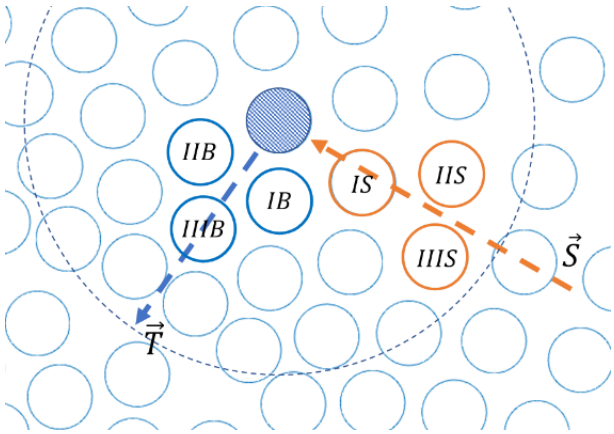

Figure 1.2: *Heliostat selection method for shading (orange) and blocking evaluation (blue).*

Then, for each selected mirror shadowing and blocking are simultaneously calculated according to a procedure based on Sassi's projection method [65], widely used by several authors [70, 29]. Some assumptions are considered

in the model: flat mirror surfaces, parallelism of the neighboring heliostats and absence of optical errors. Huang et al. [66] showed that this method, evaluating the heliostat image only from the projection of its center, tends to overestimate the f_{sb} value. In the present work, an improved model inspired to the method presented by Zhang et al. in [80] has been developed: the image of each heliostat is evaluated starting from the projection of its four vertices. The data presented in [51] have been used to validate the new shading and blocking model and the comparative analysis for two different d_{sep} is summarized in Table 1.1. The results show a good estimation of the shading and blocking factors, with a deviation closer to 1% considering the first zone and even less for the whole heliostat field.

Table 1.1: *Validation of the shading and blocking model.*

	Day=345, Solar time=9					
	dsep=0			dsep=3		
	Reference	New model	Difference (%)	Reference	New model	Difference (%)
Zone 1	0.788	0.799	1.40%	0.885	0.891	0.69%
Zone 2	0.775	0.781	0.73%	0.873	0.876	0.40%
Zone 3	0.645	0.648	0.42%	0.708	0.709	0.25%
Field	0.676	0.674	0.48%	0.747	0.749	0.26%

Spillage efficiency

The radiant power (P_h) associated to the beam reflected by each heliostat is defined considering all field optical losses, except the spillage factor (Eq. 1.16). P_h is considered to have a circular normal distribution, obtained by the convolution of three Gaussian error functions: the sun-shape error σ_{sun}, mirror slope error σ_{slp}, tracking error σ_{trk} (Eq. 1.17) [81]. The typical values of the standard deviations are 2.51 mrad, 0.94 mrad and 0.63 mrad, respectively [64].

$$P_h = DNI \cdot \rho \cdot f_{cos} \cdot f_{att} \cdot f_{sb} \tag{1.16}$$

$$\sigma_e = \sqrt{d_{hr}^2 \left(\sigma_{sun}^2 + 2\left(1 + f_{cos}\right)\sigma_{slp}^2 + \sigma_{trk}^2\right)} \tag{1.17}$$

In CRS application with molten salt as heat transfer fluid, a limitation in the working temperature is imposed to avoid corrosion problems in the receiver tube. With a typical outlet temperature of $565°C$, the flux on the receiver surface is limited to $1MW/m^2$ [82]. Since all heliostats pointing to the receiver equator generate an excessive peak flux, an aiming strategy must be adopted to vertically shift the target points and evenly distribute the energy spots. The multi-aiming strategy implemented by Sánchez-González and Santana [57] is adopted in this study. The vertical displacement zR of the aim point is such that the beam circumference is alternatively tangent to the upper or the lower receiver edge, for heliostats placed in consecutive rows (Eq. 1.18) [83]. The beam radius (BR_k) depends on the considered width of the Gaussian curve,

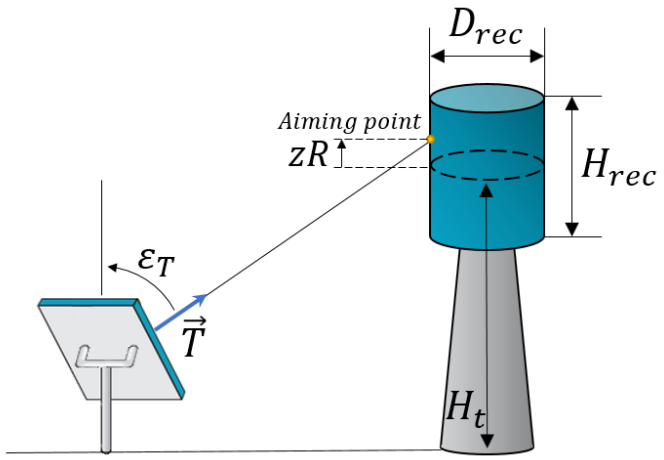

Figure 1.3: *Definition of the main parameters of the tower-receiver system.*

associated with the desired beam energy intensity to be collected (refers to Eq. 1.16-1.17): the parameter k, named aiming factor, is introduced to manage this width (Eq. 1.19). The value of k could be changed in order to adjust the energy collected: a value of 5 leads to an equatorial aiming, whilst only 1% of P_h is lost if k = 3 [84].

$$zR = \pm\left(\frac{Hrec}{2} - BR_k\right) \tag{1.18}$$

$$BR_k = k \cdot \sigma_e / \sin\varepsilon_T \tag{1.19}$$

The spillage efficiency is defined as the ratio of the real energy collected by the receiver and the maximum one, which is reflected by the heliostat field: integrating analytically P_h over the receiver domain, considering also the aiming strategy, the resulting formula presented in Eq. 1.20 is based on HFLCAL method [73]. The dimensions of the receiver and the definition of the elevation angle ε_T are reported in 1.3.

$$f_{spill} = \operatorname{erf}\left(\frac{D_{rec}}{\sigma_e 2\sqrt{2}}\right)\frac{1}{2}\left(\operatorname{erf}\left(\frac{\left(\frac{H_{rec}}{2} - zR\right)\sin\varepsilon_T}{\sqrt{2}\sigma_e}\right) - \operatorname{erf}\left(\frac{\left(\frac{-H_{rec}}{2} - zR\right)\sin\varepsilon_T}{\sqrt{2}\sigma_e}\right)\right) \tag{1.20}$$

1.2.3 Heliostat field model validation

The developed model was validated against the commercial software SAM (System Advisor Model) [85]. A user defined heliostat field is used in the comparison: the results of the simulation with the new code (orange dots) show a good agreement with those of the commercial software (blue dots). The field efficiency for two reference periods, three winter days on the left, and three summer days on the right are reported in figure 1.4. An average deviation of 0.11% is obtained; the largest difference is observed in early morning and in the late afternoon, anyway lower than 2%. The efficiency model (Eq. 1.12) , written in Matlab language, is validated against the data available in [86], even for the new approach of shadowing and blocking factor. In Table 1.3, the comparison of the optical terms is reported for two fields; the difference from the reference always below 1% confirm a good accuracy of the model. Table 1.2 resumed the main parameters of the two layouts considered for the validation.

About the computational times, a single optimization on 8-core processor at 2.50 GHz and 8 GB of RAM requires less than 24 sec.

Table 1.2: *Key parameters of the layouts used for the code validation.*

Parameter	unit	Hourly efficiency (vs. SAM)	Detailed optical losses (vs. [86])
Location		Riyadh	Sevilla
Solar field thermal power	(MW_{th})	30	155
Number of heliostats		400	2646
Heliostat dimensions	(m^2)	144.375	115.76
Occupied land	(acr)	88	212
Tower optical height	(m)	100	130
Receiver dimension	(m^2)	48.89	279.82

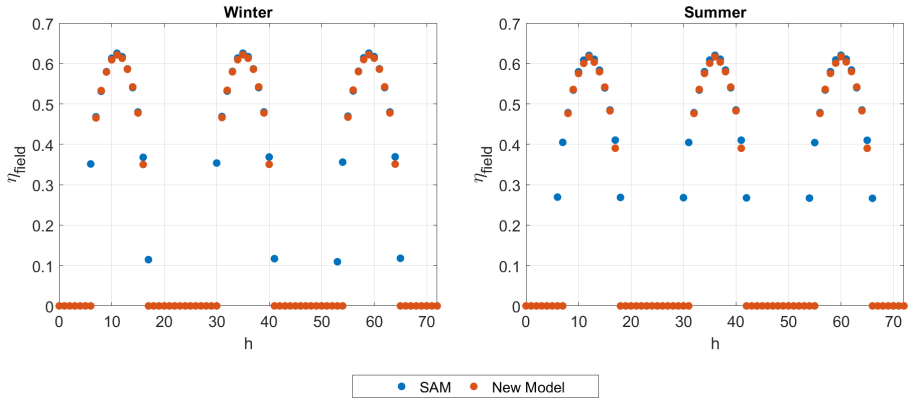

Figure 1.4: *Hourly field efficiency results: model vs. SAM.*

Table 1.3: *Validation of the efficiency model.*

	Case 1			Case 2		
	Reference	New model	Difference (%)	Reference	New model	Difference (%)
f_{cos}	0.8150	0.8164	-0.2%	0.8006	0.8018	-0.1%
f_{att}	0.9568	0.9502	0.7%	0.9515	0.9430	0.9%
f_{sb}	0.9128	0.9184	-0.6%	0.9563	0.9594	-0.3%
f_{spill}	0.9948	0.9979	-0.3%	0.9920	0.9920	-0.7%

1.3 Receiver performance model

The receiver configuration directly influences the local performance of individual heliostats within the collector field and is the dominant factor that determines the shape of the collector field. Two are receiver shapes commonly adopted in CRS: external cylindrical or cavity, as presented in Fig. 1.5.

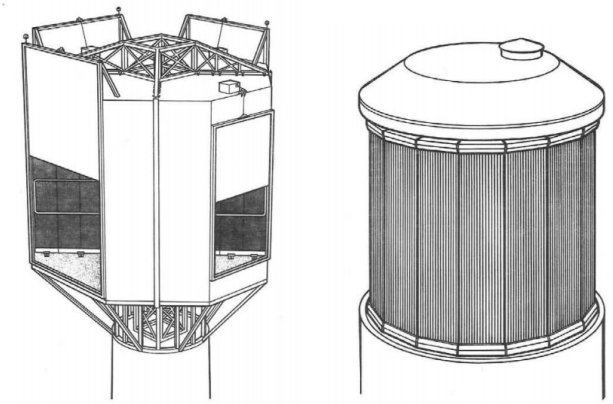

(a) *Cavity receiver (four-aperture)* **(b)** *External receiver*

Figure 1.5: *Examples of the two receiver configuration.*

A typical external receiver consists of multiple absorbing panels approximating a cylindrical surface. In the cavity receiver, the absorbing panels are inside the receiver structure and the reflected rays pass through an aperture. The exact internal configuration of the cavity is used for the calculation of the cost, thermal losses and flux profiles, the optical calculations of the field are done at the aperture [62]. The cavity geometry can greatly affect the flux distribution on the inner walls, but has almost no influence on the absorption efficiency [87]. The cavity configuration assumptions of the DELSOL software [62] are adopted for the analysis: the absorber surface is a vertical cylinder, centered horizontally on the aperture. The absorption efficiency η_{abs} (Eq. 1.28) is defined as the conversion ratio from the irradiance E_{rad} to the energy delivered to the transfer fluid E_{abs} (Eq.1.21-1.22), equivalent to the incident energy to the receiver surface E_{inc} (Eq. 1.23) less the thermal losses $L_{thermal}$ (Eq. 1.24)

(convective Q_{conv} and radiative Q_{rad} (Eq. 1.26-1.25)). Rewriting Eq. 1.21, it is possible to define the receiver efficiency η_{rec} (Eq. 1.27) and then η_{abs} can be written as the combination of the efficiency of the field and the receiver (Eq. 1.28). It is assumed that the receiver losses, presented as an efficiency, do not vary with time (equal to design point efficiency).

$$E_{abs} = \eta_{abs} \cdot E_{rad} \tag{1.21}$$
$$E_{abs} = \alpha_{rec} \cdot E_{inc} - L_{thermal} \tag{1.22}$$
$$E_{inc} = \eta_{field} \cdot E_{rad} \tag{1.23}$$
$$L_{thermal} = (Q_{rad} + Q_{conv}) \tag{1.24}$$
$$Q_{rad} = \varepsilon \sigma A_{rec}(T_{wall}^4 - T_{amb}^4) \tag{1.25}$$
$$Q_{conv} = h_{mix} A_{rec}(T_{wall} - T_{amb}) \tag{1.26}$$
$$\eta_{rec} = \alpha_{rec} - L_{thermal}/E_{inc} \tag{1.27}$$
$$\eta_{abs} = \eta_{field} \cdot \eta_{rec} \tag{1.28}$$

For the evaluation of the receiver losses a mean wall temperature T_{wall} of 813 K is considered assuming a uniform heat flux distribution and a linear wall temperature profile. When an external receiver is treated, a mixed convective coefficient h_{mix} of $16.61 W/m^2K$ is assumed; the solar absorption and the emissivity of the receiver are set to 0.95 and 0.9, respectively [33].

Cavity thermal losses

The enclosure structure represents an advantage for the receiver losses: the absorber surfaces are protected and the convection losses are limited; the coefficient h_{mix} of eq. 1.24 is adjusted based on the suggestion reported in [88] (Eq. 1.30); furthermore, as conservative assumption, if no informations are specified, the contribution of natural and forced convection is considered equal $h_{fc} = h_{nc}$ [89].

$$h_{mix} = h_{nc} + h_{fc} \tag{1.29}$$
$$h_{nc} = 0.81 \cdot (T_W - T_a)^{0.426} \tag{1.30}$$

The cavity effect allows to recuperate a portion of the emitted and reflected radiations. Considering the view factors of the surface in the receiver (1: the absorber surface, 2: the aperture area and 3: the other surface) F_{11} and F_{13} are not considered losses but with re-reflection the energy remain in the cavity.

$$F_{21} = 1 \rightarrow A_2 F_{21} = A_1 F_{12} \rightarrow F_{12} = \frac{A_{ape}}{A_{rec}} \tag{1.31}$$

The radiative losses are considered attributed to the aperture with temperature equal to the wall surface (Eq. 1.32). ε is assumed 0.8 as suggested in [90].

$$Q_{rad} = \varepsilon \sigma A_{ape}(T_W^4 - T_a^4) \tag{1.32}$$

From the definition of Q_{refl} in the cavity (Eq. 1.33), and from the energy balance of the incident radiation in an opaque medium (Eq. 1.34) is possible to define the effective absorption efficiency α_{eff} (Eq. 1.35). Yao et al. quantify the cavity effect, increasing the absorption efficiency to 0.97 [88].

$$Q_{refl} = Q_{in} \cdot Fr \cdot \rho \tag{1.33}$$

$$\alpha + \rho = 1 \tag{1.34}$$

$$\alpha_{eff} = 1 - Fr \cdot \rho \tag{1.35}$$

1.4 Solar flux model

The flux density is determined for the design condition suggested by SAM software (solar noon of the spring equinox with a DNI reference value of $950 W/m^2$ [75]) and the maximum allowable incident flux is considered before reflection, irradiation and convection losses. The receiver surface (both for the cavity and for the external configuration) is discretized with a regular mesh where each point is identified with the azimuthal angle θ and the vertical displacement from the optical height h (Fig. 1.6); more the mesh is thick (which means smaller $\Delta\theta$ and Δh), more the flux prediction is accurate but more time consuming. The contribute of all heliostats in each point is summed up, and then the respect of the allowable flux density (AFD) of $1.1 MW_t/m^2$ is verified.

As best practice suggestion, the analytical method of HFLCAL is adopted given its simplicity and accuracy. The energy associated to the radiation reflected by each heliostat is defined considering all field optical losses, except the spillage factor (Eq. 1.16). P_h is considered to have a circular normal distribution, obtained by the convolution of the Gaussian cone of the optical errors (Eq. 1.17) [81].

The definition of the solar flux through the analytic functions is correct only if considered on the image plane, defined as the normal plane to the central reflected ray (with azimuthal and zenithal direction equal to α_T and ε_T) [57]. The energy intensity of F_{image} in each point is a function of the distance from the aiming point (x_{AP}, y_{AP}) as observed in Eq. 1.39. From an energy balance, the energy contained per unit area is preserved if it is considered any point of the image plane (x, y) or the corresponding point on the receiver surface (x_c, h). Therefore, the flux distribution on the receiver surface F_{cyl} is reconstructed with a projection procedure (Eq. 1.40), as presented by Collado in [71] the Jacobian of each point projection is calculate for each node in the image plane.

The panel structure of the receiver is approximated with a simplified cylinder; each point is identified by its height h, measured from the receiver equator, and its circumferential position from the south θ, which correspond to an arc of length x_c (Fig. 1.6).
When cavity receiver is considered, the correlations Eq. 1.36 -1.40 are still valid; the vertical displacement zR at the absorber surface is not imposed by an aiming strategy but it is consequence of the central aiming at aperture surface, as highlighted in fig. 1.7.

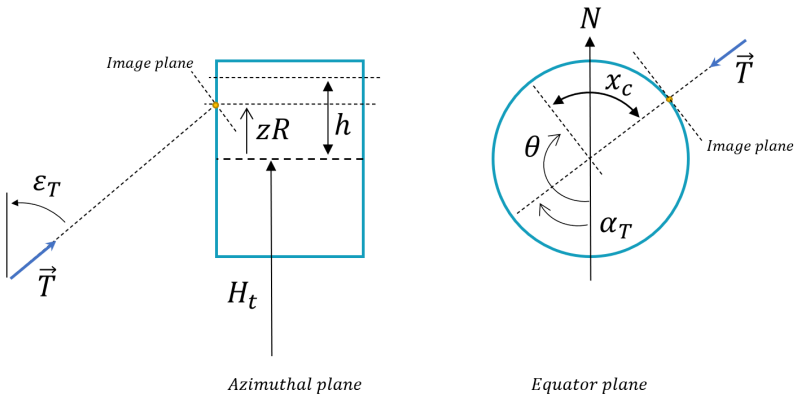

Figure 1.6: *Definition of the main parameters of the external receiver local system.*

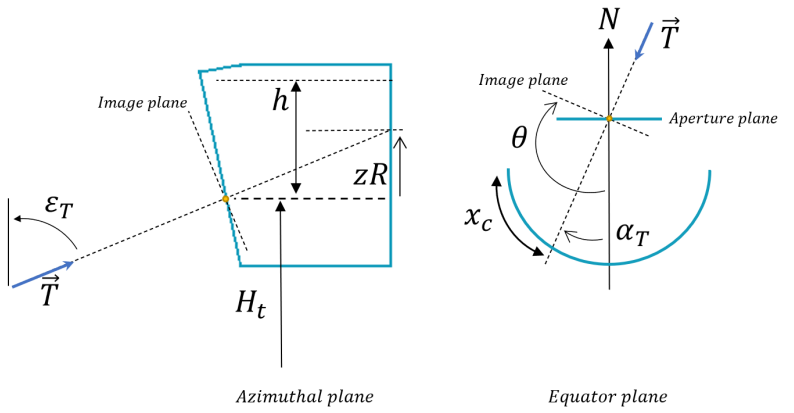

Figure 1.7: *Definition of the main parameters of the cavity receiver local system.*

$$y = (h - zR) sin\varepsilon_T \tag{1.36}$$

$$x = RR \cdot sin(\theta - \alpha_T) \tag{1.37}$$

$$Jac = |\sin \varepsilon_T \; cos(\theta - \alpha_T| \tag{1.38}$$

$$F_{image}(x, y) = \frac{P_h}{2\pi\sigma_e^2} \exp\left(-\frac{(x - x_{AP})^2 + (y - y_{AP})^2}{2 \cdot \sigma_e^2}\right) \tag{1.39}$$

$$F_{cyl}(x_c, h) = F_{image}(x, y) \cdot Jac \tag{1.40}$$

1.4.1 Solar flux model validation

The developed solar flux model is firstly validated for the cavity receiver with respect to the data of PS10 plant, available in [91]. In the figure 1.8 the resulting solar flux profile for two instant (solar noon of 21^{st} March and 4 pm of 21^{st} June) are compared with the literature and in table 1.4 the mainly performance parameters associated to the profile are reported. The collected energy at spring equinox noon is slightly underestimated, whilst the maximum peak value is overestimated for 21^{st} June at 4pm, but all the deviation are lower than $\pm 2\%$.

Table 1.4: *Validation of the solar flux calculation model.*

	21st March at solar noon			21st June at 4pm		
	Reference	New model	Diff (%)	Reference	New model	Diff (%)
$\dot{Q}_{rec}(MW)$	54.7	53.5	-1.90%	36.8	36.4	-0.01%
$Flux_{peak}(kW/m^2)$	650	650	0.00%	455	463	1.72%
η_{opt}	0.745	0.748	-0.40%	0.603	0.6016	-0.23%

For completeness also the validation for the external receiver model is reported. The solar flux profiles of an external multi-panel receiver, presented in [57], are used for the comparison. In table 1.5 the coordinates of the three reference heliostats considered are reported to help the reader to understand the profile. The results in Fig. 1.9 show a good agreement between the two methods, confirming the reliability of the developed model also for external receivers.

Table 1.5: *Coordinates of selected heliostats for the flux validation*

	x (m)	y(m)
a	0	324.49
b	147.84	48.04
c	630.15	204.74

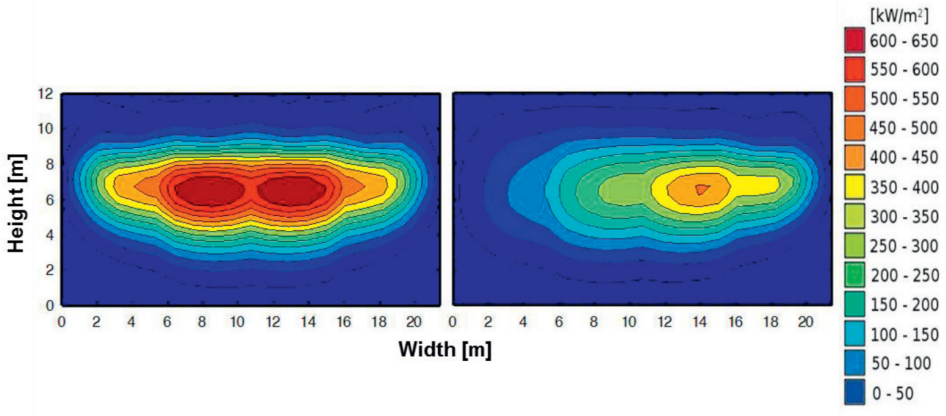

(a) *Reference data available in literature [91]*

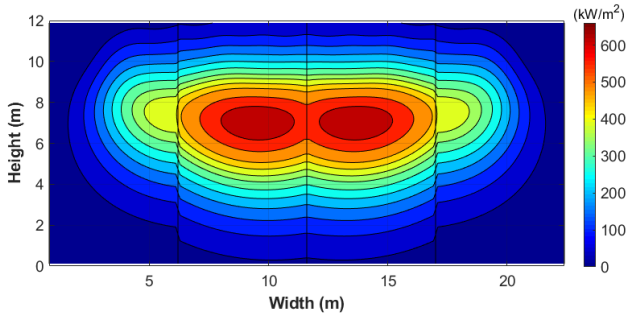

(b) *21st of March at solar noon*

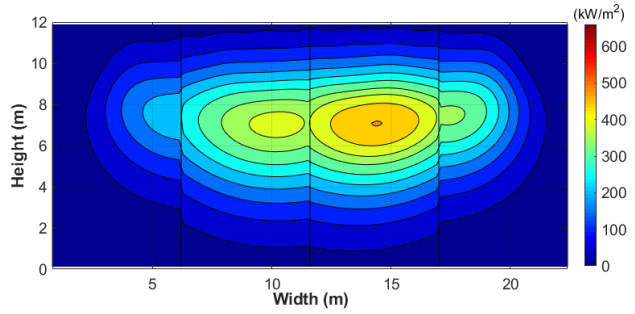

(c) *21st of June at 4 pm*

Figure 1.8: *PS10 flux map comparison between literature data and model output.*

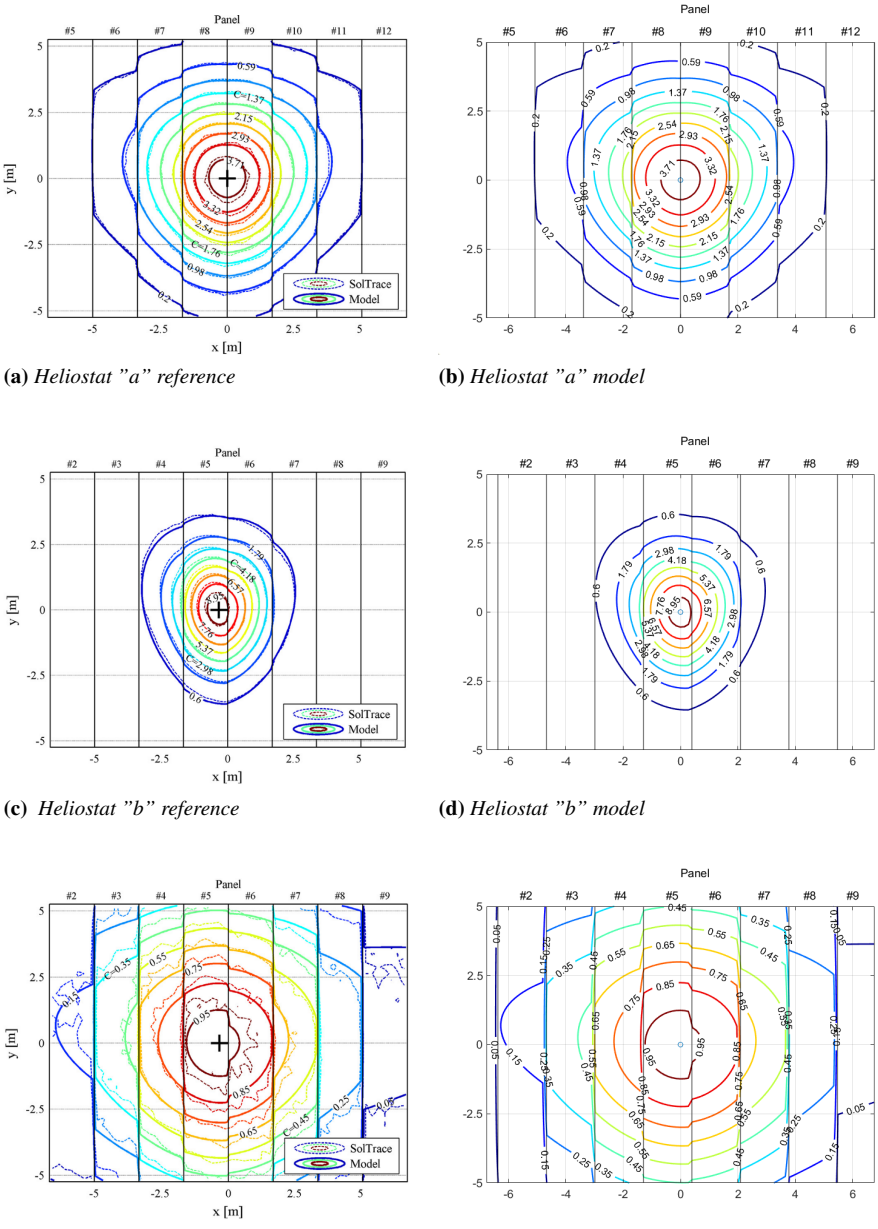

(a) *Heliostat "a" reference*

(b) *Heliostat "a" model*

(c) *Heliostat "b" reference*

(d) *Heliostat "b" model*

(e) *Heliostat "c" reference*

(f) *Heliostat "c" model*

Figure 1.9: *Solar flux profiles comparison between literature data and model output.*

1.5 CRS annual performance

Once presented the detailed model for the simulation of the central receiver system, the main performance parameters are considered to correctly compares

different CRS solutions. The performance can be assessed on a technical or economic basis

- Annual insolation weighted efficiency, defined as reported in eq. 1.41:

$$\eta_{ann,w} = \frac{\sum_{i=1}^{365} \int_{sunrise}^{sunset} DNI(t)\eta_{field}(t)dt}{\sum_{i=1}^{365} \int_{sunrise}^{sunset} DNI(t)} \tag{1.41}$$

- Levelized cost of electricity (eq.1.42):

$$LCOE(¢USD/kWh_e) = \frac{\frac{i(1+i)^{N_y}}{(1+i)^{N_y}-1} C_{plant}}{E_{El}} + OM \tag{1.42}$$

Eq. 1.42 includes the operation and maintenance costs OM (broken down as a fixed cost by capacity and a variable cost by generation, respectively 66 USD/kW-yr and 0.35 ¢USD/kWhe [85]). The indirect costs (contingency, EPC and sales) that contribute to the total installation cost C_{plant}(eq. 1.43 and the financial parameters for the calculation of the LCOE are reported in Tab. 1.6: the lifetime and the interest rate are taken from [92] to align the analysis with the latest announcement of DEWA IV power plant. The plant primary cost C_{plant} (eq. 1.44) is evaluated as sum of the costs of each component: heliostat field (eq. 1.45), tower (eq. 1.46), receiver (eq. 1.47) and power block (eq. 1.49). The cost of the heliostat field (eq. 1.45) is proportional to the unit cost C_{m^2}, including the site improvement cost ($156 \quad USD/m^2$). The cost of the power block is based on the rated power output. The unit cost values and the correlations reported in eq. 1.45 -1.49 are from [85].

Table 1.6: *Financial parameters.*

Parameter	Value
Lifetime (Ny)	35
Interest rate (i)	5
Contingency	7%
Sales	4%
EPC	13%

$$C_{plant} = Plant_{cost} \cdot (1 + Contingency) \cdot (1 + Sales + EPC)\ (USD) \quad (1.43)$$

$$Plant_{cost} = C_{helio} + C_t + C_{rec} + C_{PB}\ (USD) \quad (1.44)$$

$$C_{helio} = C_{m^2} \cdot A_h \cdot N_h\ (USD) \quad (1.45)$$

$$C_t = 3000000exp\,(0.0113(H_t - H_{rec}/2 + lm/2))\ \ (USD) \quad (1.46)$$

$$C_{rec} = 1.03 \cdot 10^8\,((D_{rec}H_{rec}\pi)/1571)^{0.7}\ \ (USD) \quad (1.47)$$

$$C_{cav} = 2.3 \cdot 10^7 \left(\frac{A_{rec}}{758}\right)^{0.8}\ \ (USD) \quad (1.48)$$

$$C_{PB} = 1330P_{el,nom}(USD) \quad (1.49)$$

CHAPTER 2

Design period analysis

2.1 Introduction

The effect of the plant design parameters on the system performance is still unclear, as underlined by Rui Chen et al. [39], such as the design meteorological condition or the solar multiple. Recently different authors addressed the field optimization from different points of view. Gadalla and Sagafifar establish the best heliostat arrangement based on the shadows and block efficiency [70]. Schöttl et al. prefer a whole field approach to the performance evaluation of individual heliostat, the layout boundaries are determined with consideration on annual efficiency and land occupancy [93]. It was also noted that the influence of the design parameters changes with different optimization function. Li et al. demonstrated that the most efficient solution is not the cheapest one [77]. Leonardi et al. analyzed the impact of the land cost on the layout of a 55 MW plant, underlying that is possible to reduce the area by almost 50% without damaging the annual efficiency [94]. Kiwan and Hamad considered the tilt of the land to minimize the occupancy, however the resulting annual efficiency is damaged [95]. An additional issue is introduced when the size of the plant increases. In the maximization of the power collected on the receiver, Cruz et al. underlines that managing a commercial scale heliostat field means an high computationally optimization cost [96]. Collado and Guallar in [27] extend their field analysis to a commercial scale CRS plant (more than 100 MWe) and

it is founded out that the impact of strong layout changes is minimal for fixed receiver and tower dimensions.

When the CRS system is called to operate in more severe condition (such as in "island mode"), the seasonal behavior of the efficiency could be decisive for the production reliability. Considering different design period during the optimization could help to select the most suitable solution for each application. The investigation carried out by Eddhibi [68] considers the hourly trend of different optical losses and their variation throughout the year (March, June, September and December); with a detailed analysis, it is obtained a heliostat field with a minimized effect of blocking and shading. Saghafifar and Gadalla evaluate the cosine factor with increasing time scales (from instantaneous, to yearly time average); the results underline that an instantaneous approach is more advantageous for the optimization of small scale field, a larger time average period is more reliable increasing the field size[97]. Furthermore, the paper presented by Chen et al. [39] underlines the influence of the design period on the efficiency: the optimal design DNI (that is strictly related to the month considered) is function of the distribution of solar irradiance throughout the year and generally lower than the classical recommended values.

Usually, heliostat optimization algorithms aim to maximize the overall efficiency in a selected day (typically 21^{st} March or 21^{st} June) or the annual energy production. In the present work, on the contrary, the layout optimization is carried out to maximize the load-following capability of a solar tower plant. Even more frequently CSP plants operate in weekly interconnected grids with high penetration of renewables. Typically, in this scenario wind and PV have grid priority and the role of CSP plants is covering the residual demand before the intervention of fossil plants. So, they must meet peaks occurring in different months, depending on the profile of the power demand, on the PV market share and on the wind speed frequency distribution. CSP plants (and mostly solar towers) can guarantee a short-term (hourly or daily) flexibility thanks to the built-in thermal storage and a dispatchable generation very valuable to the market.

The present work shows that an optimization strategy of the heliostat field can also provide a long-term flexibility when operating with a high seasonal variability of the power demand. By a multi-variable optimization, the best configuration is determined under technical and economic considerations for a given reflective area. Subsequently, an economic sensitivity analysis is also presented, to show how budget costs impact on the optimal plant configuration. Finally, different heliostat sizes are investigated to further improve the efficiency and reduce the cost of the plant. The analysis is carried out for two different sizes of the solar field.

2.2 Design optimization

An optimization procedure based on the performance model presented in section 2 has been developed to design the solar field. For an established thermal power on the receiver, namely for a given number of heliostats, the heliostat field layout is identified by finding the best combination of the independent design variables values maximizing the goal function. As well known the heliostat field performance depends also on the tower and receiver sub-systems, so the tower height is introduced as optimization variable. Conversely, the dimensions of the receiver are assumed from the software SAM, for a reference field with the same reflected area [85]. Furthermore, the receiver does not show any interaction with the tower and may be optimized at a later stage, as shown by Luo et al. [40]. The optimal spacing of the heliostats is strongly influenced by the height of the tower as it acts directly on the operating orientation of the mirrors. For this reason, the optimization procedure is divided into two consecutive steps, according to the scheme shown in Fig. 2.1. First, for an assumed tower height H_t, the spacing coefficients of the radial staggered configuration (dR_2 and dR_3) are varied until the best compromise between shading and blocking effect and the other optical losses is reached, thus maximizing the optical efficiency η_{opt} for the considered design period [98]. The best radial coefficients $dR_{i,optI}$are hence used to generate the optimal layout ($layout_{optI}$) as follows:

- A field with an excess of heliostats is created with the radial staggered arrangement, as above described.
- The performance of each heliostat placed in the field is evaluated.
- The heliostats are sorted from the most to the least efficient.
- The final mirror layout is selected by choosing the most efficient heliostats, up to reach the predefined total number.

In the second step, the above procedure is repeated for different tower heights in the considered range and the resulting layouts are simulated on annual basis to get the field performance. Then the optimal tower height $H_{t\ optII}$ is selected in between all the analyzed cases as the one providing the best value of the goal function.

Since the analysis is done with fixed number of heliostats, maximizing the energy absorbed in the receiver corresponds to maximizing the heliostat field efficiency. However, the most efficient solution is not always the solution with the lowest cost [77]. As suggested in [33], once identified the best arrangement for each tower height, two optimization criteria can be identified, the technical one and the economic one. The two objective functions [70] are respectively

the annual weighted efficiency (Eq. 1.41) and the levelized cost of electricity (Eq. 1.42) already presented in the paragraph 1.5.

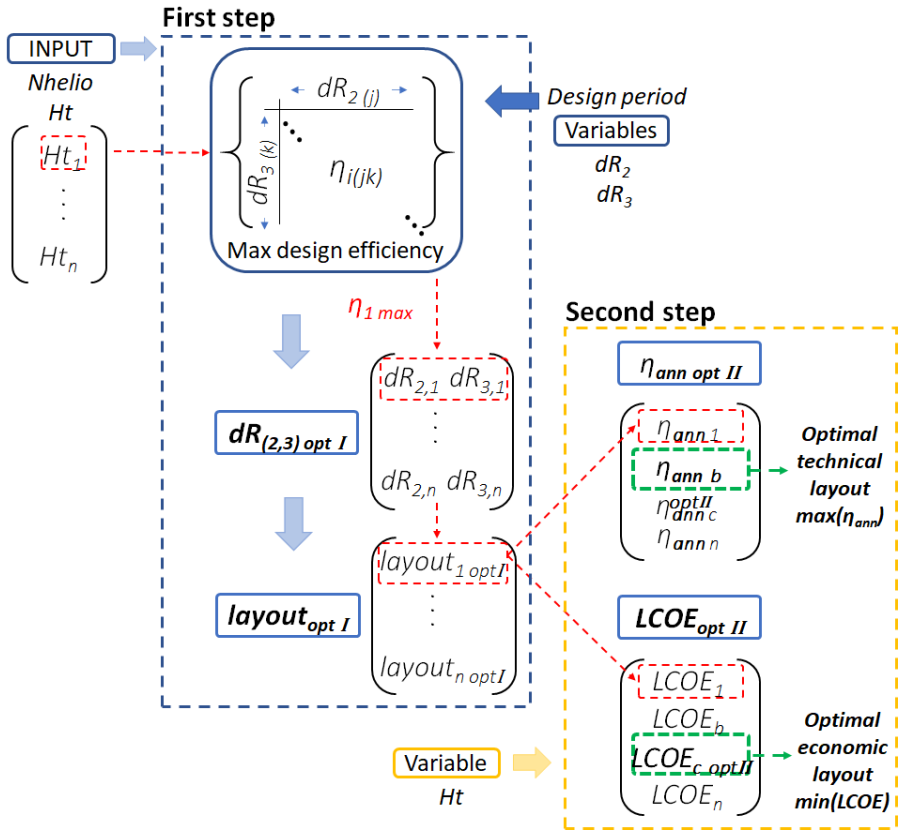

Figure 2.1: *Scheme of the two-step optimization algorithm.*

2.2.1 Methods and tool

With the aim of studying in detail the variables affecting the performance behavior, the optimization algorithm has been applied for two heliostat fields with quite different sizes: a small one (400 heliostats) and a large one (6400 heliostats) corresponding approximatively to 30 and 500 MW_{th} delivered in design conditions, respectively. Despite for smaller size a north field is generally preferred, the two possible layout shape (polar and surround) could present quite various influence for different parameters. To guarantee a more consistent comparison between the two size, the surround field is adopted for both the plant. It is however expected a more complete analysis for the smaller field in the next chapter, according to different receiver configuration. The main parameters imposed to the field design are reported in Tab. 2.1. The receiver

dimensions (that are not directly included in the following analysis) are determined by the software SAM for a plant with the same power [85].

Finally, it is necessary to evaluate the conversion from thermal energy to electricity for the calculation of the LCOE, so as to compare the solution with the current market situation: a reference steam turbine is considered for each field compatible with the receiver thermal power and with a solar multiple equal to 2, assumed with consideration on current operating plants. In this phase of the study, no penalty for off-design condition is considered.

Table 2.1: *Definition of the main parameters.*

Parameter	unit		
Field layout configuration		Surround	
Receiver configuration		External cylindrical	
Off-design operations		Not considered	
Heliostat dimensions	(m)	12.2x12.2	
Heliostat mirror area	(m^2)	144.38	
		Small field	Large field
Number of heliostat	-	400	6400
Total reflective area	(m^2)	57600	921600
D_{rec}	(m)	4.53	14
H_{rec}	(m)	4.67	15.4
Receiver design power	(MW_{th})	30	500
Steam turbine nominal capacity	(MW_e)	5	100
Steam turbine nominal efficiency [99]	-	0.333	0.425

Aswan (Egypt) is assumed as site location, where an annual DNI of 3200 kWh/m^2 is achieved [100]. The level of solar irradiance is referred to sampled measurements including clouds, pollution and dust effects, with reference to Meteonorm database [101].

The optical efficiency of the layout is a non-linear function, without an explicit structure and with several local minimums [30]. Due to the unknown trend of the objective functions and to the extension of the search space, a direct search optimization method is mandatory. A brute force method is preferred to highlight the influence of each parameters [80]: all the possible solutions are considered, and the best configuration is selected among all the parametric results. Table 2.2 shows the search space for each optimization variable, i.e. radial spacing dR_2, dR_3 and dR_4 (where $\Delta R_i = dR_i \cdot DM$ according to eq. 1.2) and tower height. ΔR_1 is fixed, as discussed before, and it is found, with a preliminary analysis, that the densest solution of the second group maximize the efficiency for the large field, then dR_2 is kept constant, equal to the minimal allowable radial spacing. Moreover, dR_4 is not investigated for the smallest field since all the heliostat are placed within the third group.

Table 2.2: *Definition of the search space.*

Variable	Field	Range	Step
dR_2	Small	0.866-1.4	0.09
dR_3	Both	1.2-2.5	0.16
dR_4	Large	3-4	0.16
Ht	Small	30-150	10
	Large	150-270	10

Furthermore, to show how the optimal heliostats layout depends on the considered design period, three optimization cases are presented in which the efficiency is maximized for the period when the peak power demand is expected: spring, summer, or winter. More precisely, the three design conditions refer to the solar noon of the 21^{st} of March, June, and December, respectively.

2.3 Design period results

In accordance with the scheme of Fig. 2.1, for each tower height the first step of the optimization process determines the values of the radial spacing parameters (dR_2, dR_3 and dR_4) that maximize the heliostat field efficiency. Fig. 2.2 shows how the efficiency of the small field (400 mirrors) is influenced by the radial expansion for the three design conditions. Similarly, Fig. 2.3 refers to the large-size heliostat field (6400 mirrors). The red points indicate the optimum dR_i value for various tower heights. The discontinuities of the optimal values are related to the discrete search span of the spacing variables, as shown in Table 2. Looking at the graphs reported in Fig. 2.2 (small-size heliostat field), some general trends can be observed. The higher is the tower, the more expanded is the optimum heliostat field, as documented by the increasing values of dR2 and dR3. For high towers (Ht $>$ 90 m), the expansion in the second group (dR2) leads to an efficiency improvement up to 2% (curves have a positive slope), whilst the efficiency curves have a negative slope or are flat for small towers. For Ht higher than 90 m (see Fig. 2.2-right), the curves efficiency vs. dR3 are flat, because the third group is empty, and the mirrors are placed all in the second group with a larger spacing. Moreover, the trend of the curves confirms that several configurations lead to very similar efficiency values, thereby defining an optimization criterion is difficult. Looking at different design periods, the maximum efficiency ranges from 72.4% (in December, Fig. 2.2c) to 74.2% (in June, Fig. 2.2b). In the layout designed for December conditions, the optimal radial spacing dR_2 is 1.4. Conversely, the optimal dR_2 is 1.22 when June is considered as design period. For both cases, all mirrors are placed within two groups. With regard to the optimal tower height, the field efficiency exhibits a maximum almost constant with towers ranging between

80 m and 120 m, whatever the design period considered. A different trend is observed considering the large heliostat field (Fig. 2.3). The relative distance between the heliostat rows has a strong impact, especially for the third group and for tower height lower than 200 m: values of dR_3 different from the optimal one lead to an efficiency reduction up to 6 percentage points. Increasing the tower height, the curves become flat, thus indicating a lower influence of dR_3. The nearly flat behavior of dR_4 suggests that only few heliostat are placed in the fourth group and a more expanded solution could help the shading and blocking factor; up to Ht = 200 m the . The layouts for March (Fig. 2.3a) and December (Fig. 2.3c) cases are quite similar, except for a variation in the optimum efficiency (64.8% vs. 62.4%). The layout designed for June conditions exhibits a maximum efficiency value of 65.9% with a tower 270 m high and a radial spacing $dR_3 = 2.1$.

The results of the first step optimization process are summarized in 2.2 and 2.3, where radial spacing and optical efficiency are plotted vs. tower height, for the small and the large field respectively. Looking at the small-size field (Fig. 2.2), the layouts maximizing the efficiency require only the second group to place the heliostats. The optimum radial spacing is slightly higher for June case than for the March and December ones, while the optimum tower height is similar (100-110 m). The small heliostat field shows a maximum efficiency of almost 70% for Ht = 110 m; taller towers have a better cosine factor, but the reduction of the spillage efficiency has a stronger impact on the overall performance. The best efficiency value is similar for March and June (73.78% and 74.18%) but rather lower for December case (72.43%). The optimization results of the large-size field are significantly different (Fig. 2.3). The higher is the tower, the higher is the field efficiency: the function η_{field} vs. Ht exhibits an asymptotic trend. Starting from 210 m, every 10 m added the efficiency gain step is lower than 0.01 points. The best efficiency is reached on the upper boundary of the investigated range of tower height (270 m): 64.82%, 65.86% and 62.42% for March, June and December cases, respectively. Concerning the optimal radial spacing, the best solution (June) is more compact than the one of March: the limitation of the atmospheric attenuation losses compensate the higher cosine effect.

2.3.1 Annual simulation

The optimal layouts for each tower height and for each design period have been simulated on annual basis and the target functions, $\eta_{ann,w}$ and LCOE, have been calculated as mentioned in the paragraph 1.5 with the assumption reported in Tab. 2.1. Fig. 2.6 and Fig. 2.7 compare design efficiency, annual average efficiency and LCOE vs. tower height for the design periods considered (in 2.6a, 2.6b, 2.7a and 2.7b additional optimization results are shown for further

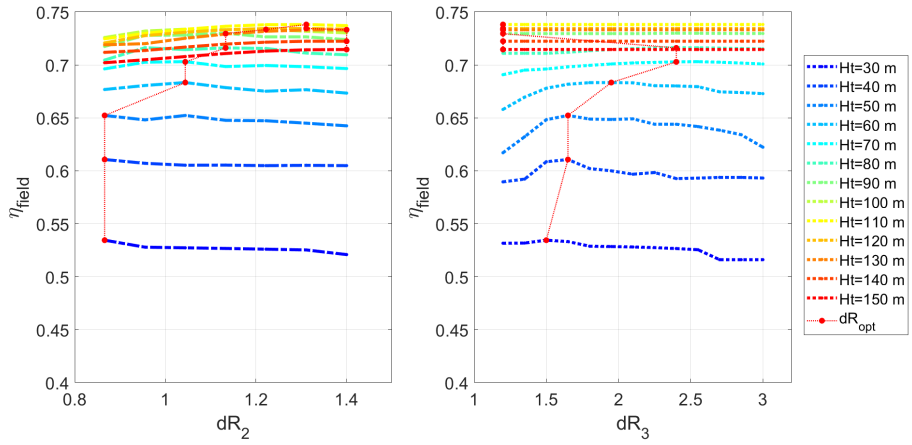

(a) *March*

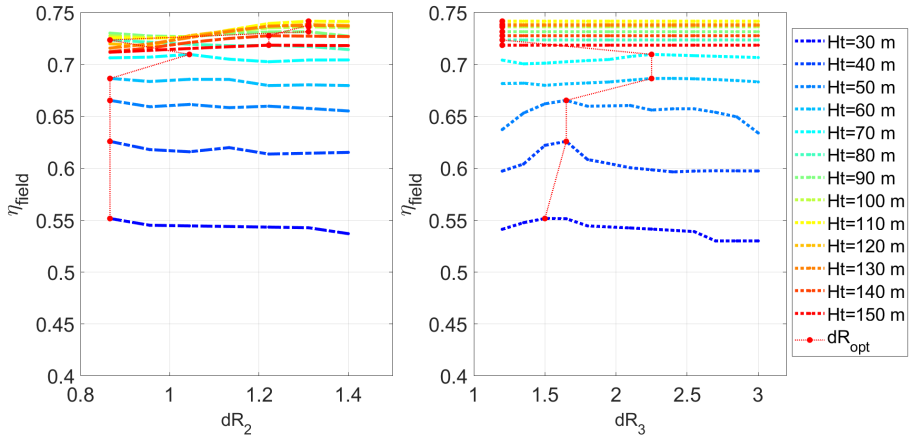

(b) *June*

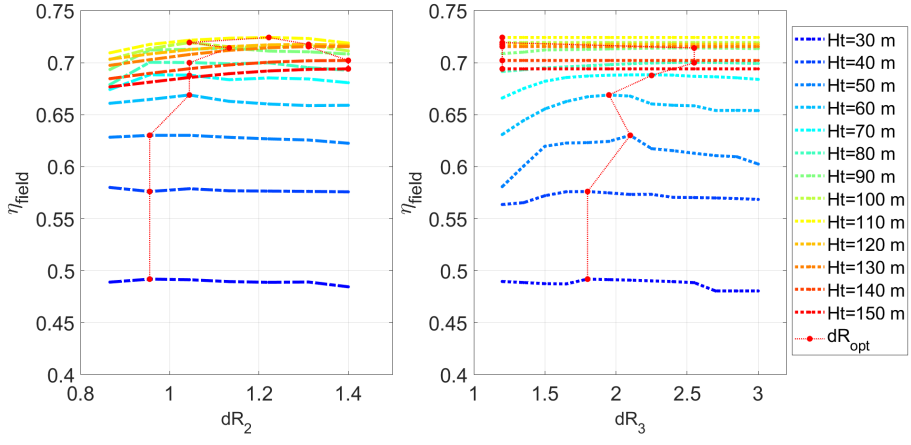

(c) *December*

Figure 2.2: *Optical efficiency vs. radial spacing varying tower height (small size field): impact of dR_2 (left) and dR_3 (right)*

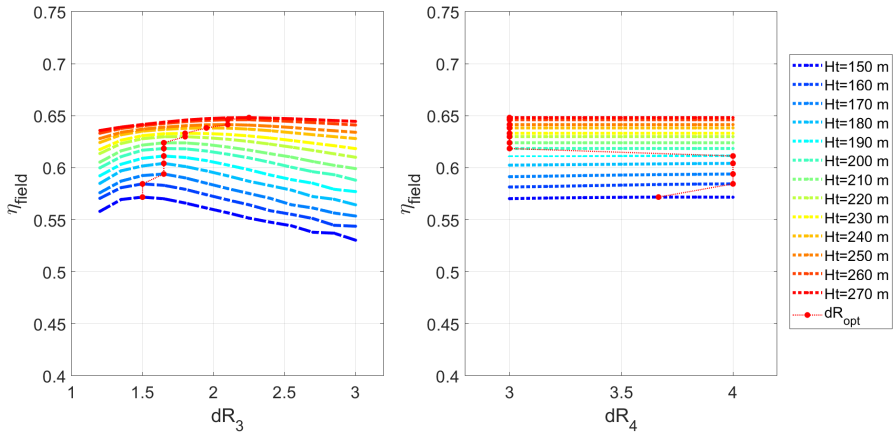

(a) *March*

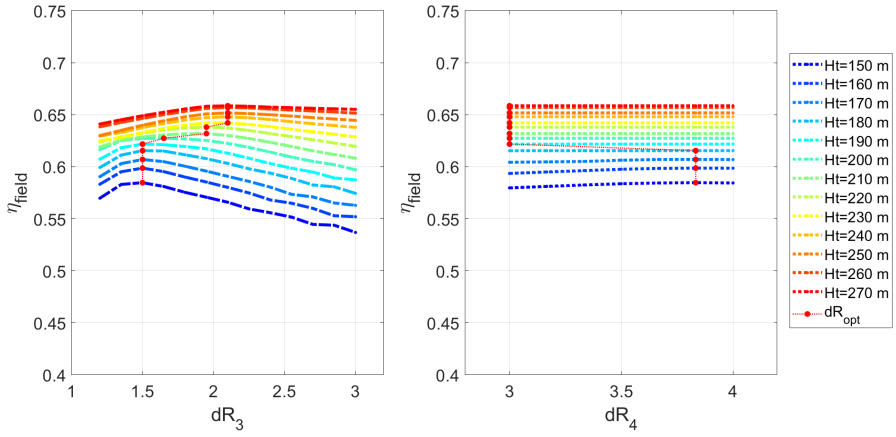

(b) *June*

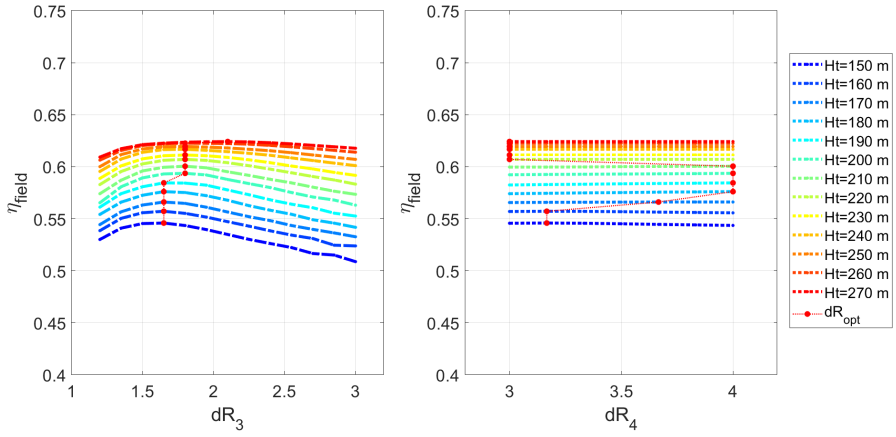

(c) *December*

Figure 2.3: *Optical efficiency vs. radial spacing varying tower height (large size field): impact of dR_3 (left) and dR_4 (right)*

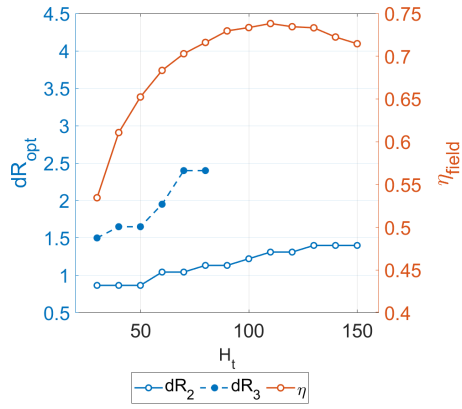

(a) *March*

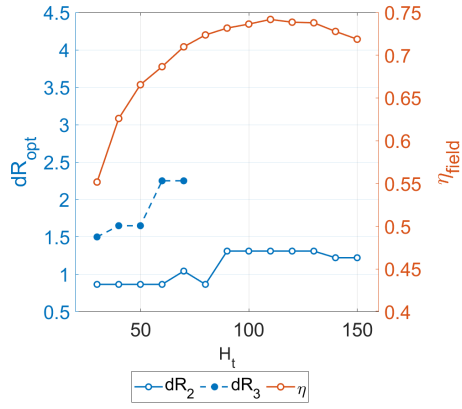

(b) *June*

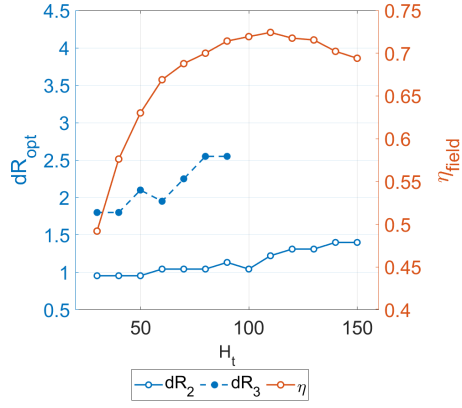

(c) *December*

Figure 2.4: *Radial spacing and optical efficiency vs. tower height*

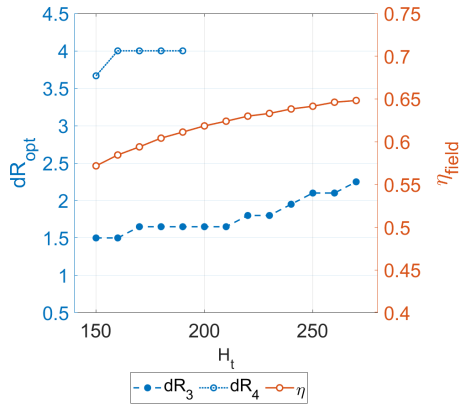

(a) *March*

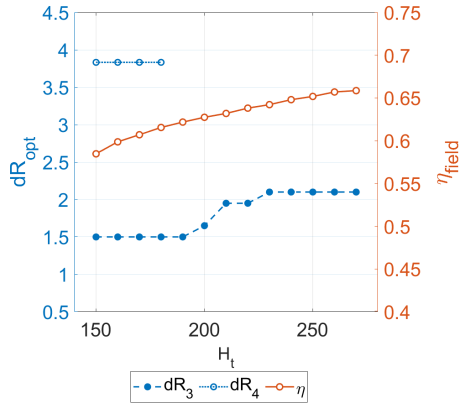

(b) *June*

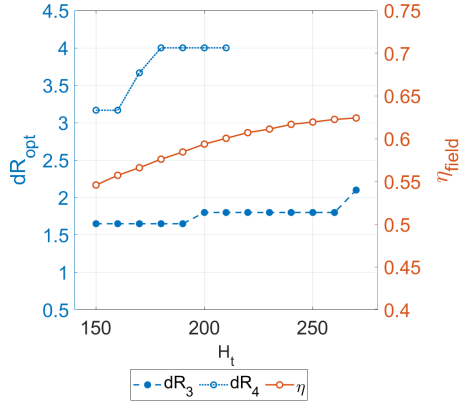

(c) *December*

Figure 2.5: *Radial spacing (dR_3 & dR_4)and optical efficiency vs. tower height (large field)*

design periods). Curves reported in Fig. 2.6a and 2.7a show a general trend: the higher is the Solar Zenith of the design condition, the higher is the optical efficiency. The average annual efficiency curves exhibit a trend similar to the one of the design efficiency, with a maximum for Ht 100-110 m in the small field case and an asymptotic behavior for the large one. But on annual basis the efficiency levels are very close to each other, with a slight prevalence for March case when Zenith angle ranges between 25° and 10°. Compared to March, June and December cases on annual basis show a deviation in the maximum efficiency value of -0.53% and -1.50% respectively for the small size field, whilst the deviations are +0.54% and -1.86% when evaluated at the design period. The same analysis is valid for the large size cases, where a maximum annual efficiency of 56.28% is achieved by the mirror field designed for March conditions. The influence of the Zenith design angle is further reduced to -0.34% and -1.12%, for June and December respectively.

Moving to the economic target function, the optimum is completely different. For the small field (Fig. 2.6-c), the cost of the tower has a strong impact: a prominent minimum can be observed for a tower height 60 m, corresponding to a LCOE of 9.52 ¢USD/kWh. On the contrary, the curve LCOE vs. Ht is almost flat in the large size case (Fig. 2.7-c): a plateau level around 5.97 ¢USD/kWh takes place in the range Ht 190-240 m. This behavior should be justified by a lower impact of the tower cost on the total investment (up to 10%) and the LCOE trend reflects the annual efficiency curves with a very slight deviation when different months are considered.

The summary of the optimization results is reported in Tab. 2.3 and Tab.2.4. The two target functions ($\eta_{ann,w}$ and LCOE) lead to different optimal solutions. A lower tower height (combined to a slightly more expanded layout) is preferred when the cost minimization is pursued: the annual efficiency is sacrificed by 8-4 percentage points, for a LCOE reduction of about 9% and 3%, for the small and the large case respectively. Referring to March as design period, the small size field exhibits a minimum LCOE (9.52¢USD /kWh) for a tower 60 m high, corresponding to an average efficiency of 61.21%, whilst the technical optimum is 66.36% for a tower height of 110 m. The solar field with 6400 mirrors achieves a maximum efficiency of 58.33% with a tower 270 m high and a LCOE 6.16 ¢USD/kWh, while the minimum LCOE (5.97 ¢USD/kWh) is obtained with Ht = 210 m (with a $\eta_{ann,w}$ = 56.21%).

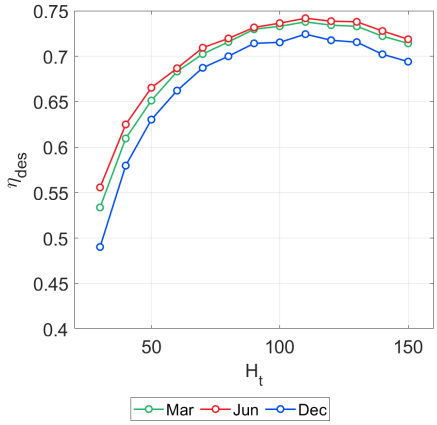

(a) *Design efficiency*

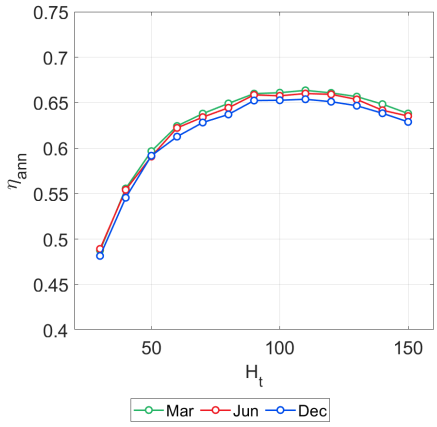

(b) *Annual average efficiency*

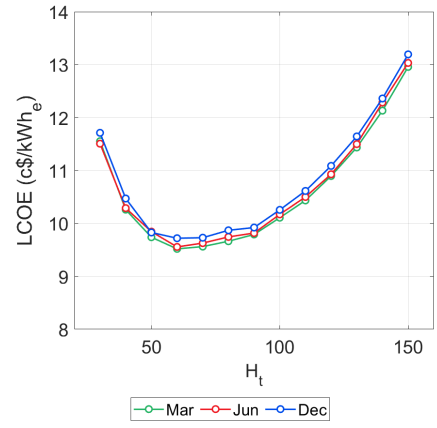

(c) *LCOE*

Figure 2.6: *Performance parameters vs. tower height (Small size heliostat field).*

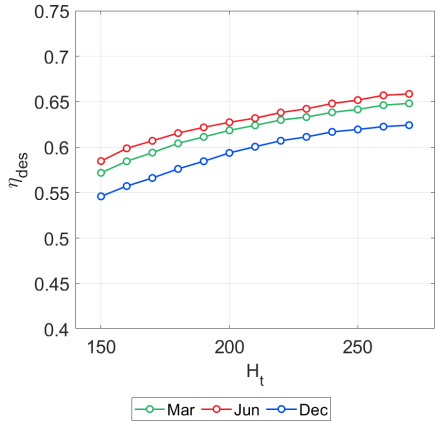

(a) *Design efficiency*

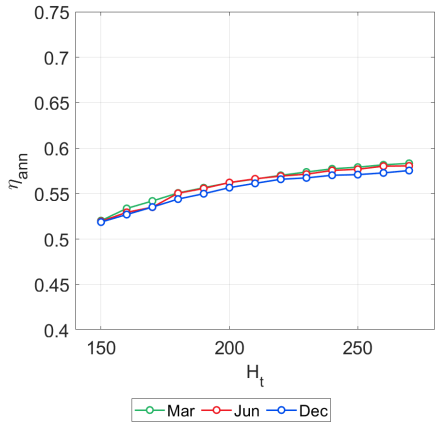

(b) *Annual average efficiency*

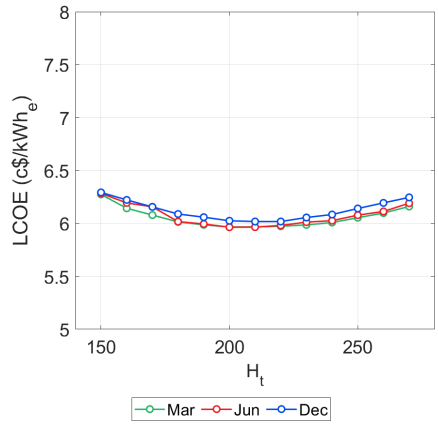

(c) *LCOE*

Figure 2.7: *Performance parameters vs. tower height (Large size heliostat field).*

Table 2.3: *Summary of optimization results (Small field).*

Design period	Ht, opt (m)	η_{des} (-)	$\eta_{ann,w}$ (-)	$Eabs$ (GWh)	$Ctot$ (Mio $)	$LCOE$ (c$/kWh)
Technical optimization						
March	110	0.7378	0.6636	94.15	44.23	10.43
June	110	0.7418	0.6601	93.53	44.23	10.50
December	110	0.7243	0.6538	92.50	44.25	10.61
Economic optimization						
March	60	0.6832	0.6121	92.60	38.81	9.52
June	60	0.6868	0.6223	92.23	38.84	9.56
December	60	0.6622	0.6127	90.61	38.87	9.72

Table 2.4: *Summary of optimization results (Large field).*

Design period	Ht, opt (m)	η_{des} (-)	$\eta_{ann,w}$ (-)	$Eabs$ (GWh)	$Ctot$ (Mio $)	$LCOE$ (c$/kWh)
Technical optimization						
March	270	0.6482	0.5833	1481.18	454.10	6.16
June	270	0.6586	0.5805	1473.38	453.81	6.19
December	270	0.6242	0.5754	1459.57	454.30	6.25
Economic optimization						
March	200	0.6240	0.5621	1430.69	418.52	5.97
June	200	0.6319	0.5622	1431.03	418.81	5.96
December	200	0.6005	0.5566	1415.66	419.19	6.02

Geometry and heliostat position of the layouts resulting from the two optimization processes are summarized in Table 2.5 and 2.6. Additional information is shown in graphical way in Fig. 2.8 and Fig. 2.9, where the efficiency of each mirror is indicated by color and the hourly trend of the field efficiency is also reported for three different days. Starting from the small size field, the impact of the different design periods on the placement of the mirrors is remarkable. Looking at June as design period (Fig. 2.8c and Fig. 2.8d, the optimum layout exhibits an almost uniform distribution of heliostats around the tower, and the occupancy radius is almost the same along the four directions. Conversely, the design at December conditions (Fig. 2.8a and Fig. 2.8b) selects the heliostats in the northern region as favorites, since the cosine effect is better in that area: the layout is close to a polar configuration with less than 30% of the heliostats in the southern region. The mirror distribution in the technical optimum layouts (Fig. 2.8a, Fig. 2.8c and Fig. 2.8a) basically consists of two groups: the third group is occupied only by very few heliostats. The first group is extended up to 165 m from the tower with radial spacing $\Delta R_1 = DM \cdot cos30°$, in the second one the radial spacing is equal to $DM \cdot 1.4$

except for June case, which is slightly more compact with $\Delta R_2 = DM \cdot 1.222$. On the contrary, in the optimum LCOE layouts (Fig. 2.8b, Fig. 2.8d and Fig. 2.8b) the first heliostats are closer to the tower and the first group is limited to only three rows in accordance with a smaller tower. The second group with $\Delta R_2 = DM \cdot 1.044$ is extended up to 180 m from the tower. Finally, the third group shows a different ΔR_3 for each design period: more compact for March and December cases ($DM \cdot 1.92$ and $DM \cdot 2.14$ respectively) and more expanded for June configuration ($DM \cdot 2.36$).
In the large size case, the layouts corresponding to March and June as design periods show the same radial spacing for the economic optimization: $\Delta R_3 = DM \cdot 1.65$, and the fourth group is used only for the December period where $\Delta R_3 = DM \cdot 1.8$ and $\Delta R_4 = DM \cdot 4$; in the technical optimization $\Delta R_3 = DM \cdot .2.1$ for June and December cases, and $\Delta R_3 = DM \cdot 2.25$ for March case. Nevertheless, the resulting layouts are rather different: the design condition of December (Fig. 2.9e and Fig. 2.9f) preferably places the heliostats north to the tower, similarly to the small field case. The layout related to June as design period independently from the spacing promotes the circular arrangement (Fig. 2.9c -2.9d).

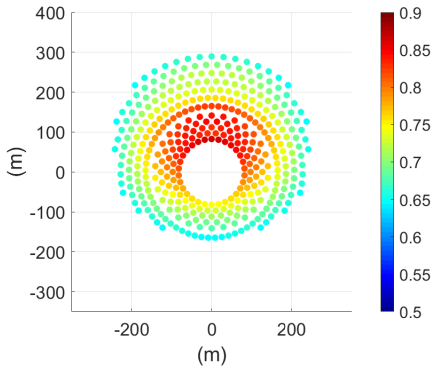

(a) *Ht = 110 m*

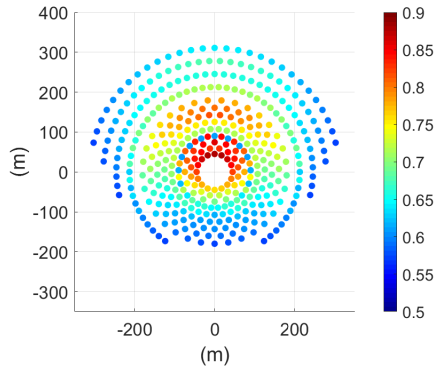

(b) *Ht = 60 m*

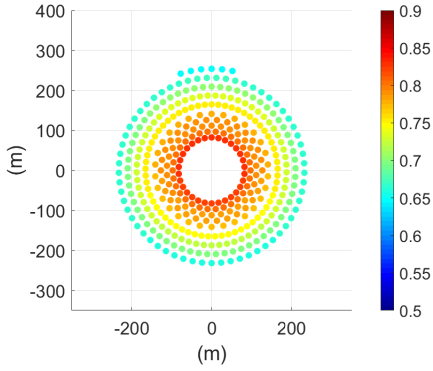

(c) *Ht = 110 m*

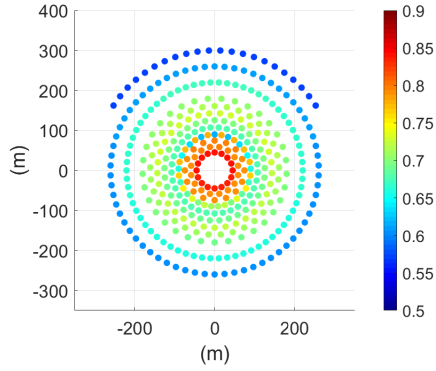

(d) *Ht = 60 m*

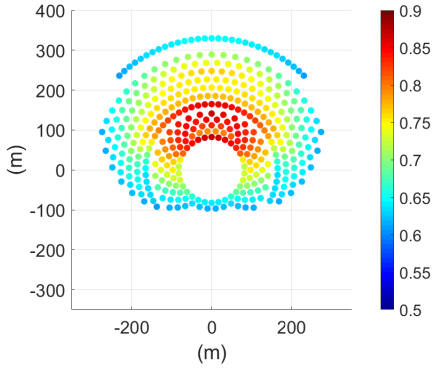

(a) *Ht = 110 m*

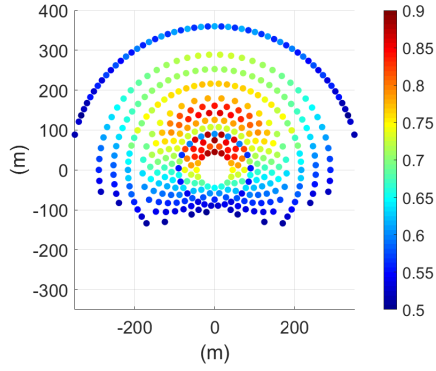

(b) *Ht = 60 m*

Figure 2.8: *Optimum technical (left: a,c,e) and economic (right: b,d,f) layouts and corresponding efficiency for different design periods (March: a, b; June: c, d; December: e, f) (Small field).*

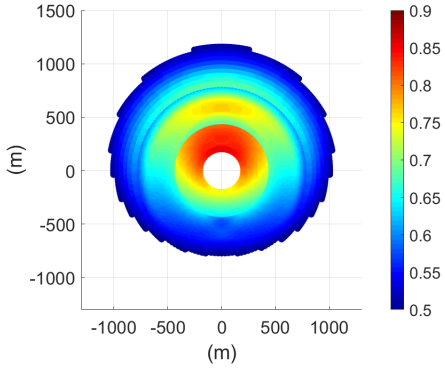

(a) *Ht = 270 m*

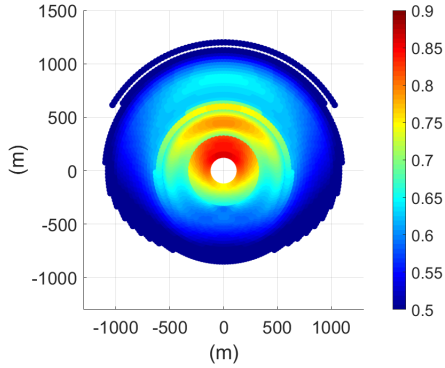

(b) *Ht = 210 m*

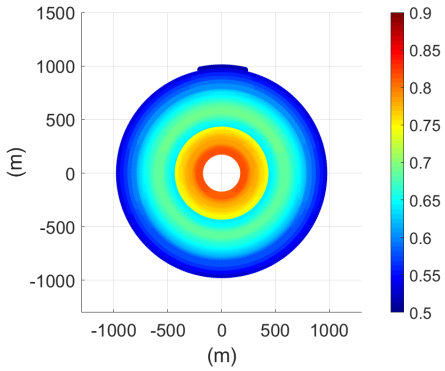

(c) *Ht = 270 m*

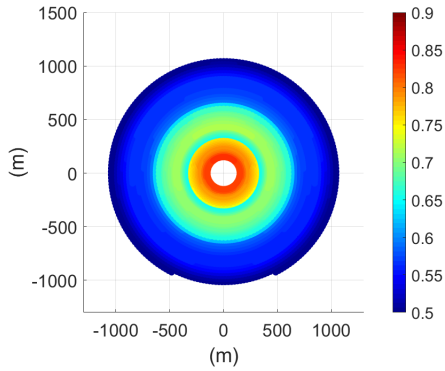

(d) *Ht = 210 m*

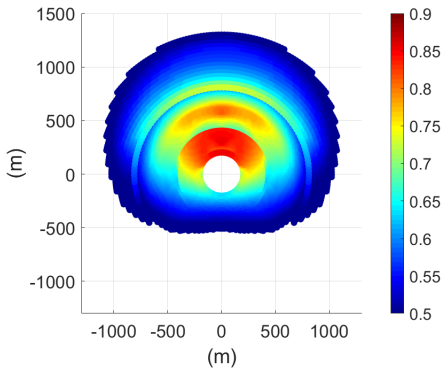

(e) *Ht = 270 m*

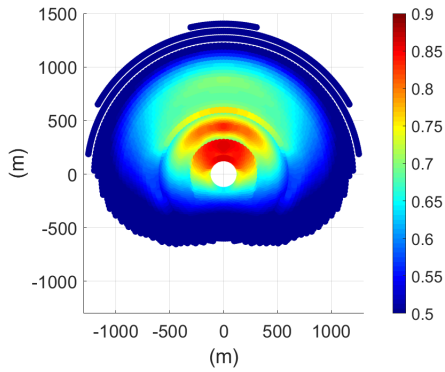

(f) *Ht = 210 m*

Figure 2.9: *Optimum technical (left: a,c,e) and economic (right: b,d,f) layouts and corresponding efficiency for different design periods (March: a, b; June: c, d; December: e, f) (Large field).*

In Table 2.5 and Table 2.6 the mirror distributions are reported with the specification of the maximum radius in the four-cardinal directions for small and large field respectively. With respect to the north-south direction the field is symmetric (only one radius R_{maxE-W} is reported), whilst in the north the extension is much greater than in the south. In the economic optimization, the field is generally more expanded in the north direction and a higher number of heliostats is placed in the lateral region (east-west).

Table 2.5: *Summary of optimum layouts (Small field).*

	$H_{t,opt}$ (m)	R_{maxN-S} (m)	R_{maxE-W} (m)	R_{groups} (m)	$N_{hpergroup}$ (-)
Technical optimization					
March	110	289.4	241.3	82.5	168
		164.8		165	232
				-	-
June	110	254	231.7	82.5	168
		231.7		165	232
				-	-
December	110	330	273.4	75	145
		105		150	240
				300	15
Economic optimization					
March	60	310.96	248.31	45	58
		180		90	173
				180	169
June	60	300	260	45	58
		260		90	173
				180	169
December	60	360	340	45	58
		130		90	148
				180	194

Table 2.6: *Summary of optimum layouts (Large field).*

	$H_{t,opt}$ (m)	R_{maxN-S} (m)	R_{maxE-W} (m)	R_{groups} (m)	$N_{hpergroup}$ (-)
Technical optimization					
March	270	1160	1025	202.5	1008
		773		405	4032
				810	1360
				1620	-
June	270	985.3	950.3	202.5	1008
		950.3		405	4077
				810	1315
				1620	-
December	270	1301	1068	202.5	1008
		528.1		405	3458
				810	1934
				1620	-
Economic optimization					
March	200	1200	1096	150	608
		850		300	2240
				600	3510
				1200	42
June	200	1043	1043	150	608
		1016		300	2224
				600	3568
				1200	-
December	200	1404	1254	150	608
		653.2		300	2268
				600	3079
				1200	445

For all solar fields, the most efficient heliostats are in the north sector and the maximum average efficiency is greater than 80% for mirrors located in the first row. An average efficiency of 45% is reached by the mirrors farthest from the tower. By comparing technical vs. economic optimum layouts, it is worth noting that the mirror fields determined by economic optimization exhibit a larger deviation between the most efficient and the least efficient heliostat.

2.3.2 Seasonal efficiency

The seasonal efficiency variability of the optimum layouts is here considered. In Fig. 2.10 and Fig. 2.11, the monthly average efficiency is reported for the two considered solar fields. The design period has a strong impact on the annual trend of the field efficiency this influence is more evident for the small field (Fig. 2.10). For both the optimum solutions (technical and economic) the layouts designed at June conditions show a plateau level in the summer

months and a dramatic performance reduction in winter (8 percentage points less). Conversely, the design with a lower Zenith ensure a better efficiency in the winter months. The polar configuration of the December layout is responsible for the performance penalization in summer: for the optimum technical layout (Fig. 2.10a) the efficiency is reduced by over 3.2 points, compared to the March layout. In the optimum LCOE layouts (Fig. 2.10b), the seasonal variations in March and December cases are mitigated due to the lower tower height, whilst the layout designed at June conditions shows the same belly-shape trend of the technical optimum configuration. Moving to the performance of the largest field (Fig. 2.11), the considered cases show a more uniform trends especially for March and June. The layouts designed at March conditions undergo a variation lower than 0.1 percentage point from April to August. Comparing technical optimum (Fig. 2.11a) and economic optimum (Fig. 2.11b) configurations, the general trend is similar, with an average efficiency 3 points lower for the layouts maximizing the LCOE.

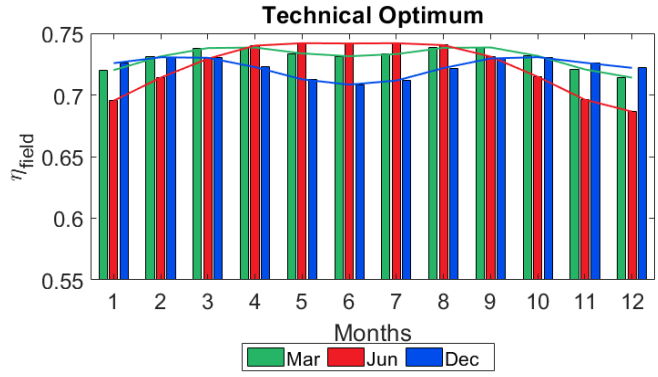

(a)

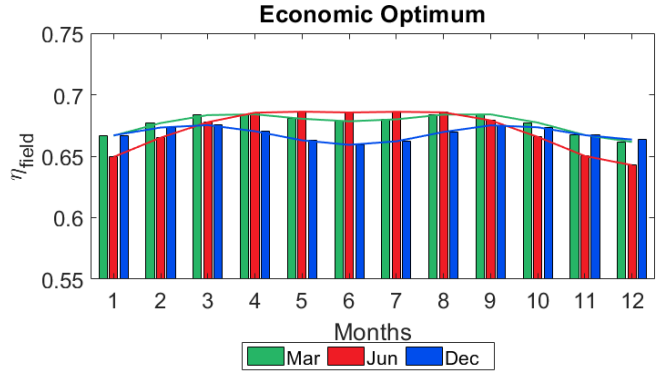

(b)

Figure 2.10: *Monthly efficiency trend of the technical optimum layouts (a) and of the economic optimum layouts (b) (Small field).*

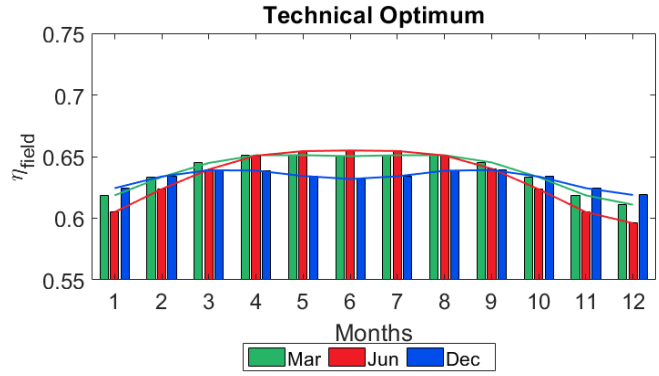

(a)

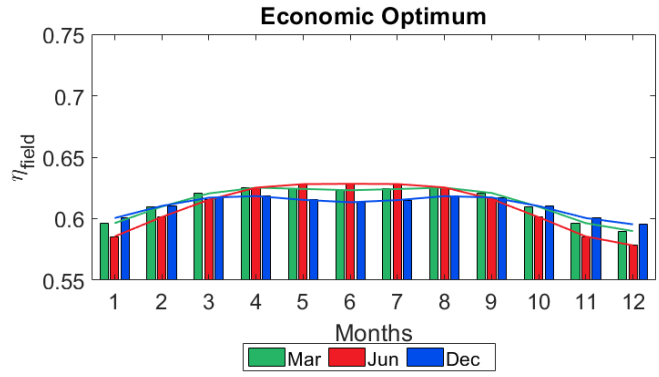

(b)

Figure 2.11: *Monthly efficiency trend of the technical optimum layouts (a) and of the economic optimum layouts (b) (Large field).*

Finally, the monthly energy collected by the receiver is considered in Fig. 2.12 and Fig. 2.13. The amount of collected thermal energy is highly dependent on the monthly trend of radiant energy (yellow line), but the seasonal variation of the efficiency previously discussed plays an important role. The results presented in Fig. 2.12 and Fig. 2.13 weigh the field efficiency values with the available solar irradiance, allowing to estimate the actual monthly yield. The efficiency penalization in winter for the layout layouts designed for June conditions is mitigated by the lower level of solar irradiation, whilst the penalty of December configuration is emphasized in summer months.
The annual collected energy into the receiver is summarized in Table 2.7. For both the sizes considered, the technical optimum layout designed for March conditions is the solution that maximizes the annual collected energy into the receiver (94.15 GWh and 1481.18 GWh, respectively). The energy collected with the economic optimum layout is lower by 2% and 4%, for the small and large size respectively; moreover.

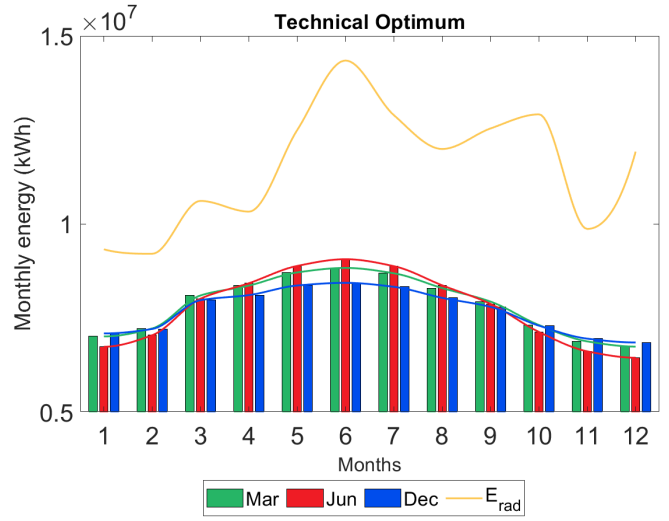

(a)

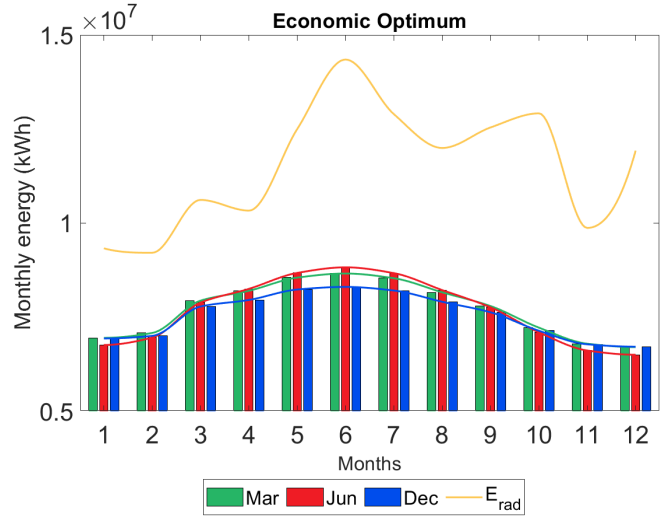

(b)

Figure 2.12: *Monthly energy collected by the receiver (Small field).*

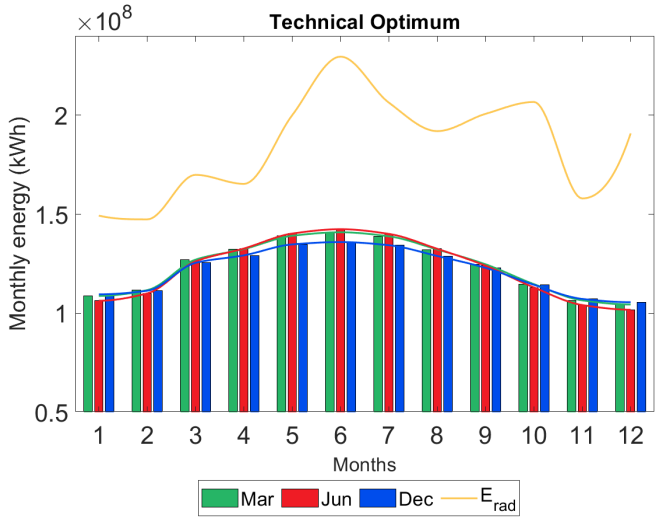

(a)

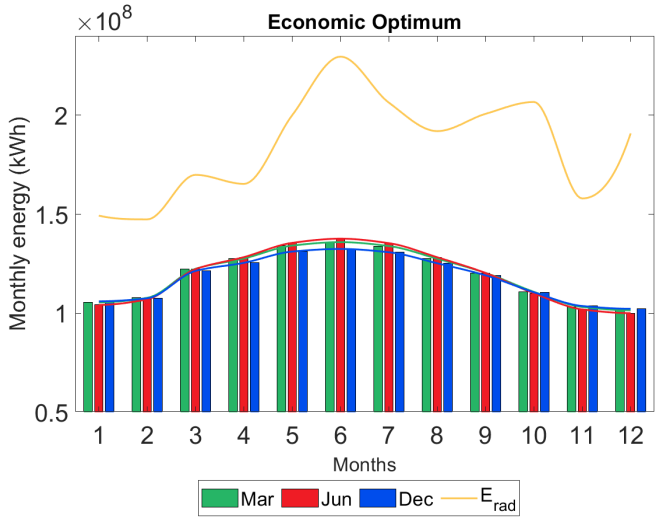

(b)

Figure 2.13: *Monthly energy collected by the receiver (Large field).*

Table 2.7: *Summary of energy collected from optimum layouts.*

Design period	$E_{abs}(GWh)$			
	Small field		Large field	
	Technical	Economic	Technical	Economic
March	94.15	92.60	1481.18	1430.69
June	93.53	92.23	1473.38	1431.03
December	92.50	90.61	1459.57	1415.66

2.4 Sensitivity cost analysis

The case with the best performance (i.e. the layout optimized for March conditions) is then analyzed more in detailed. It is well known that the economic evaluations are affected by a high level of uncertainty and some valid conclusions in the present can be denied in the future. This is particularly true in emerging markets like the CSP sector, where the costs show a large variability in dependence on several factors, including economies of scale and technological progress. Consequently, a sensitivity analysis has been carried out and is here presented, in order to show the impact of the unit costs of the main components (heliostats and tower) on the optimal plant configuration. The heliostat cost has been varied from 75 to 200 USD/m^2, with reference to the value suggested in [33] and [102]. Moreover, given the uncertainty of the tower cost model, three correlations are compared: the one proposed in the S.A.M. [85] and the two correlations presented by Turchi and Augsburger in [103] and [104], which correspond to the highest and to the lowest cost respectively (Fig. 2.14).

The variation of the LCOE with the cost of heliostats and tower is shown in Fig. 2.15a and Fig. 2.15b. Filled symbols are related to the budget cost presented in the section 3 (156 USD/m^2 for the heliostats and SAM correlation for the tower), whilst hollow symbols are the result of the sensitivity analysis. The heliostat unit cost variation leads to a pure shift of the LCOE curve (Fig. 2.15a), and therefore the optimization process is practically insensitive to such term. Furthermore, the optimum tower height does not change. Looking at Fig. 2.15b, the hollow symbols on the left-end of all curves refer to the Augsburger correlation, whilst the ones on the right-end refer to the Turchi correlation. The use of different cost correlations produces a modification of the optimum tower height, as documented by the labels reported in the figure. One can note that the influence of the tower cost is significant only for the small field, whilst the impact is weaker for larger sizes because the heliostat costs become dominant, despite of a significant variation of the optimum tower height.

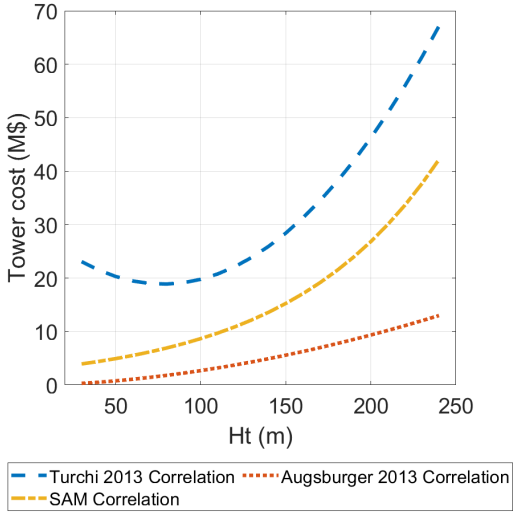

Figure 2.14: *Tower cost correlations.*

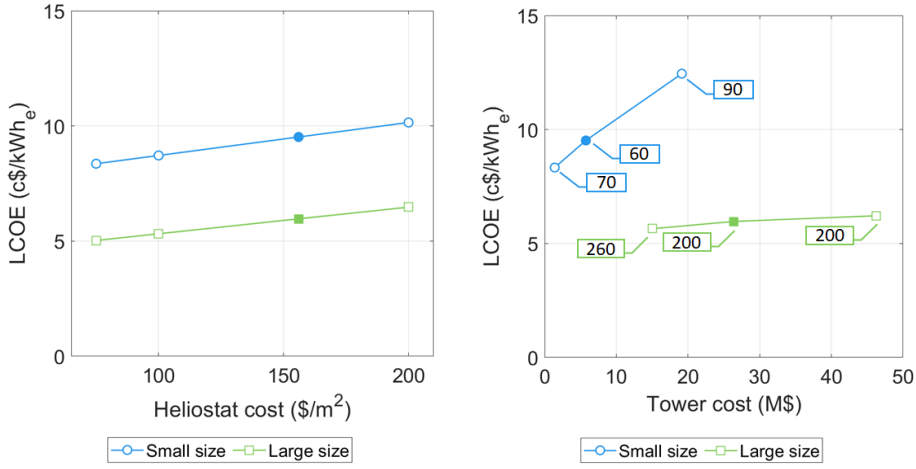

(a) *LCOE vs. Heliostat unit cost* **(b)** *LCOE vs. Tower cost*

Figure 2.15: *LCOE sensitivity analysis with components cost.*

2.5 Heliostat dimension sensitivity analysis

The higher level of investment cost is the most restraining features that nowadays is limiting the heliostat collectors to large-scale and high-irradiance-level applications [105]. Although increasing the level of irradiance could have the greater savings, a reduced capital cost of the plant can almost proportionally

reduce the level of LCOE [19]. Since the solar field can represent up to 50% of the investment, find a way to reduce the cost could be crucial: heliostat cost is strictly dependent on mirror area and a size optimization could have a great impact. The sensitivity cost analysis presented above is further investigated introducing an heliostat dimension analysis.
Open literature exhibits heliostat dimensions ranging from 1 to 180 m^2, and different are the opinion among the optimal size: one oriented to an increasing heliostat size and plant scale to reduce the cost [64], and one where smaller heliostat can lead to better efficiency [21]. Smaller heliostats can achieve better optical performance and Telsnig et al. propose a new concept of autonomous heliostats to reduce the installation and operation cost [18]. Some studies propose the use of different heliostat size in the same field, to increase the efficiency [48] and some others suggest that not only the dimension but also the shape of the heliostat could be changed minimizing the distance between heliostats [106]. Square, rectangular (with different aspect ratio) and also pentagonal shape were considered to find the solution that allows to reduce the cost [107]. Many are the correlation presented during past years and the Fig. 2.16 show a brief comparison: a general trend, such as presented by Blackmon et al. [108] , consider a cost curve that becomes steep as the heliostat size tends toward zero (because of greater fixed cost) and the slope of the curve is gentler as the heliostat sizes becomes large. Singhai points out that wind speed affects the cost since more robust and expensive frames are needed when the mirror surface increases. A cost-area correlation as function of maximum design wind speed (DWS) is presented in [15]: more the design wind speed is lower more the cost benefits large heliostat, until the cost becomes constant if a ridiculous wind speed (3 m/s) is considered. Increasing the design speed, a good compromise is found out for a 40 m^2 heliostat. Blackmon's and Coventry's [109] suggestions confirm that smaller mirror surface, ranging from 10 to 50 m^2, can lead to a cheaper solution. The recent trend underlined a reduced cost of 75 $\$/m^2$, justified by simpler structure and greater volume of production [102], thus the penalization for the smaller size can be considered negligible with a good accuracy. At last, combining the different model and suggestions available in literature [26, 108, 110], a new cost correlation model has been proposed, as reported in Fig. 2.16 (dark red line). A parametric analysis has been carried out and different heliostat size and shape (square and rectangular) are compared in terms of efficiency (design and annual) and LCOE, for a fixed total reflective area; the dimension investigated are reported in table 2.8 with the corresponding number of heliostats for the small and large case. The mirror cost per unit of area, calculated with the new correlation, is also reported.

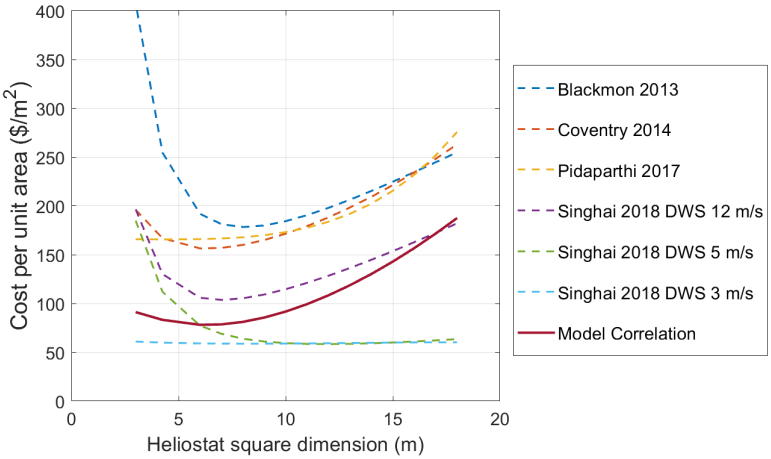

Figure 2.16: *Cost-Area correlations available in literature and the new developed model.*

2.5.1 Sensitivity analysis results

Once again based on the scheme of Fig. 2.1 and on the search space reported in table 2.2 , the analysis is repeated for all the heliostat sizes considered, assuming March as design period; the square heliostat 12x12 is set as reference size for the comparison with different width-height proportion. In Fig. 2.17, the influence on the geometrical spacing that maximize the design efficiency is investigated (dR_2 and dR_3 for the small field and dR_3 and dR_4 for the large field) and no relevant deviation are observed from the reference case. When different shape are investigated (right charts), a slight more irregular behavior is detected and the radial spacing is minimized for the solution "6x9 m". Comparing the solutions "9x12 m" and "12x15 m" with the reference "12x12 m" it is possible to affirm that the optimal radial spacing, especially for the farthest group, is more influenced by the heliostat height than the width.

In Fig. 2.18-2.19 the performance parameters are shown and the heliostat size influence is more pronounced. In the small case (Fig. 2.18a) an interesting trend of design efficiency is observed: a well defined optimum of 73.7% is found for a tower height around 110 m. Up to Ht 110 m, smaller is the size greater is the efficiency; after the optimum the trend is opposite, the largest heliostat benefits most by an higher tower. Analogously, the annual efficiency (Fig. 2.18c) exhibit the same trend with a level lower of around 10.5%; the heliostat with a width/height ratio greater than one have a better annual efficiency than square reference dimension. Introducing the economic performance, the optimum tower height becomes much smaller suggesting that the tower cost has a relevant impact; the heliostat cost correlation clearly highlights the difference between mirror size and accentuating the penalty of greater heliostat

Table 2.8: *Definition of the heliostat parameters.*

Dimensions h x w	Heliostat mirror area	Mirror cost per unit area	Number of heliostats	
(m)	(m^2)	$\$/m^2$	Small field	Large field
Variable size cases				
6x6	36	78.16	1600	25600
9x9	81	85.57	712	11378
12x12	144	108.37	400	6400
15x15	225	142.91	256	4096
18x18	324	187.34	178	2845
Variable shape cases				
6x9	54	79.23	1067	17067
9x12	108	94.53	534	8534
12x15	180	123.34	320	5120

for smaller tower height. The cheapest solution (8.25 ¢$/kWh$) correspond to a heliostat size of 6x9 m with a tower height of 50 m; despite the cost per unit area greater of 1.35%, the better annual efficiency (+0.7%) than the square solution of 6 m has a greater impact on the LCOE. Increasing the heliostat size, the optimum moves to higher tower to compensate the lower annual efficiency.

Moving to the large field case Fig. 2.19, greater is the tower, greater is the efficiency and smaller heliostats generally perform better (+1.34%). A maximum efficiency of around 64.7% is reached with a tower of 270 m. A width/height ratio of 1.5 (6x9 m) allows superior annual performance (+1.5%) than the better square solution of 6 m ($\eta_{ann} = 58.48\%$). Finally the LCOE (Fig. 2.19e) shows a greater differentiation between the different sizes but to a lesser extent than the small field. The economic function shows a little variation with the tower height but a minimum point is identified for Ht = 210 m for all the sizes considered. According to a better efficiency, the heliostat with dimension 6x9 m, minimize the LCOE (5 ¢$/kWh$); whilst the largest mirror can't drop below 6.35 ¢$/kWh$.

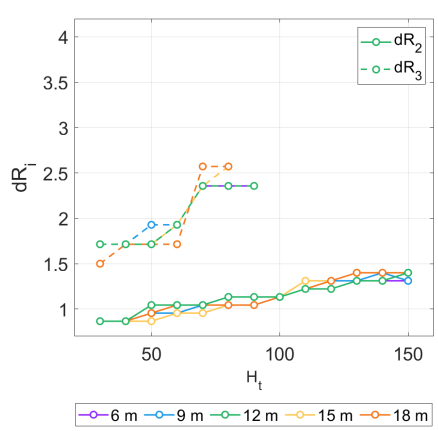

(a) *Small field variable size*

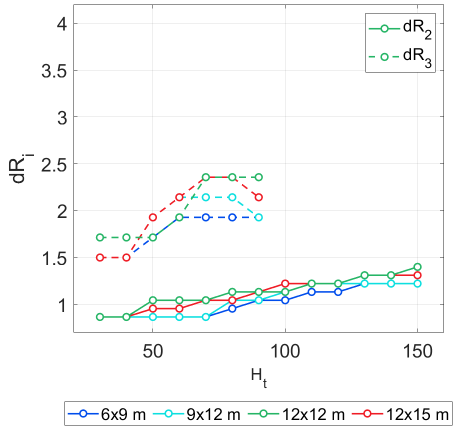

(b) *Small field shape*

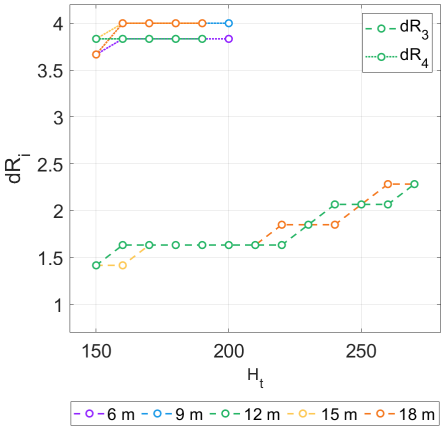

(c) *Large field size*

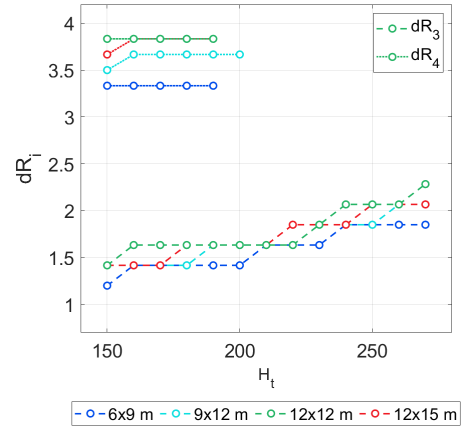

(d) *Large field shape*

Figure 2.17: *Radial spacing varying tower height for small (a & b) and large field (c & d).*

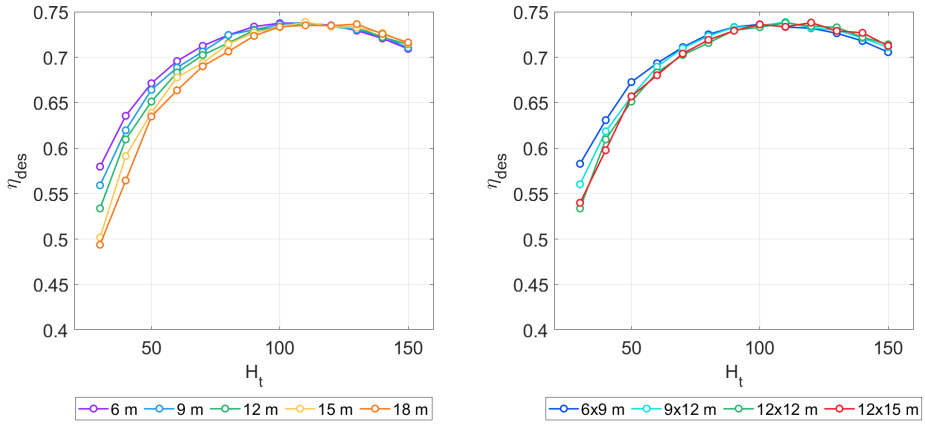

(a) *Design efficiency*

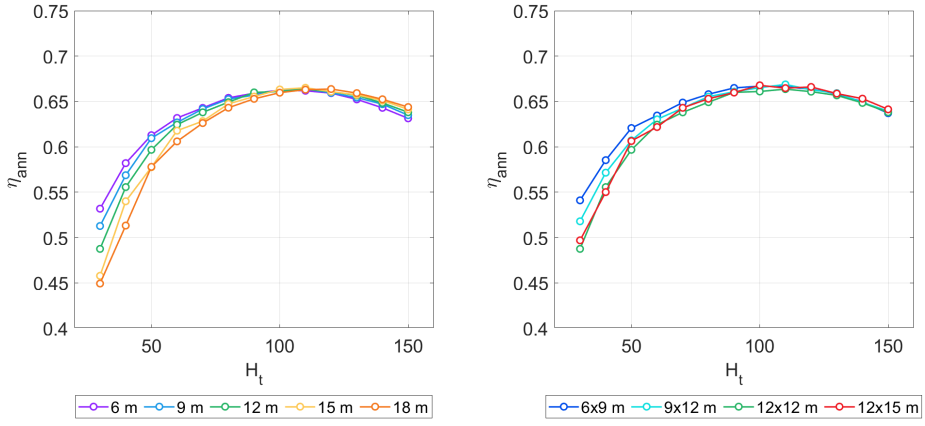

(c) *Annual average efficiency*

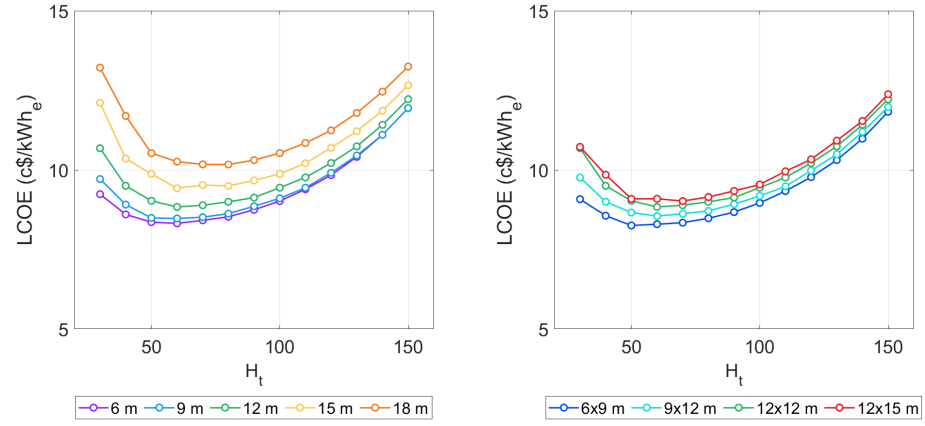

(e) *LCOE*

Figure 2.18: *Performance parameters vs. tower height for different heliostat size (left) and shape (right) (Small field).*

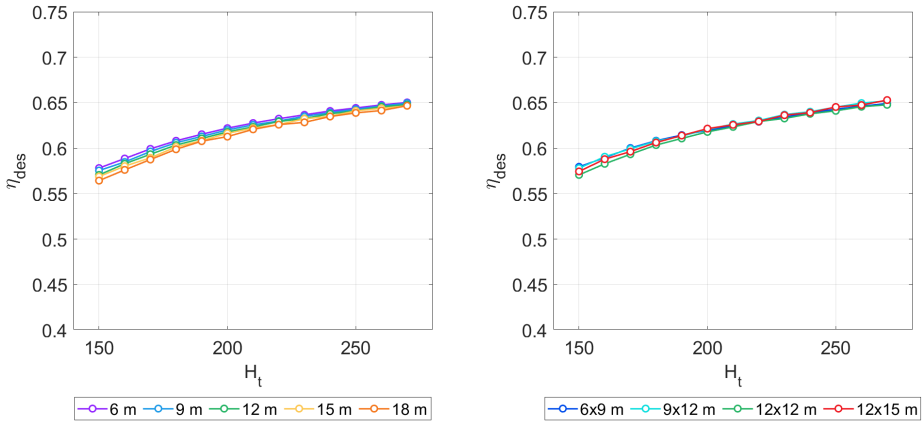

(a) *Design efficiency*

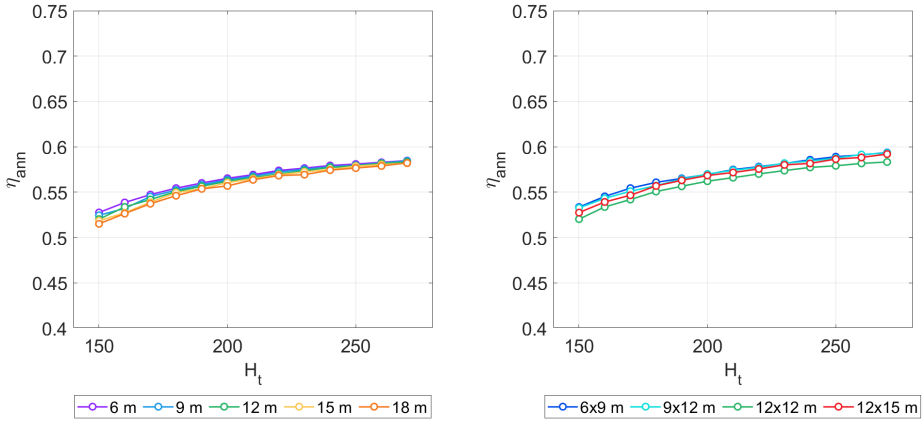

(c) *Annual average efficiency*

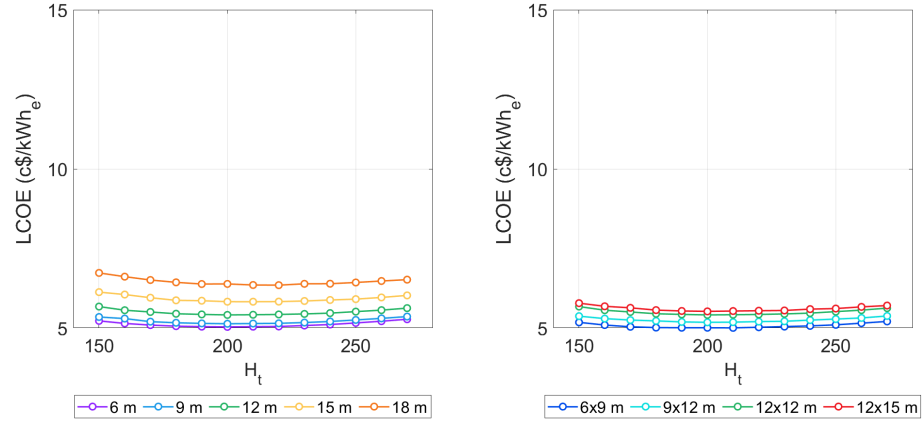

(e) *LCOE*

Figure 2.19: *Performance parameters vs. tower height for different heliostat size (left) and shape (right) (Large field).*

CHAPTER 3

Receiver Dimension

3.1 Introduction

The receiver is a crucial component for the solar tower system. Firstly, this is due to its economic impact on the total investment costs, comparable to the one of the heliostat field as reported by Augsburger and Favrat [104]. Moreover, the receiver configuration directly influence the performance of each heliostat, according to its position, and then imposes the shape to the field [111]. External cylindrical or cavity are the most diffuse configurations that implies a surround or north field distribution, respectively. Several aspect are considered to determine the convenience of one solution compared to the other: in the cavity, higher spillage losses occur but reflection and radiative losses are limited since the heated surface are protected by a smaller aperture; the surround field is less penalized in efficiency when the condition are different from the design point.

The performance of the receiver directly affect the plant's output power, as pointed out by Hassan in [112] and many authors investigate solutions to improve its efficiency. Rodríguez-Sánchez et al. [113] propose a receiver able to withstand to high fluxes: two zones are present in each panel in which the velocity of the fluid could be handled independently. As pointed out by Wang et al. [114], a vertical finned structure can increase the efficiency by 3.2%; whilst Fleming et al. implement a multi-cavity system that can ensure a thermal

efficiency greater than 90% and an effective absorption of almost 99.8% [115].

The optimization of the entire CRS system involves a large number of variables and could be computationally burdensome. Ramos and Ramos [34] applied the "*Nevada solar plant optimization code*" (NSPOC) to speed up the optimization process and define the best combination of 11 design variables (including receiver and heliostat layout). The sensitivity analysis provided by Luo et al. [40] brings out that the interaction effect between the subsystem in the CRS plant has a strong impact on the possible decomposition of the optimization problem; however, it is demonstrated that the heliostat layout and the receiver are independent and the optimization of the CRS system could be split in two separated procedures [40]. Collado and Guallar [33] once optimized the tower and heliostat field consider the receiver design based on an economic optimization. In the paper proposed by Carrizosa et al. [52] a greedy-based heuristic algorithm is used to optimize the receiver minimizing the LCOE.

Venkatesh et al. pointed out that spillage losses can be 15% of the optical losses [116] if the receiver size is not optimized, and thermal losses (convective and radiative) can be significant, being proportional to the receiver area. The receiver must be large enough to not penalize the performance of the heliostat field and to guarantee the maximum allowable flux limit, generally about of $1 - 1.2 MW/m^2$ for a solar tower with molten salt [30]. The maximum flux incident to the receiver surface is function of the surface material and the operative conditions, as molten salt temperature and velocity [117]. Without any control strategy, peak flux values exceed the maximum more than double (2-5 MW/m^2) and the receiver is subjected to excessive stress on the material and accelerated damaging effects due to local overheating [81]. In order to limit the flux intensity two are the main strategies adopted: defocussing of some heliostat sectors or adjusting the aiming strategy to keep the flux as uniform as possible over the surface to maximize the energy transfer efficiency [118]. An equatorial aiming strategies does not ensure a realistic performance prediction but, in general, is over-estimated: a controlled penalty between an uniform solar flux distribution and a maximum spillage efficiency must be selected [119]. The work of Ashley et al. [120] is mentioned as examples of various studies that investigated on aiming strategies to homogenize the flux over the receiver surface; otherwise, Servert et al. focus on the impact of the aiming strategy on the receiver optimal size [121].

With the suggestion on optimization decomposition, the analysis of the receiver influence on the energy collected by the system has been carried out for fixed field layouts. The annual efficiency and the LCOE profiles are studied to underline the different influence of the technical or economic objective function on the final best configuration. The analysis is repeated for two field sizes and the convenience of a cavity receiver is evaluated for the smallest field.

3.2 Receiver optimization

For a given set of design and thermal constraints, the absorber area is generally proportional to the peak thermal rating. The optimal receiver size is the result of the trade-off between spillage losses, receiver thermal losses and peak flux limitation. It is worth noting that the optimal dimensions are more restricted by the peak limitation, and even if the influence of the aiming strategy on the global efficiency is small [121], it is the only parameter that allow to manage this limitation: Sánchez-González et al. in [84], and later Collado and Guallar in [122], observe that for a surround field, an aiming factor k_{aim} near to 2 reduces the peak level into the limit range without penalizing the spillage efficiency more than 1% .

In this discussion, the receiver is considered with the influence of the tower height H_t since directly affect the energy level that reach the receiver. The optimization process is distinguished into two step, as schematize in Fig. 3.1:

- first, for each tower height investigated the best parameters (D_{rec} and HD_{rec}) are determined to find the extrema of the objective function; among all investigated solutions, during the selection process, the peak flux values are verified.
- along the available tower height, the solution (that includes optimized and fixed layout and receiver dimensions) that ensure the best objective function is selected.

The performance model adopted and the main assumption on the adopted receiver structure are described in the section 1.3. Moreover, based on the breakdown approach of Luo et al. [40], the provided layout associated to each tower height are results of the technical (first step) optimization of the previous chapter, assuming the 21^{st} March solar noon as design period (such as the heliostat field presented in figures 2.8a, 2.8b, 2.9a and 2.9b).

Usually the economic analysis is carried out after the technical optimization but in this way, the correct evaluation of the minimum of the economic function could be altered. For this reason, two distinct optimization process are considered and the resulting configuration are compared. The two objective functions considered are the absorption efficiency (Eq. 1.28) and the LCOE (Eq. 1.42).

When a cavity receiver is considered, additional variables must be introduced in the optimization: instead of D_{rec} and HD_{rec}, the dimensions of the aperture W_{ap} and HW_{ap}, and the diameter of the absorber W_{rec} are considered. The aperture size and the geometry are chosen to minimize the sum of thermal and spillage losses [111]. The exact configuration of the cavity enclosure influence the distribution of the flux on the absorber surface, and therefore, the prediction of the energy collected is not damaged with a simplified structure. The peak flux usually occurs along the back centerline and to reduce peak flux

values, it is sufficient to move the absorber surface away from the aperture (increasing the distance, the local spots are more distributed along the total receiver height, since the aim point is considered at the center of the aperture), or alternatively, the aiming point along the aperture are re-distributed. After the calculation, the values of the flux along the height are checked to determine the minimum panel length that does not damage the energy collected.

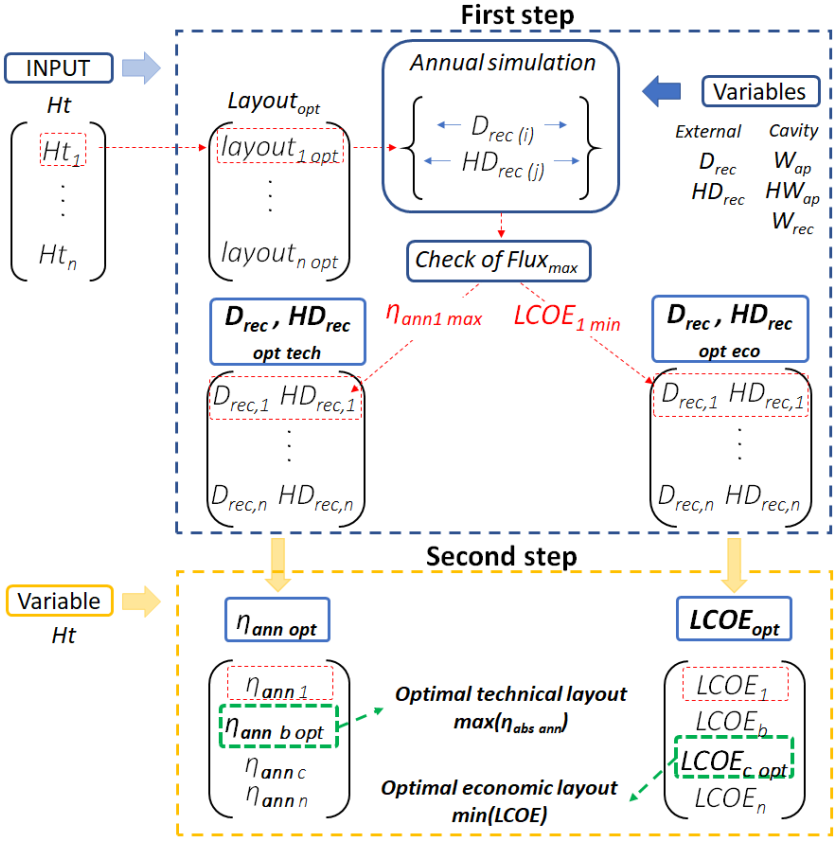

Figure 3.1: *Scheme of the two-step optimization algorithm.*

3.2.1 Methods and tools

The simultaneous optimization of tower and receiver is considered to be the extension of the field analysis provided in the chapter 2. The same assumption of field dimension and meteorological condition shall be held constant; the main parameters of the receiver subsystem are reported in Tab. 3.1, differentiating between cavity and external geometries. The aperture tilt angle is kept constant and equal to 12.5°, as suggested by Carrizosa et al. in [52] according to the thermal power. A later analysis should consider the effect of this parameter

on the efficiency.

Table 3.1: *Definition of the main parameters of the receiver subsystem.*

Parameter	unit	External	Cavity
Emissivity ε	-	0.9	0.8
Absorptance α_{eff}	-	0.95	0.97
h_{mix}	(W/m^2K)	16.61	23.24
Aperture tilt	(deg)	-	12.5

As already commented, the optimization functions considered are non-convex and their evaluation is computationally expensive. A direct search method is preferred and a sensitivity analysis has been carried out to easier identify the most influencing variables. The explored values are reported in table 3.2.

First, the external receiver is considered comparing two field size, a small and large application, please refers to Tab 2.1 for the parameters related to the field. Consequently, the attention is moved to the small field where the comparison between external and cavity structure is introduced; few comments about the field layouts associated to the cavity receiver are also provided.

Table 3.2: *Definition of the search space of tower and receiver subsystem.*

Variable	Unit	Range		Step
		Small	Large	
D_{rec}	(m)	3-8	12-20	0.5
HD_{rec}	-	1-1.2		0.1
W_{ap}	(m)	3-8	-	0.5
HW_{ap}	-	0.7-1	-	0.1
W_{rec}	(m)	5-11	-	0.5
Ht	(m)	30-150	150-270	10

3.3 Results

Based on the model presented in the previous sections, the dependence of the annual absorption efficiency and the LCOE with the tower and receiver is investigated and the main interactions between the subsystems are observed. The analysis for the small field, with an external receiver, is presented in Fig. 3.2. When the optimal efficiency (Fig. 3.2a) is considered, a constant receiver diameter of 5 m is selected up to 100 m, over this limit the diameter is increased by 0.5 m mainly due to the flux limit, in fact, the first part of level curves for higher H_t are cut off. Moreover, the level curves are approximately parallel to each other that suggest that no influence is observed between the effect of D_{rec} and H_t on the efficiency. Increasing the tower height a greater absorption

efficiency is observed and a asymptotic value of 59.5% is achieved from 110 to 150 m; whilst for smaller Ht the penalization can reaches 40% (η_{abs} of 0.418 for a tower of 30 m). Moving to the economic function a quite different trend is observed (Fig. 3.2b); first of all a clear minimum point of $0.096\$/kWh$ is find out for a tower height of 60 m and away from the best point, the cost increase is relevant: from 0.1 to 1 ¢$ every 10 m. Optimizing the cost a smaller receiver diameter is preferred for small tower (4-4.5 m), whilst for H_t greater than 100 m, once again, the flux limit has more impact than the performance and forces to larger and higher receiver. In the right chart of Fig. 3.2c, it is highlighted that the minimum feasible receiver diameter guarantees the minimum cost; furthermore, it is observed that the interaction between tower and receiver is somewhat pronounced especially for tower height lower than 70 m where the cost increment is more marked when the receiver is larger than the optimum.

Shifting the attention to the large field size, when the combined receiver and field efficiency is maximized, the best absorber area decreases when the tower height increase (Fig. 3.3a); whilst, a slight smaller diameter is obtained in the economic optimum for higher tower height but the receiver area is always increasing according with a greater receiver height (Fig. 3.3b).The technical optimal receivers are larger than the economical solution by more than 10%, and increases to almost 38% when the tower is lower than 180 m. Conversely to the small case, it is worth noting that the influence of the geometrical parameters is even lower: the gain in efficiency related to a higher tower height is always lower than 1 point percentage (every 10 m) and the maximum LCOE deviation from the cheapest solution is within 2%. This trend is confirmed by the rather flat level curves in Fig. 3.3c: the absorption efficiency is more influenced by the tower height than the receiver, conversely, the combined effect of the tower cost and the annual energy collected nullify any relevant advantage and even very different solutions are equivalent.

Finally, in table 3.3 the solutions that maximize the annual absorption efficiency or minimize the LCOE function are reported for the two field size considered. The best technical solution is characterized by an higher tower and larger receiver: the thermal losses of the hot absorber surfaces are compensated by a greater field optical efficiency reaching a $\eta_{ann,abs}$ of 0.5955 and 0.5324. In the economic optimization, the component cost has a key role in the sizing of each subsystem; reducing the tower height by 60 and 80 m and the receiver aperture by 41.8% and 21.6%, for the small and large field respectively, a minimum LCOE of 9.6 and 6.02 $¢\$/kWh$ is achieved. As commented before, the larger field size is less sensitive to configuration away from the best: the electricity cost is damaged by only 5.2% with the technical optimum solution, and the same order of magnitude for the efficiency penalization is realized if the LCOE is minimized. Conversely, the small field exhibit penalty of more than

10% and 25% for the efficiency and the LCOE respectively.

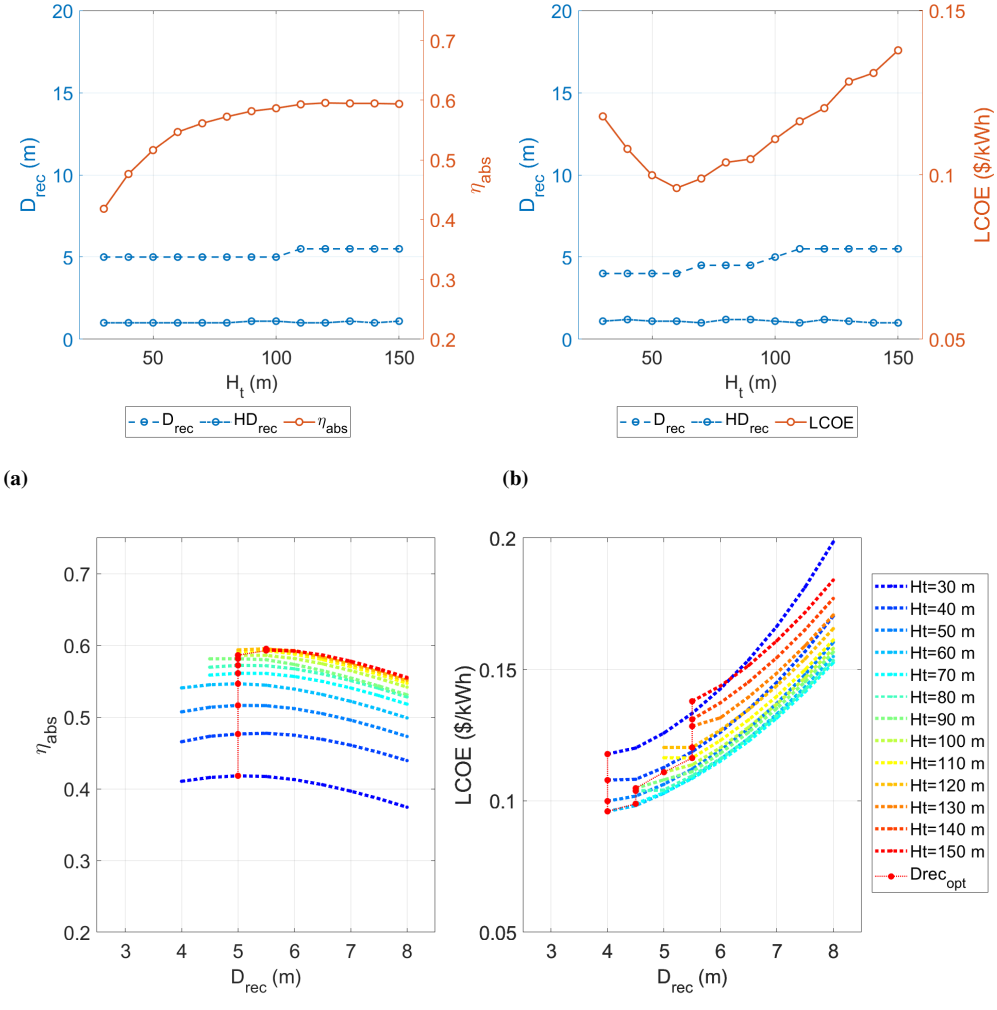

Figure 3.2: *Tower and receiver influence on absorption efficiency and LCOE for the small field.*

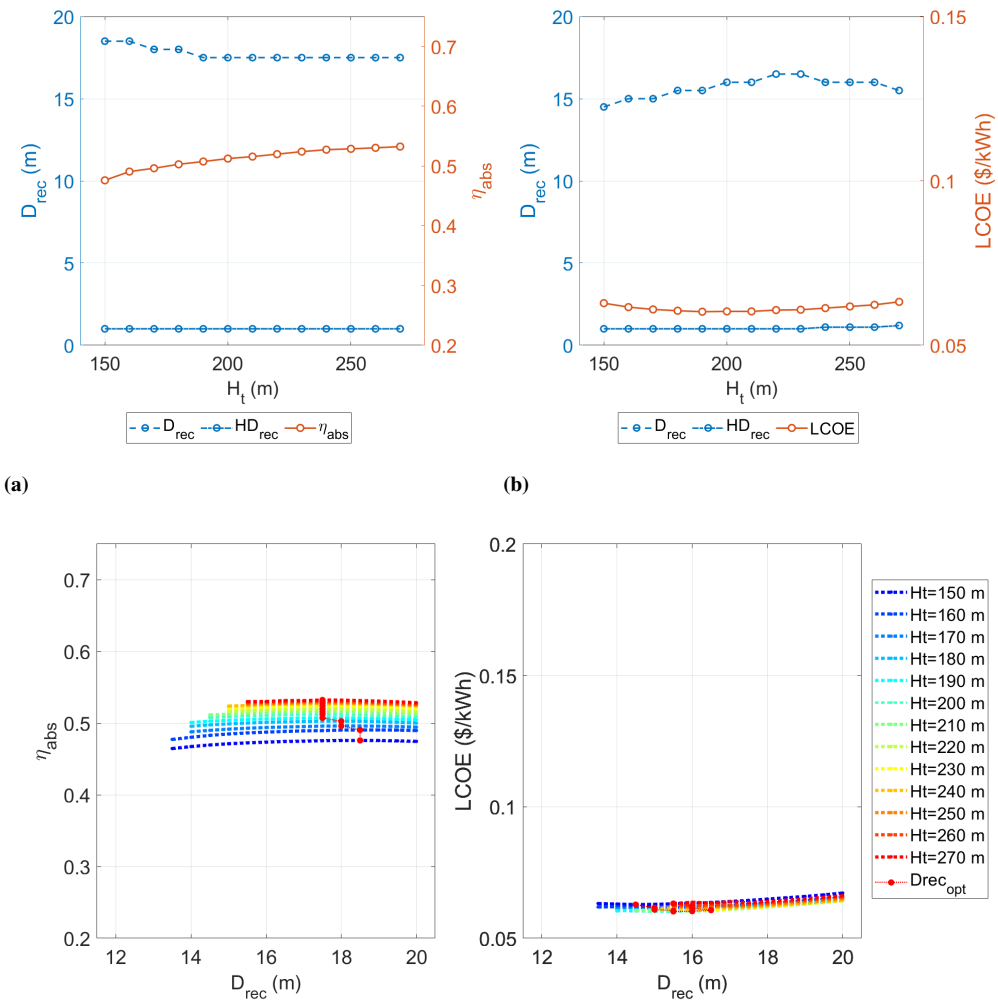

Figure 3.3: *Tower and receiver influence on absorption efficiency and LCOE for the large field.*

Table 3.3: *Summary of optimization results.*

Field	*O.F.*	H_t (m)	D_{rec} (m)	A_{rec} (m^2)	$\eta_{ann,abs}$ (-)	$LCOE$ $(\$/kWh_e)$
Small	Techn	120	5.5	95.03	0.5955	0.1203
Small	Eco	60	4	55.29	0.5396	0.0960
Large	Techn	270	17.5	962.11	0.5324	0.0635
Large	Eco	190	15.5	754.77	0.5040	0.0602

3.3.1 Cavity receiver

When the application scale is reduced to low thermal rating power (like the treated $30MW_{th}$) a cavity receiver configuration could be more economical. The figures 3.4a and 3.4b show the results of the receiver optimizations (the size of the aperture W_{ap}, HW_{ap} and the absorber diameter W_{rec}) for different tower height: it is worth noting that no significant variation are observed if the technical and the economic function is considered. When the tower is lower than 60 m the aperture is quite larger than the hot surface to compensate the low optical efficiency with a limited spillage effect and maximizing the absorption efficiency the aperture area is larger by almost 13% than the cheapest case. The parameter W_{rec} is handled to guarantee the flux limit on the receiver surface and remains unchanged with different objective function, this behavior suggest that the effective absorber area is more limited by the heat flux than the cost or the thermal losses.

Similarly to the external case, it is recognized an increasing trend of the absorber performance with the tower height (Fig. 3.4a), whilst le LCOE function benefit smaller H_t between 50 and 70 m (Fig. 3.4b). However, it is underlined a different influence of the receiver main dimension. With reference to (Fig. 3.2c), the right size of the Fig. 3.4c shows that greater is the aperture, greater is the efficiency and an asymptotic tendency, when the tower is higher than 70 m allows to slightly reduce the aperture width to 7.5 m. At the same time, the penalization for low W_{ap} is larger increasing the H_t. An opposite trend is observed for the LCOE (Fig. 3.4c right chart) that present a minimum for an aperture of 7 m for most tower heights considered and reducing the width the lower absorbed energy rising the cost per kWh.

The optimization results for the two function are reported in table 3.4. The economic solution benefits most from a reduced cost of the tower component and despite a greater receiver area than 29.4%, the LCOE is lower than 30% and the efficiency is reduce only by 11.6%. Compared these configuration with the external receiver optimal, it should be pointed out an area 55% larger in the technical case that is mainly responsible for the LCOE of 12.03 $¢\$/kWh$, with an increased investment cost and higher thermal losses that damage the absorption efficiency. Analogous effect is observed in the economic solution, even if the receiver area is just smaller (55.29 vs. 61.1 m^2).

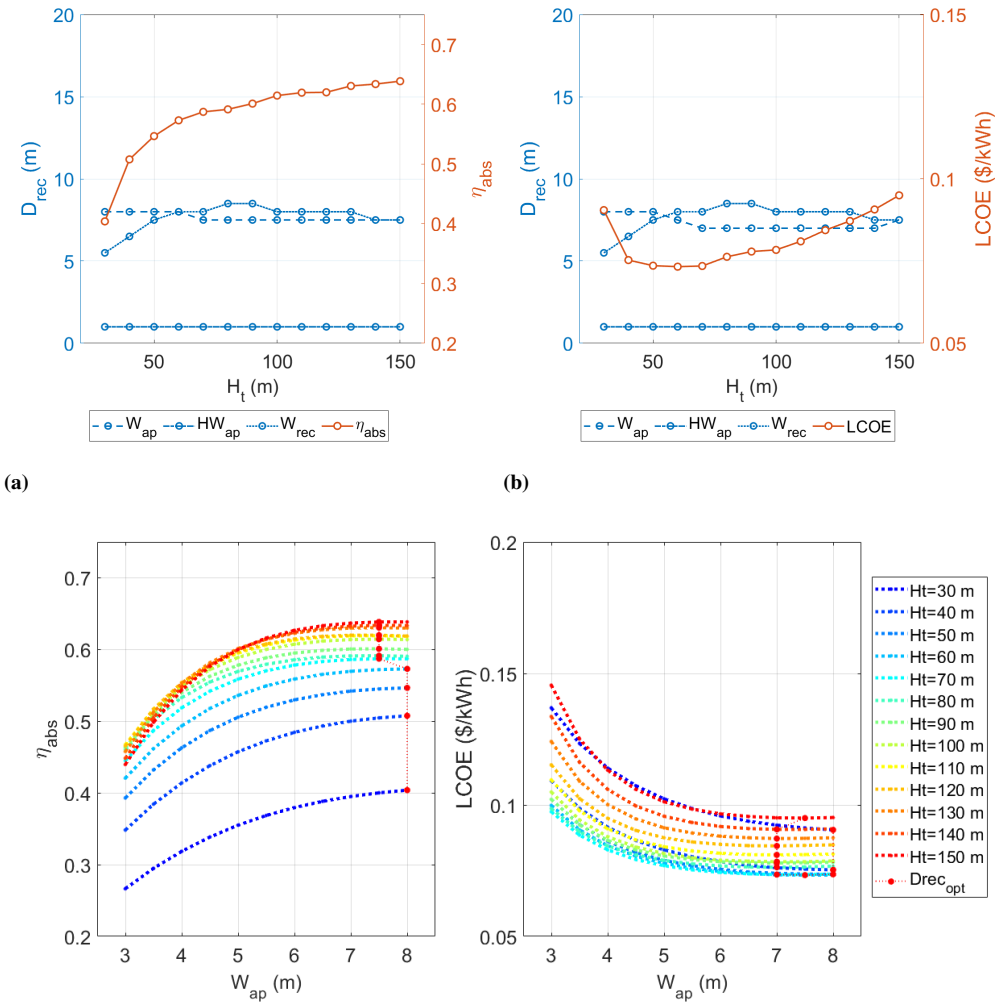

Figure 3.4: *Tower and receiver influence on absorption efficiency and LCOE for the small field with cavity receiver configuration.*

Table 3.4: *Summary of optimization results: comparison between cavity and external receiver.*

Field	*O.F.*	H_t (m)	W_{ap} (m)	A_{ap} (m^2)	D_{rec} (m)	A_{rec} (m^2)	$\eta_{ann,abs}$ (-)	$LCOE$ $(\$/kWh_e)$
Cavity	Techn	150	10.5	110.25	7.5	43.13	0.6385	0.095
Cavity	Eco	60	7.5	56.25	8	61.098	0.5720	0.0733
External	Techn	120	-	-	5.5	95.03	0.5955	0.1203
External	Eco	60	-	-	4	55.29	0.5396	0.096

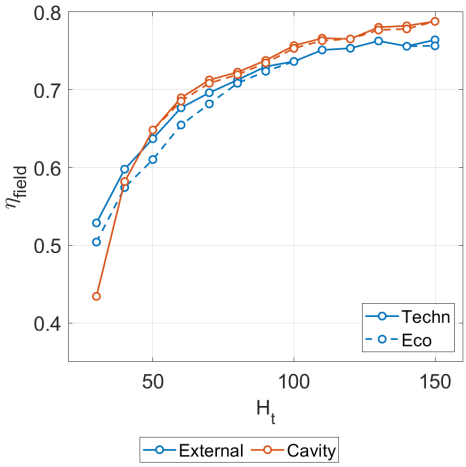

(a) *Field design optical efficiency*

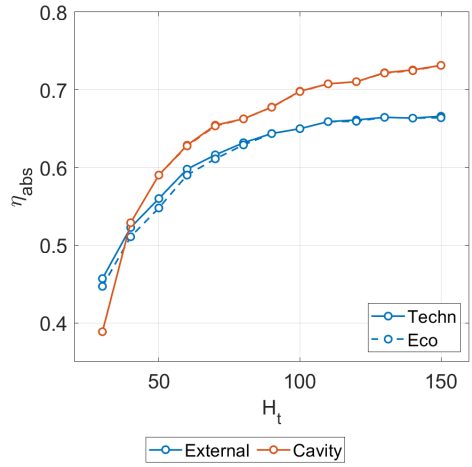

(b) *Design absorption efficiency*

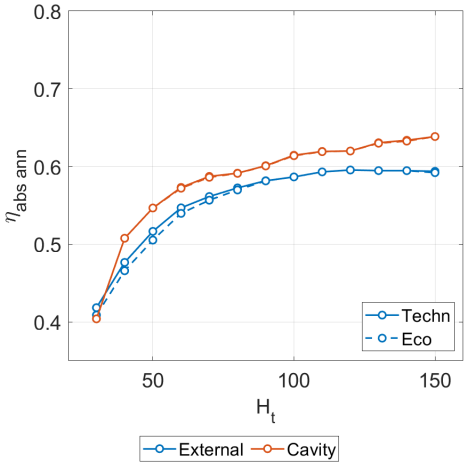

(c) *Annual absorption efficiency*

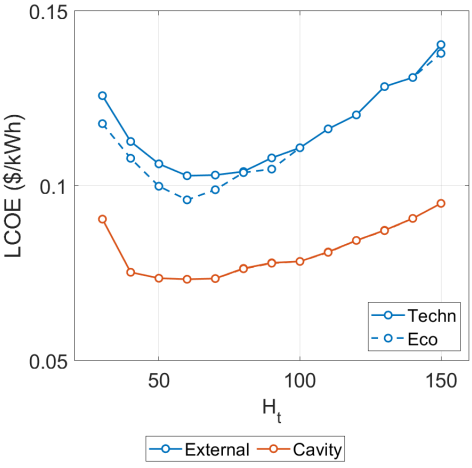

(d) *LCOE*

Figure 3.5: *Comparison of the main performance of the field-receiver system for the external and cavity configurations, for the two optimization function (technical and economical).*

In Fig. 3.5 the cavity-external comparison is extend to the main performance parameters (i.e. field efficiency η_{field}, design and annual absorption efficiency η_{abs},$\eta_{abs\ ann}$ and LCOE) and their variation with the tower height. Once again, the difference between technical and economic optimization for the cavity is negligible and the maximum deviation, observed for the optical efficiency, is always lower than 0.6%. Whilst, the external case is more influenced by the objective function, especially for lower tower height. A general trend is noted for all the efficiencies considered where the optimized cavity

guarantee greater performance except for the smaller H_t. Introducing the receiver efficiency (Fig. 3.5b) the performance curve is flattened increasing the tower and the cavity benefit are emphasized. Extending the analysis period to the whole year, weighing the efficiency with radiation levels, no significant variations are introduced except a small reduction (from 8% to 5%) of the main different between the two solutions. Finally, the economic function further penalizes the external receiver for small scale application since, as commented above, the investment cost is not convenient and the LCOE is greater of almost 40% for all the height investigated.

Layout comparison

For the sake of completeness, the influence of the cavity receiver geometry on the heliostat field layout is analyzed in details. It should be remembered that due to physical constraints related to the cavity geometry, the layout distribution is limited to the field area north of the tower. First, the results of the geometrical parameters, based on the optimization procedure presented in the section 2.2, is reported in Fig. 3.6. It is observed that, compared to the surround configuration (blue), a more compact solution is preferred to limit the attenuation losses of furthest heliostats. Moreover, the third group is adopted up to a tower height of 130 m, instead of 90 m, confirming the presence of an higher number of mirror with a large distance from the center.

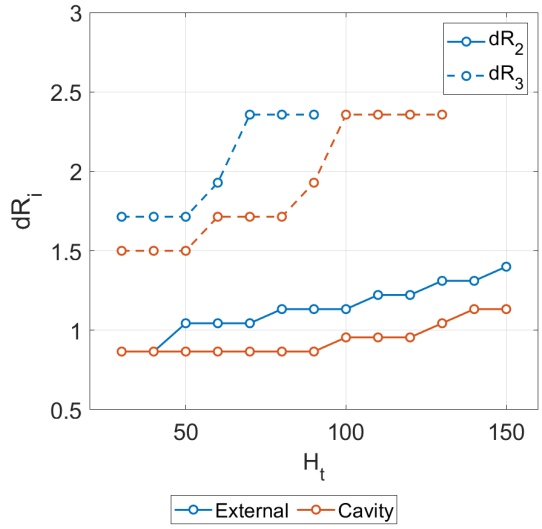

Figure 3.6: *Radial spacing vs. tower height corresponding to the layout for external and cavity receiver*

The layout corresponding to the best technical and economic solution are

shown in Fig. 3.7 and the advantages of the polar configurations are underlined by the design efficiency of each mirror; it is interesting to note that although the greater extension of the field in North direction (up to 600 m in Fig. 3.7a), the heliostat performance is more uniform along the field and always greater than 60%. The economic layout are densest to compensate a lower tower height but the occupied land is almost doubled with the cavity geometry, whilst only 22% higher in the external configuration.

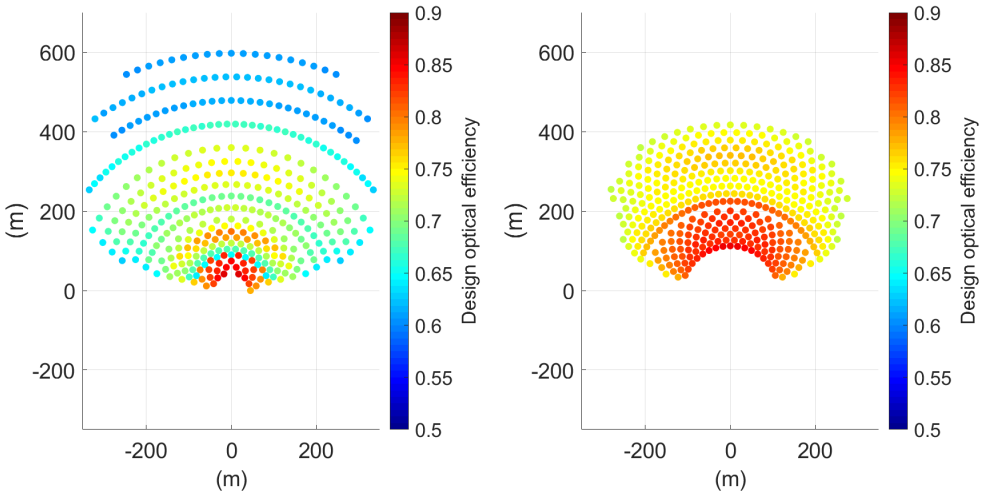

(a) $H_t = 60m$, *cavity receiver*

(b) $H_t = 150m$, *cavity receiver*

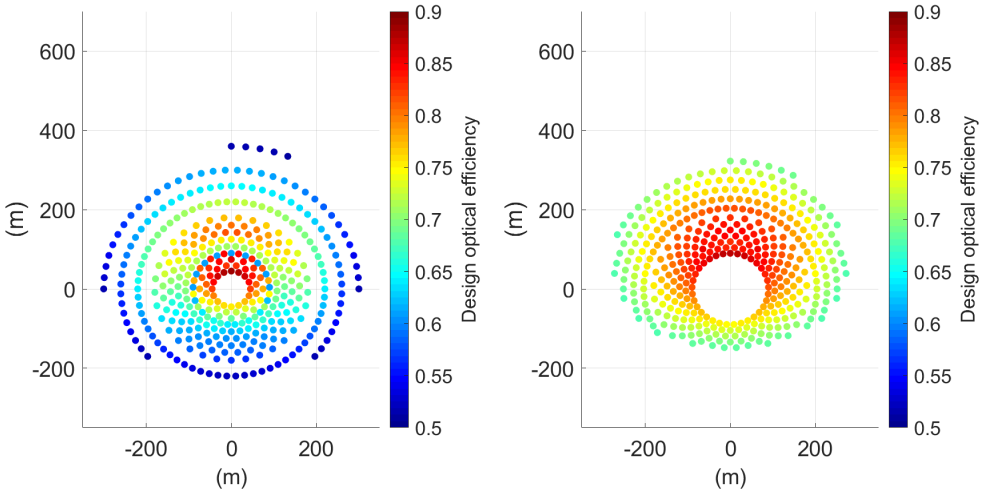

(c) $H_t = 60m$, *external receiver*

(d) $H_t = 120m$, *external receiver*

Figure 3.7: *Layout comparison of the best economic and technical solution for the cavity (a and b) and the external (c and d) receivers.*

Finally, the seasonal behavior of the daily efficiency of the presented layouts is analyzed for three reference days: the 21^{st} of March, June and December (Fig. 3.8). The polar and surrounding fields shows distinct daily and seasonal performance: first of all, the bell-shaped trend of the optical efficiency resulting from the cavity geometry is opposed to a more constant development with the external receiver (especially when the tower is low Fig. 3.8c). Moreover, the cavity receiver penalizes the optical efficiency when the solar altitude is higher and consequently the peak is observed for December and a penalty drop of more than 5 point percentage occurs in June (corresponding to the maximum Zenith angle). On the contrary the surround field benefit by high solar altitude and the seasonal behavior is more uniform, indeed the maximum efficiency in December is reduced by only 3.2 point in the worst case.

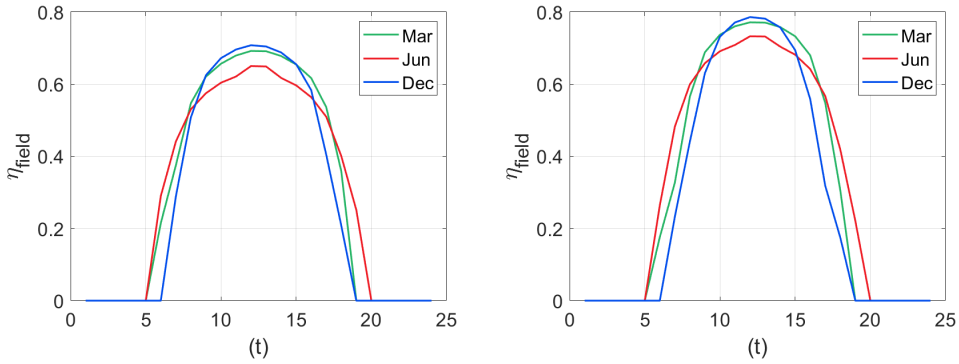

(a) $H_t = 60m$, *cavity receiver*

(b) $H_t = 150m$, *cavity receiver*

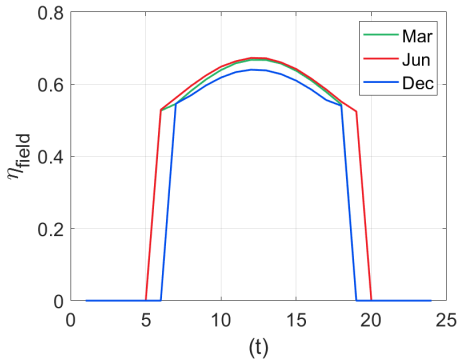

(c) $H_t = 60m$, *external receiver*

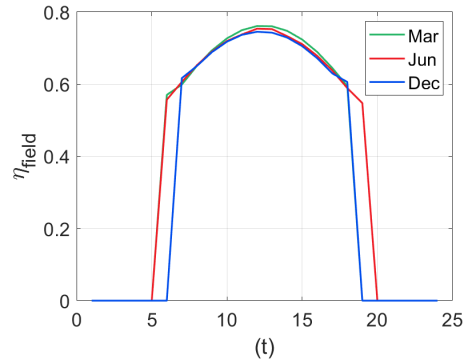

(d) $H_t = 120m$, *external receiver*

Figure 3.8: *Daily and seasonal trend of the optical efficiency of the optimal layouts.*

Part II

Multi-generation system optimization

CHAPTER 4

Concentrated solar power system

4.1 Introduction

A growing market share of renewable energy is ongoing in several countries and is expected to increase further in the next years. When the renewable penetration increase, the plants which can satisfy the energy deficit, related to the variability of the renewable sources, assumes a key role in the replacement of fossil-fired solution [123]. The role of the solar power plants is no longer limited to a marginal contribution, and a high dispatchability is becoming a requirement as important as a low price. Furthermore, particular climate conditions, such as of MENA region with a direct normal irradiance (DNI) level between 2000-3200 kWh/m^2 per year [100], the competitiveness of solar technologies is further enhanced.

The main disadvantages of solar energy are the significant land requirement to harness enough power and, in addition, the regulation of solar power plants is particularly delicate considering the stability of the grid [124]. The two available solar technologies are photovoltaic panels (PV) and concentrated solar power (CSP): PV generates electricity exploiting the photoelectric effect of the materials, whilst CSP collects the solar thermal power and produce electricity with a thermodynamic cycle. The performance of the two technologies has been extensively compared: in the study carried out by Desideri et al., the PV production is greater when the same nominal power or the same land oc-

cupied is imposed to both plants [125]. Roni et al. confirm that PV is more convenient thanks to a significant lower land requirement [126] and Servert et al. highlighted that the PV better modularity results in more attractive investment [127]. On the other hand, Magrassi et al. underline that the CSP main advantage is the capability to schedule the production (across peak demand time period), and the possibility of hybridization with fossil fuel increase the energy reliability [7]. Furthermore, CSP is the most convenient solution for the integration with desalination plants, decisive given the scarcity of the drinkable water of the MENA region [128]. Finally, Mahlooji et al. study the affordability of the solar technologies in the GCC countries based on their impact on other resources such as water, land and economy with the Relative Aggregated Footprint (RAF). Although the CSP has a great impact, especially for water footprint, the initial commercialization level of the CSP industry shows considerable cost reduction margins [129].

The availability of an embedded long-term storage system allows supplying thermal energy when the radiation is low (or fluctuating) and can extend (or shift) the operation of the plant after sunset, allows to significantly reduce the CO_2 emissions ensuring the variable hourly demand, as reported by Guédez et al. in [130]. The predominant TES system for CSP plants is a two-tank molten salt configuration introduced and proven in long-term operation [131, 132]. Among the CSP technology available for electricity production, parabolic trough collectors (PTCs) central receiver systems (CRS) are the competitors for utility-scale applications. Nowadays PTCs dominate the installed CSP capacity, though a recent growth in CRS deployment has been seen, mainly driven by the ability to achieve higher temperatures [133], raising plant efficiencies and providing lower storage costs. Furthermore, CRS typically have a more uniform thermal collection capability, all over the year. However, because of the larger spacing needed by the heliostats, the energy density is lower than for the PTC plants and the financial risk is still high,as reported by Ogunmodimu and Okoroigwe [134] .

The possibility of satisfying the power demand continuously has led the enhancement of CSP plants for standalone grid applications [135] where the system performance prediction and the hourly behavior must be analyzed in details to guarantee the production. PTC and CRS are compared in different operative conditions; studies like [136] show the prevalence of PTC in the field of ISCC (integrated solar combined cycle) whilst the CRS shows better performance when coupled with a steam Rankine cycle [137]. Ravelli et al. [10] investigates the capability to satisfy the demand for power and cooling in Saudi Arabia; the required aperture area for CRS is lower than PTC thanks to a flatter energy demand. The electric load pattern represents an important issue in terms of plant operation forecasting [138] the load-following strategy requires a thermal energy storage sized up depending on the operational scheme, as

pointed out by Wagner [139]. The load patterns could differ for variation between daily maximum and minimum and for seasonal fluctuations (summer vs. winter). The patterns of networks with high concentration of residential buildings [140] typically exhibit large daily and seasonal variations, whilst the load curve of industrial district [141] are usually flat. In the case of large penetration of non programmable renewables without storage, the back up generation system (fossil or renewable) must satisfy an energy demand with a typical duck profile characterized by a minimum requirement in central hours and a very steep ramp in the sunset hours [142].

The present work aims to investigate the load-following capability of a full solar plant assumed to operate in a remote or weakly interconnected grid, and to completely match the electricity demand of a mid-size community. Starting from previous works focused on the integration of solarized power plants and electric grids [143] and on the design of CSP plants [10], the present section aims to investigate the load-following capability of a full-solar power plant. The power systems are assumed to operate in a remote or weakly interconnected grid, and to almost completely match (SF = 90%) the electricity demand of a mid-size community. The power block is based on a typical steam Rankine cycle with superheated steam temperature $540°C$, coupled with a molten salt mixture direct storage system. Two different solar devices are compared: PTCs with north-south axis orientation and CRS with a field of heliostats reflecting on the tower top. Different operative conditions are considered in order to evaluate the production flexibility of the solutions.

4.2 Design condition and assumption

Two typical electric loads, namely industrial and residential, presented in [144, 145] and representing two city districts with different settlements, have been considered to estimate pros and cons of the two different CSP plant configurations. The two patterns of power demand were scaled up to reach the same peak load (100 MW), and it follows a different annual integral values (540 GWh vs. 700 GWh). Figure 4.1 shows the electric load trends in a typical summer and winter day. The residential load exhibits a large daily variation in the power demand (the minimum is about 50% of the peak), and simultaneously a moderate reduction between summer and winter peak value (100 MW vs. 50.3 MW): in this case, the load curve is strongly affected by the building air conditioning. The industrial load patterns, on the contrary, show a very limited seasonal variation (between 15%) and a lower distance between maximum (100 MW) and minimum (69.8 MW).

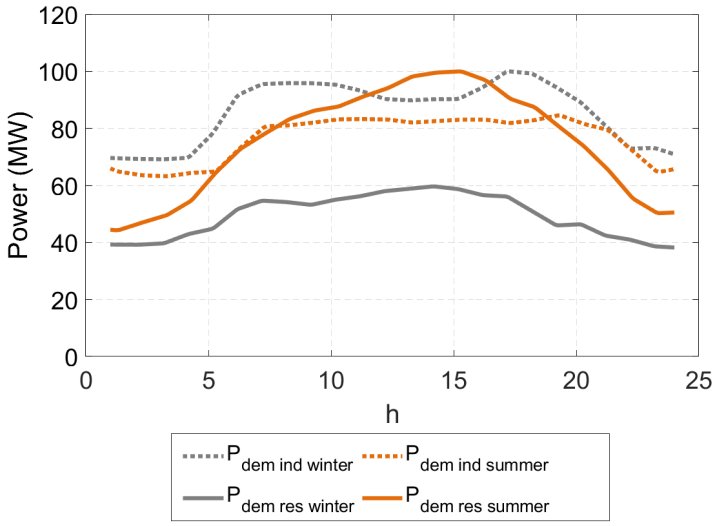

Figure 4.1: *Seasonal variation of the electric power demand for two different load pattern.*

4.2.1 Plant model

The models developed for the CSP system simulation and the performance of the solar technologies are based on Trnsys® v. 18 and plant operation are simulated over one-year period.

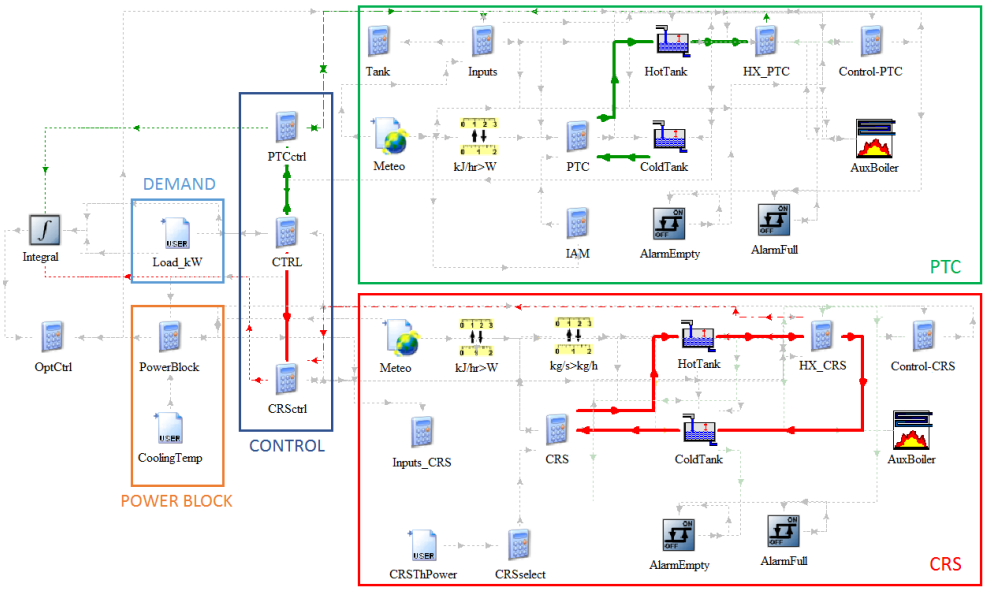

Figure 4.2: *Trnsys deck of the CSP plants.*

The deck of the CSP plant is shown in figure 4.2; in addition to the so-

lar technologies model, some components are included to manage the energy dispatching, depending on the hourly demand and the power block efficiency. In this work, the solar field (PTC or CRS) are considered one by one and no interaction is expected.

Each CSP plant includes the solar field and a two-tank Thermal Energy Storage system. The heated molten salt mixture (60% $NaNO_3$-40% KNO_3) is stored in the hot tank and delivered to the steam generator according to the mass flow rate required by the power block. After the heat transfer, the molten salt flow rate is collected in the cold tank.

The solar field design temperature is 550°C and the TES working levels are respectively 550°C and 300°C. The CSP model use the storage to limit the source fluctuation and store the excess of the molten salt production.

A Steam Rankine Cycle driven by molten salt convert the heat collected by the solar field into electric energy delivered to the load. The present work focuses on the solar field operation, including the Thermal Energy Storage and a less detailed performance evaluation of the power block section is considered acceptable. However, the efficiency of the power block affects the real discharging time of the Thermal Energy Storage and a correct prediction of the TES operative time. The model of the steam turbine is based on the review study provided by Poullikkas et al. [99] where the main specification of the power block coupled with CSP plants are reported. In table 4.1, main assumption and specification for the adopted model are shown. The steam turbine performance is evaluated only in terms of efficiency variation due to the design capacity, part load and ambient temperature effect; any more detailed analysis of the turbine operation has been omitted in this essay.

Table 4.1: *Steam Rankine cycle specifications (from [99]).*

Turbine type	Condensing, back pressure and extraction turbine
Cycle design efficiency	Fig. 4.3a
Turbine inlet temperature	$540°C$
Turbine inlet pressure	40-140 bar (variable with capacity)
Steam mass flow rate at turbine inlet	2-108 kg/s (variable with capacity)
Exhaust condition	50 mbar, X = 0.85
Extraction pressure	5.83 bar
Off-design efficiency	Fig. 4.3b

Considering the expected power block capacity, in the range between 50 and 100 MW, the adoption of an interpolation of the literature results represent an adequate solution. The interpolation function (Figure 4.3a), based on a polynomial function (dashed line), fit the curve proposed by Poullikkas (solid line), in the interval 500 kWe – 100 MWe, with a coefficient of determination R of 0.99. The operation map, reported in Figure 4.3b, includes the part load

derating and the ambient temperature for the performance of the condenser. The map is then normalized to a reference condition of 100% load and 30 °C condenser temperature. Starting from a selected design capacity of the plant (proposed by the optimization tool), the software combines the two maps and evaluate the performance based on the steam turbine size and operative conditions. Lastly, the developed algorithm, according to the hourly efficiency of the power block, evaluate the molten salt mass flow rate that the thermal storage must provide to satisfy the hourly demand.

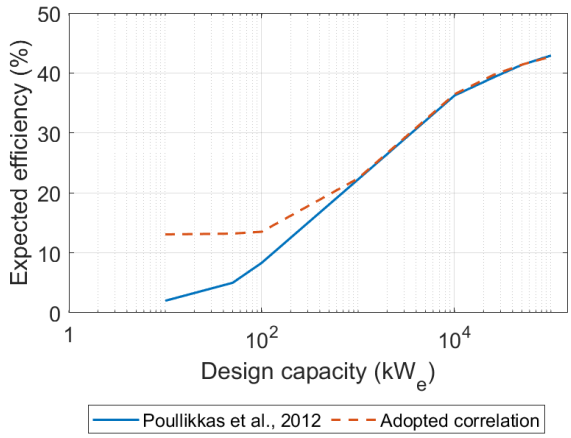

(a) *Power block design efficiency vs. power block design output*

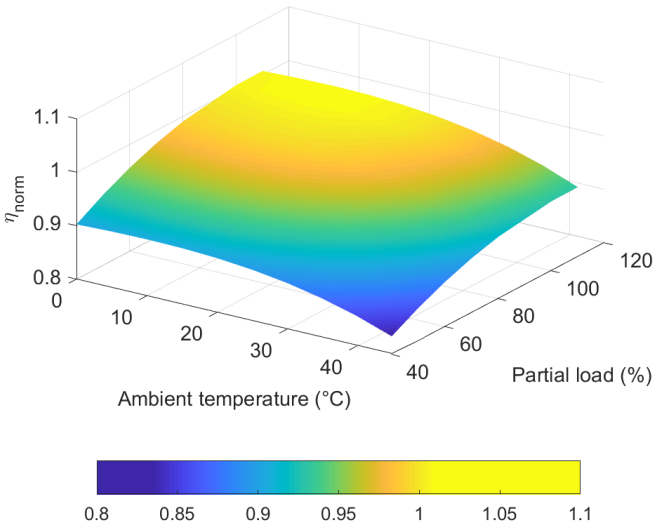

(b) *Power block performance map (normalized 100% Load – 30* deg *C)*

Figure 4.3: *Thermal efficiency variation of the power block with the turbine size (a) and with variable operative condition (b): ambient temperature and partial load.*

4.3 Methods and tools

The thesis section aims to investigate the load-following capability of different CSP plant configurations to satisfy the load demand of a mid-size town located in Egypt. Ambient condition in Egypt permit to solar technologies to be more competitive: the direct normal irradiance (DNI) reaches levels between 2000-3200 kWh/m^2 per year and an average of 9-11 hours of sun activity [100].

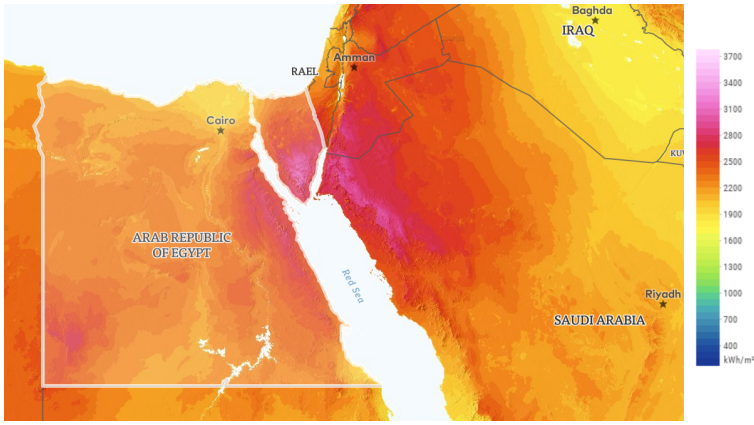

Figure 4.4: *Annual beam radiation on Egyptian territory.*

Two locations are in particular compared: Aswan and Giza, with quite different meteorological conditions as depicted in Figure 4.5, for the two representative summer and winter days.

The Figure 4.5a shows the monthly average temperature and humidity compared for the two cities. Aswan shows a remarkable excursion between maximum and minimum temperature whilst, the humidity is very low both in summer and winter period. This leads to a reduced diffusion of the available solar radiation and, consequently, the concentrated solar devices to operate with a better efficiency. Giza, conversely, presents a reduced peak temperature in summer, that benefits the steam turbine efficiency, but a much greater humidity level (around 60%) penalize the available radiation. From Meteonorm database, the annual amount of DNI is 3058 kWh/m^2 and 2097 kWh/m^2, for Aswan and Giza respectively.

Moreover, the proposed location exhibit a contrasting seasonal trend of the DNI, as presented in Fig. 4.5b. Giza show a typical bell-shaped profile with a peak radiation in summer and an high reduction (50%) during the winter period. On the contrary, the radiation of Aswan has a more constant behavior, reaching the maximum level in winter (250 kWh/m^2).

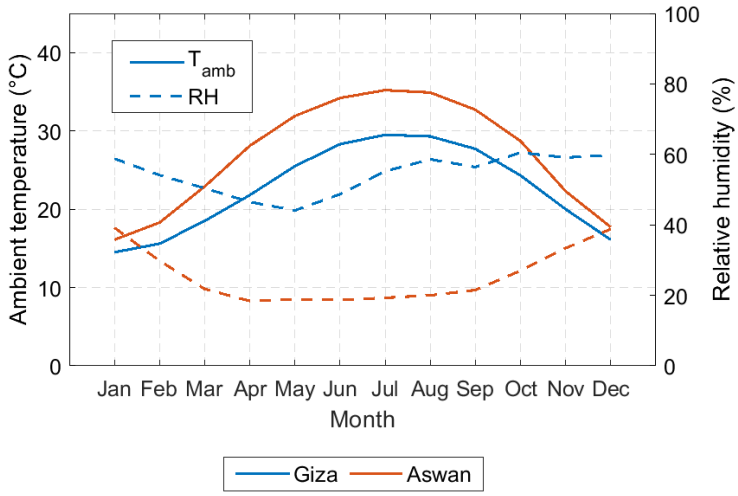

(a) *Ambient temperature and Relative humidity(%)*

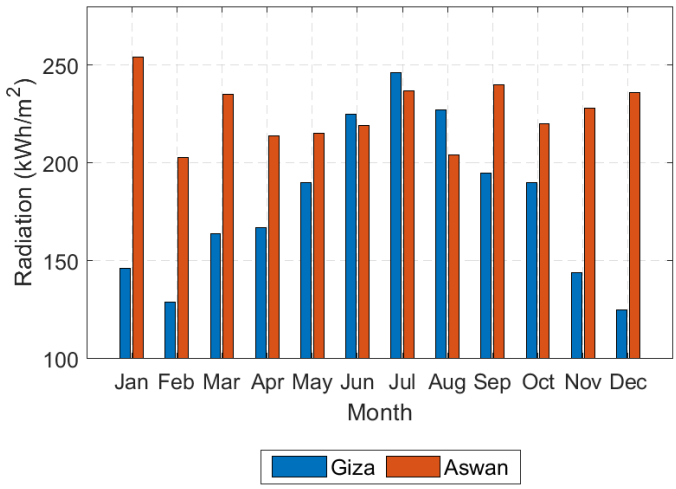

(b) *Direct normal irradiance*

Figure 4.5: *Ambient condition comparison for the investigated location, Giza and Aswan.*

The simulations were carried out for a one-year period on hourly basis. With regard to the computer model, firstly it has to be underlined that in every modeling activity the selection of the level of investigation is a crucial point. The present chapter targeted a compromise between a detailed analysis and an evaluation of the performance of the CSP technology.

4.3.1 Solar fields model

The solar field based on PTC is supposed divided in several loops with north-south orientation. Each single collector is 100 m length and 6 m wide (the aperture area is 524.8 m^2) and the loop is made by a series of 8 arrays. The PTC efficiency was evaluated, time step by time step, according to the Eq. 4.1 proposed by Lippke in [146]. The adopted equation includes long wave emission linked to the effective sky temperature and the wind speed to estimate the thermal losses. The coefficients η_{opt}, A, B and C were computed to fit the thermal efficiency curve of Schott PTR70 receivers under standard conditions [147]. The incident angle modifier K is related to the effect of the non-perpendicularity of solar radiation and it is a function of the sun-ray incidence angle.

$$\eta_{PTC} = \eta_{opt} \cdot K - (A + C \cdot V_{wind}) \cdot \frac{T_{av} - T_{amb}}{I_b} - \varepsilon \cdot B \cdot \frac{T_{av}^4 - T_{sky}^4}{I_b} \quad (4.1)$$

Moving to the CRS, the heliostat field is made-up by thousands of mirrors (178 m^2 reflective surface) having a surrounding arrangement and pointing to an external receiver. During this thesis work, the efficiency of the heliostat field and, more in general, of the entire collector system is analyzed in detail. The CRS performance is not easily extendable for different scale since the contribute of each component is variable with the design power (such as the number of heliostat, the layout arrangement, the tower height and the receiver dimensions). For this reason, a preliminary optimization has been carried out determining the heliostat field-receiver structure that minimize the cost for a range of the most probable design thermal power (from 300 MW_{th} to 1000 MW_{th}).

Heliostat field-tower economic optimization

The economic optimization procedure is schematized in Fig. 4.6, repeated for all the power considered. The performance model and the cost correlation adopted are reported in the chapter 1.

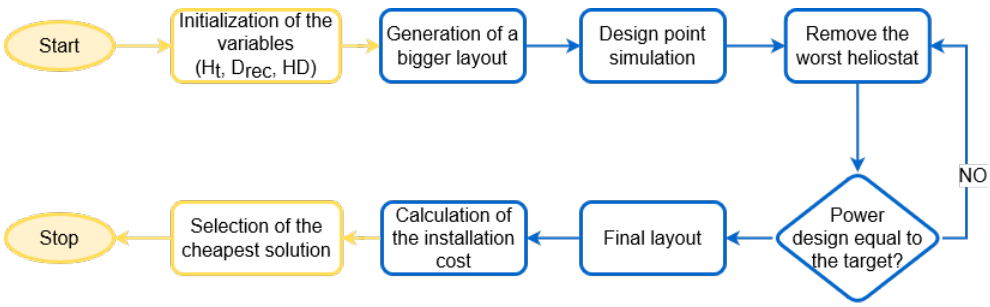

Figure 4.6: *Optimal parameters value for different nominal power.*

- For the selected set of variables (namely H_t, D_{rec}, HD_{rec}), a bigger heliostat field is generated based on the geometrical parameters optimized for the size (i.e. the number of heliostat) and the tower height (obtained with a procedure like in chapter 2).
- The worst heliostats are deleted until the power delivered to the receiver is equal to the target power.
- For each combination the installation cost is calculated (for the economic model and detailed values, please refers to par. 1.5).
- The solution that minimize the cost for each power considered is selected.

The analyzed variables and their range of variation is reported in table 4.2. The aiming strategy is assumed to be constant and equal to 2, ensuring a more uniform distribution of the heat flux over the receiver surface for the most of operative period.

Table 4.2: *Definition of the search space of the economic optimization.*

Variable	Unit	Range	Step
Ht	(m)	150-270	10
D_{rec}	(m)	11-20	0.5
HD_{rec}	-	1-1.2	0.1

The resulting configurations are summarized in fig. 4.7 where the design efficiency and the total installation cost are also reported. The number of selected heliostat is directly proportional to the power required, also as the receiver absorber area; whilst, the optimal tower height remains constant for ranges of 100 - 150 MW_{th}. The behavior of the occupied land is consistent with the changes in tower height, that confirms the strong influence of the Ht on the layout arrangement. For further details about the optimized CRS fields please refer to the appendix A.

The trend of the efficiencies is in accordance with changing in tower height (the greatest discontinuities are highlighted for 500 MW_{th} and 850 MW_{th}), mostly, and an influence of the receiver area is also depicted (especially around 700 MW_{th} and over 900 MW_{th}). Finally, a nearly linear trend of the total capital cost with the power is observed, while the cost per unit of reflective area is slightly lower when the power considered is higher: the cost of tower and receiver are less impact when the number of heliostat in the field is greater.

Despite many codes and algorithms are devoted to the detailed calculation of the optical losses, including cosine effect, blocking and shading, mirror reflectivity, spillage and atmospheric attenuation [58, 148], the principal parameters affecting the hourly field efficiency are the size plant, namely the aperture

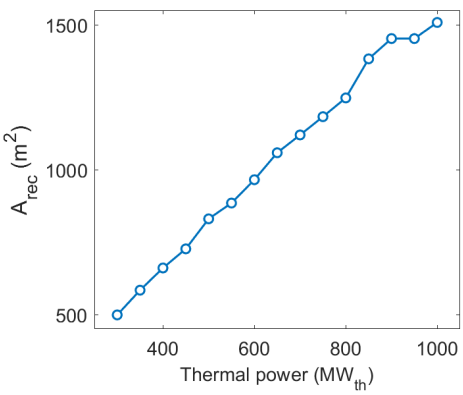

(a) *Receiver area*

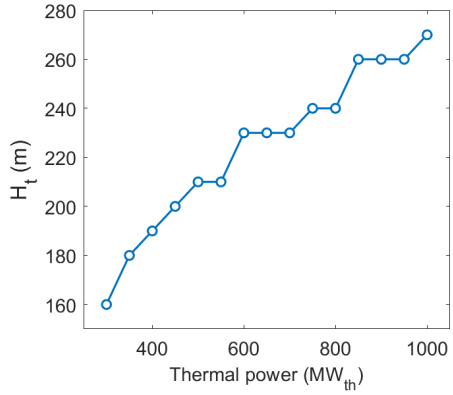

(b) *Tower height*

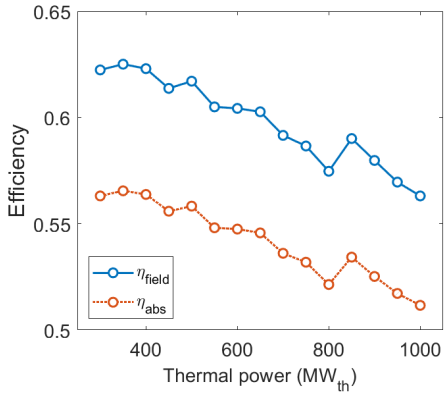

(c) *Number of heliostats*

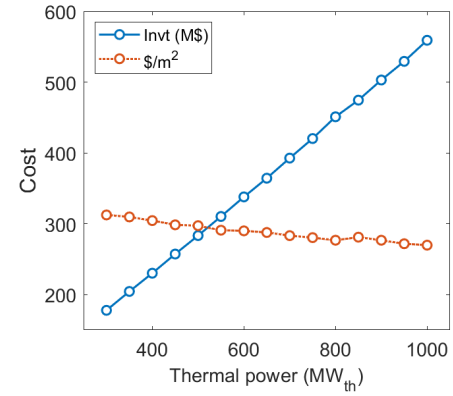

(d) *Land occupied*

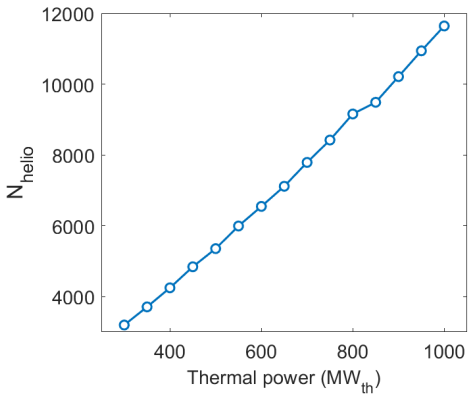

(e) *Design efficiency*

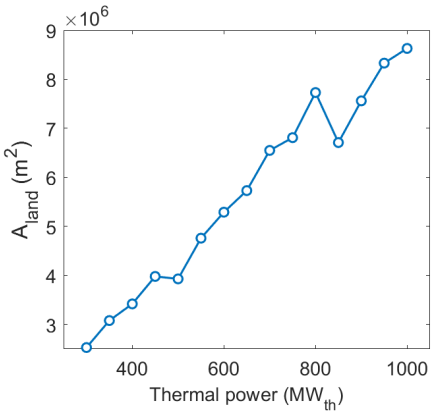

(f) *Capital cost*

Figure 4.7: *Optimal parameters value for different nominal power.*

area of the mirrors and the tower height, and the zenith angle. From this chapter and on, the performance of the heliostat sub-system included in the system model was simplified to an efficiency map, reducing the computational cost but ensuring a good accuracy. For each size and for each combination of solar position the field efficiency has been calculated according to eq. 1.12. The resulting map is shown graphically in Fig. 4.8. Moreover, the seasonal peak efficiency variation is reported in Fig. 4.9: a general flat trend is observed from March to September with a limited reduction (less than 0.4%) in central months (this behavior has already been commented in the subsection 2.3.2). The main irregularities are correspondent to the trend show in Fig. 4.7e.

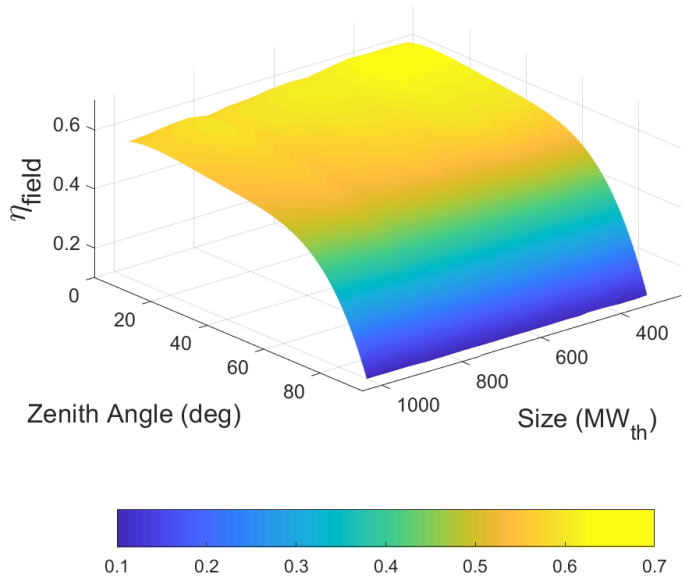

Figure 4.8: *Heliostat field efficiency map as function of size and Zenith angle.*

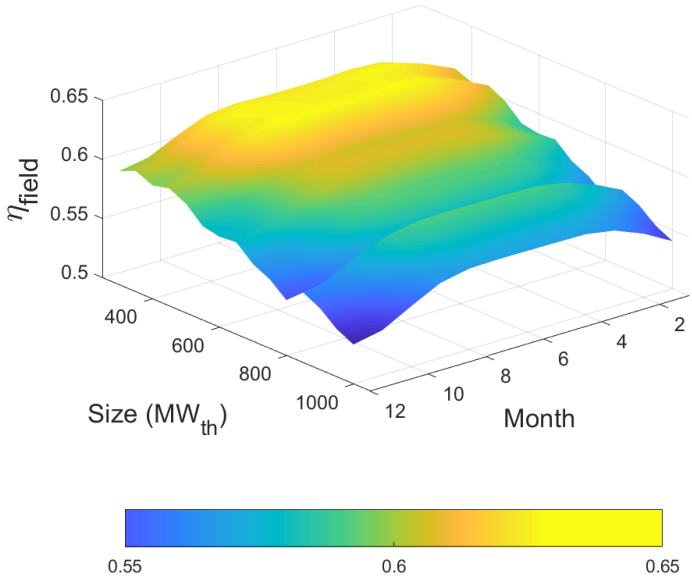

Figure 4.9: *Monthly variation of the peak efficiency for different power.*

4.4 Economic evaluation and system optimization

For each plant configuration, the solar field aperture area $A_{solarfield}$, the storage capacity Cap_{tank} and the turbine nominal power P_{PB} have been determined through an optimization procedure. The size of the solar field and of the turbine are chosen independently in order to enable the optimizer to determine the best combination between Solar Multiple (SM) and storage capacity. The optimization tool GenOpt, according to the scheme proposed in App. B, is used to determine the best component size that minimize the budget cost function (Eq. 4.2) ensuring a Solar Fraction[1] (SF) of 90%. The optimization algorithm implemented is based on a direct search pattern method that runs multiple Trnsys simulations changing the search pattern of the variables, with the aim of fulfill hour by hour the power demand with the minimum investment cost. The considered unit costs shown in Table 4.3 have been estimated according to the economic data reported by the NREL in the System Advisor Model (Version 2018.11.11) [85]. The objective function, corresponded to the direct capital cost of the plant (C), is calculated according to Eq. 4.2 and includes: the solar field (troughs for the PTC case; heliostats, tower and receiver for the CRS case), the tank system C_{tank} and the power block C_{PB}. The tank capacity Cap_{tank} (Eq. 4.3)is calculated as the maximum available hours of turbine operation h_{tank} at its nominal capacity P_{PB}. The software SAM listed the molten

[1]The Solar Fraction represent the portion of energy demand supplied by the solar technology.

salt TES and the steam turbine costs equal to 22 $/kWh and 1440 $/kW, respectively. The proposed model includes a variable budged cost according to the nominal capacity of the power block. In particular, Poullikkas and al. [99] propose an unit cost function ($/kW). The reported power block cost correlation has been modified in order to align the installed cost with the value reported by SAM at the same nominal capacity of 100 MW. The parameter p is a penalty-cost related to the energy deficit (seen as $SF - SF_{target}$), that gives different "cost" to energy deficit or surplus (Eq. 4.4); this functional structure allows to reject all system configurations that cannot satisfy the power request and avoid an excessive oversizing of the system.

Table 4.3: *Budget cost of CSP component.*

	unit	Value
C_{PTC}	$(\$/m^2)$	220
C_{CRS}	$(\$/m^2)$	$324 - 2.74 \cdot 10^{-5} \cdot A_{CRS}$
C_{tank}	$(\$/kWh)$	22
C_{PB}	$(\$/MW_e)$	$15587 \cdot P_{PB}^{-0.232}$

$$C = A_{solarfield} \cdot C_{solarfield} + Cap_{tank} \cdot C_{tank} + C_{PB} \cdot P_{PB} + p \tag{4.2}$$

$$Cap_{tank} = h_{tank} \cdot P_{PB} \tag{4.3}$$

$$p = \begin{cases} 3.6 - 4 \cdot SF & SF \leq SF_{target} \\ 1.5 \cdot SF - 1.35 & SF > SF_{target} \end{cases} \tag{4.4}$$

The combination of reflective area, hours of full tank and turbine nominal power that are analyzed in the optimization procedure are included in the search space reported in Tab. 4.4. It is worth noting that, based on the result of the economic analysis of the tower system, it is found an one-to-one correspondence between nominal thermal power and reflective area of the field.

Table 4.4: *Optimization variables search space.*

Variable	Unit	Start value	Min value	Max value	Step
Solar field ($A_{solarfield}$)	km^2	0.86	0.5	4.2	0.1
Hours full tank of storage (h_{tank})	h	12	6	24	1
Nominal power (P_{PB})	MW	75	20	150	2.5

Finally, to correctly compare the economic performance of different technologies the LCOE function is considered, for easier reading the equation 1.42

is called back below. The adopted financial parameters for the two technologies, based on [85], are resumed in Tab. 4.5.

$$LCOE(¢USD/kWh_e) = \frac{\frac{i(1+i)^{N_y}}{(1+i)^{N_y}-1}C_{plant} + OM_f}{E_{El}} + OM_v$$

Table 4.5: *Financial parameters.*

Parameter	PTC	CRS
Lifetime (Ny)	30	
Interest rate (i)	4	
Contingency	7%	
Sales	4%	
EPC	11%	13%
OM_f ($\$/kW-yr$)	66	
OM_v ($\$/MWh$)	4	3.5

4.5 Results

The results of the optimization procedure are summarized in Table 4.6, the load following capability is investigated for each CSP technology for two load profile pattern (i.e. residential and industrial) and the influence of the climate condition is also considered (the analysis is repeated for Giza and Aswan).

First the configurations designed for the residential case are investigated. The ambient conditions of Giza heavily penalizes the performance of PTC that requires +46.5% of reflective area to satisfy the demand level of 90%. In Aswan, the heliostat field is only 6.2% smaller but the CRS plant is also favored by a tank capacity lower by 38.5%. The power block size seems to be independent from the location that suggest a different load-following strategy between the two technology: the PTC steam turbine capacity greater by 25-30% indicate that is forced to work in more severe condition (near the maximum peak) to guarantee the annual energy demand. The residential load, under Aswan condition, allows to not excessively oversize the solar field and a solar multiple of 2.4 is achieved (near to the best practice suggestion); on the contrary, for Giza the SM is much greater especially for the PTC, over 6.3.

Moving to the industrial load case, almost the same behavior is observed for the solar field that is larger for the PTC of 51% and 21%, for Giza and Aswan respectively. Moreover, the tank capacity of PTC plant is kept constant between the two location whilst a significant difference is observed: for Giza, a capacity greater by 61% is required (30% more than PTC), whilst for Aswan, the tank is smaller by 20%. Similarly to the residential case, the steam turbine is more influenced by the efficiency of the field but the different between the two technologies is reduced to only 10 MW_e.

The capacity of the TES system and the solar aperture area are, in general, larger in the industrial case for both PTC and CRS: this is related to the need to satisfy an higher demand also during night-time period.

With regard to the global cost, the CRS appears more cost effective for all cases except for residential case at Aswan where the reduction of PTC efficiency is compensate by a reduced demand and a higher radiation. More in detail, for Giza the solar field is responsible for more than 60-65% of the global cost; under Aswan meteorological condition, the field impact is reduced to 50-55% and the power block effect becomes more remarkable (up to 17%).

Table 4.6: *Optimized component size for each combination.*

		Giza		Aswan	
		PTC	CRS	PTC	CRS
Residential					
A_{refl}	(m^2)	2593500	1386442	918750	861876
Cap_{tank}	(MWh)	1045	1141	1039	683
PB_{size}	(MW_e)	95	63.5	87.5	65
SM	(-)	6.3	3.9	2.4	2.4
$Capital\ cost$	$(\$M)$	894.6	650.5	414.2	441.1
Industrial					
A_{refl}	(m^2)	3819375	1947320	1362638	1066754
Cap_{tank}	(MWh)	1186	1564	1186	968
PB_{size}	(MW_e)	89.5	82	89.5	80
SM	(-)	9.9	4.05	3.5	2.6
$Capital\ cost$	$(\$M)$	1320	860.8	550.9	539.1

Moving to the simulations, firstly the daily simulation results related to two representative summer and winter days are presented. Then, the monthly and annual simulation outputs will be shown and discussed.

4.5.1 Daily simulation results

Figure 4.10 shows the solar-to-thermal efficiency of the solar fields with reference to the Aswan residential case (where the aperture area is similar for the two technologies).

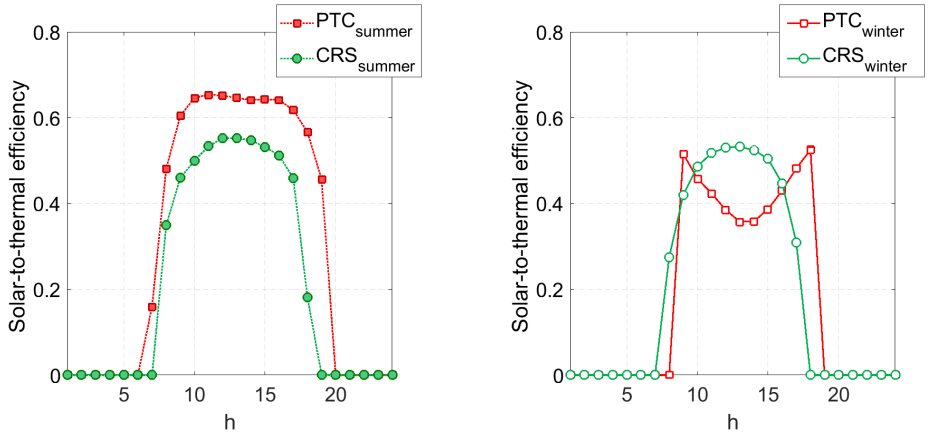

(a) *Summer* **(b)** *Winter*

Figure 4.10: *Solar-to-thermal efficiency in a typical summer and winter day.*

It is clear that PTC and CRS perform differently. PTC efficiency dramatically decays in winter days because of the cosine effect and lower ambient temperatures. The solar field efficiency for CRS configuration is slightly lower in summer (55.2% vs. 64.6% in the central hours of the day), but significantly higher in winter (53.2% vs. 35.7%). This is due to the benefits of the 2-axis tracking system.

Figures 4.11 and 4.12 shows the hourly results for each plant configuration and load pattern. Plots report the collected heat (Q_{coll}) and the instantaneous heat demand required by the power block (Q_{dem}), for a representative summer (full symbols) and winter day (hollow symbols). The hot storage tank level is also reported. It is worth noting a better exploiting of the storage in summer periods and a significant defocus is observed for PTC technology (when the tank reaches the maximum capacity); on the contrary, in winter the TES level does not exceed 40%, with only few exceptions (e.g. the industrial cases in Aswan). The condition of Aswan ensure a more uniform performance of the CRS system throughout the year ensuring a better capability (complete charge and discharge cycles). In the residential load case (Fig. 4.11), the solar radiation profile and the power demand pattern seem to be in-phase; however, the PTC solar field appears over-sized in summer, especially for Giza where the peak value of the collected heat is 750 MW, whilst the maximum heat demand is 200 MW. The bell-shaped profile of the power demand does not fit much the flat CRS efficiency curve. This attenuates the performance difference between CRS and PTCs. Moving to the industrial load case (Fig. 4.12), the PTC over-sizing is emphasized (peak production 1600 MW vs. peak demand 203 MW) due to the low performance in winter, when the PTC efficiency almost halves but the demand is higher. Therefore, for many hours per day a fraction of the troughs must be defocussed, since the hot storage tank is at the maximum capacity. On the contrary, the CRS plant configuration exhibits similar performance in summer and winter, as documented by the efficiency curves reported in Figure 4. The CRS configurations appear more advantageous less evident in the residential case. The lower aperture area and the more constant efficiency pattern allows minimizing the heliostat defocussing, as confirmed by the limited number of hour with full hot tank.

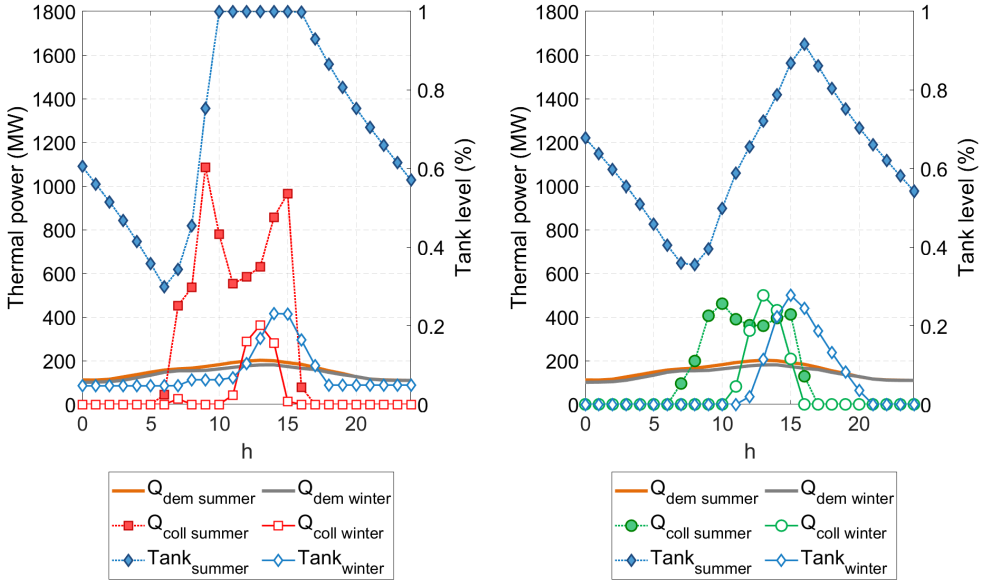

(a) *PTC Giza Residential*

(b) *CRS Giza Residential*

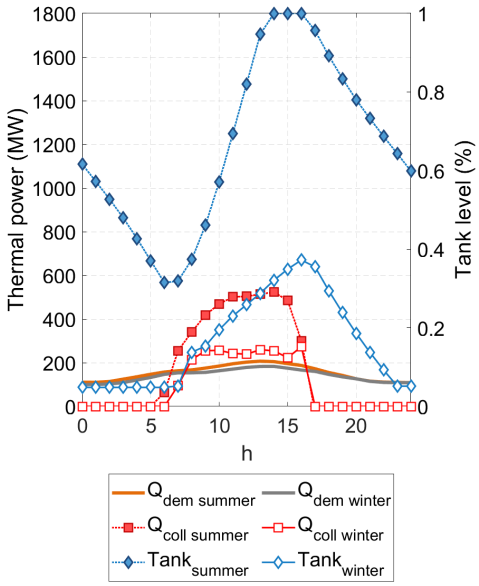

(c) *PTC Aswan Residential*

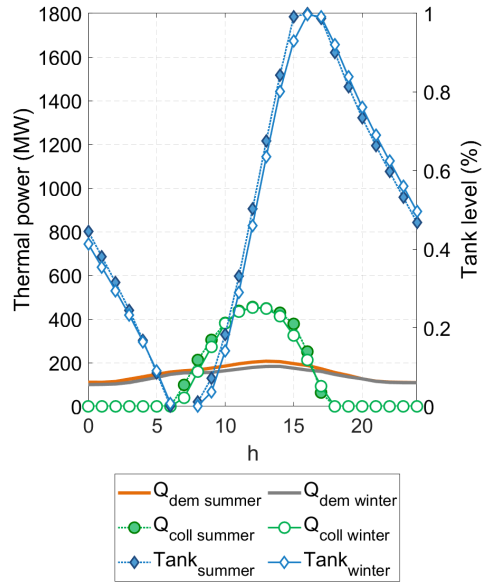

(d) *CRS Aswan Residential*

Figure 4.11: *Solar field daily simulation (Residential case).*

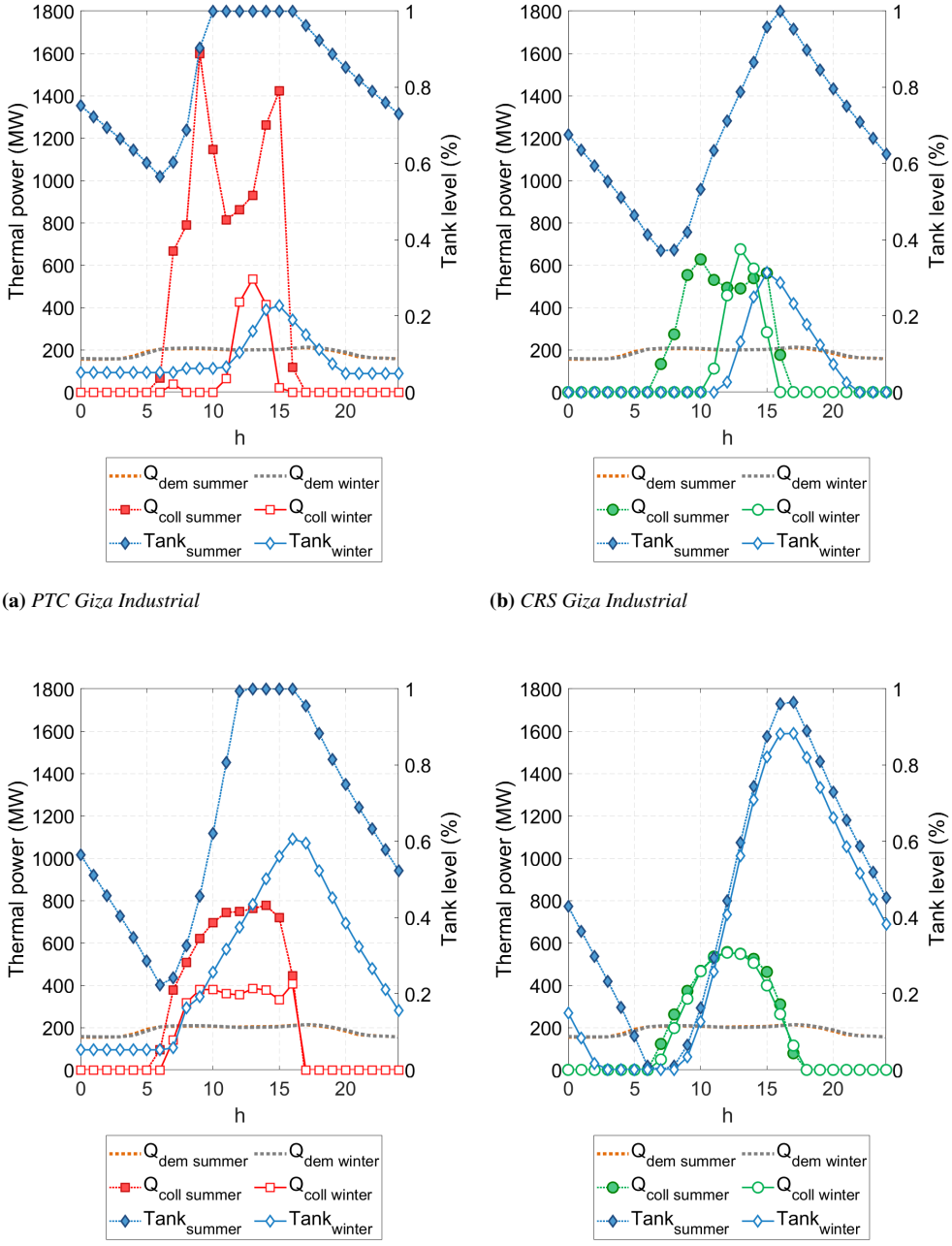

(a) *PTC Giza Industrial*

(b) *CRS Giza Industrial*

(c) *PTC Aswan Industrial*

(d) *CRS Aswan Industrial*

Figure 4.12: *Solar field daily simulation (Industrial case).*

4.5.2 Monthly and yearly performance

Figures 4.13-4.16 show the monthly energy amounts, namely the available solar energy (E_{rad}), the collected heat (E_{coll}) and the power block thermal input demand (E_{dem}), for the two load profiles and the locations considered.

A different behavior can be noticed depending on the solar field. Looking at the PTC performance, it is clearly seen that in summer the heat collection strongly exceeds the heat demand from March to October: a maximum surplus of 312% is observed for the industrial case in Giza that is slightly reduced to 218% moving to the residential demand; under Aswan condition, the heat excess is limited to 84% and 40%,respectively for the two load. In winter, the energy collected daytime is just enough to drive the power block and the limited energy surplus is sent to the storage. For these reasons, the design requires to oversize the aperture area and many troughs in summer must be defocussed. The CRS monthly thermal production is fairly stable throughout the year and slightly larger than the heat energy demand: the energy surplus is never greater than 54.7% and 9%, for Giza and Aswan respectively.

More in general, the industrial case causes a greater thermal dumping in summer months since the peak of demand occurs when the field performance is at minimum. This effect is accentuated for Giza condition since the bell-shaped trend of the radiation intensity. Furthermore, a different management of the admitted energy deficit (10% of the demand) is observed. A peak takes generally place in December, but for CRS the deficit is more distributed throughout the year, except in central months.

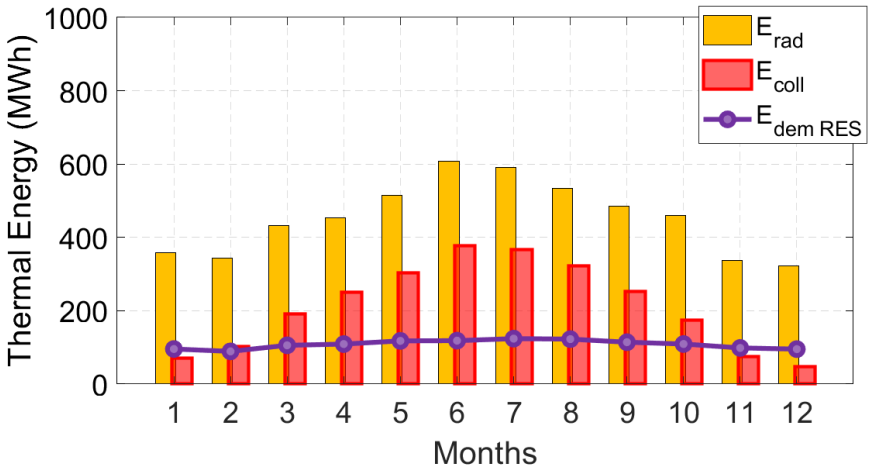

(a) *Residential*

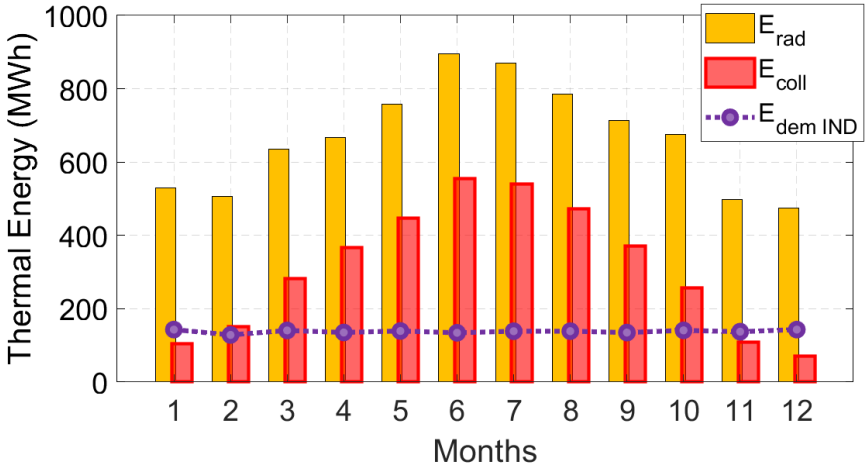

(b) *Industrial*

Figure 4.13: *Monthly simulation results for PTC at Giza condition.*

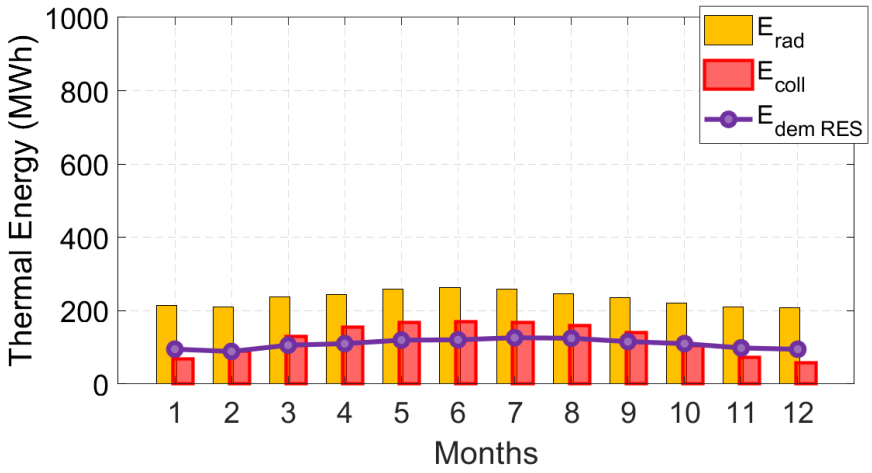

(a) *Residential*

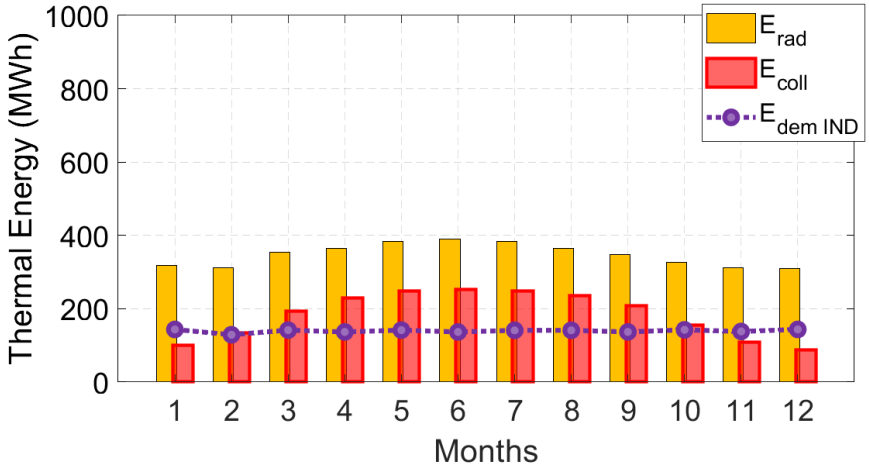

(b) *Industrial*

Figure 4.14: *Monthly simulation results for PTC at Aswan condition.*

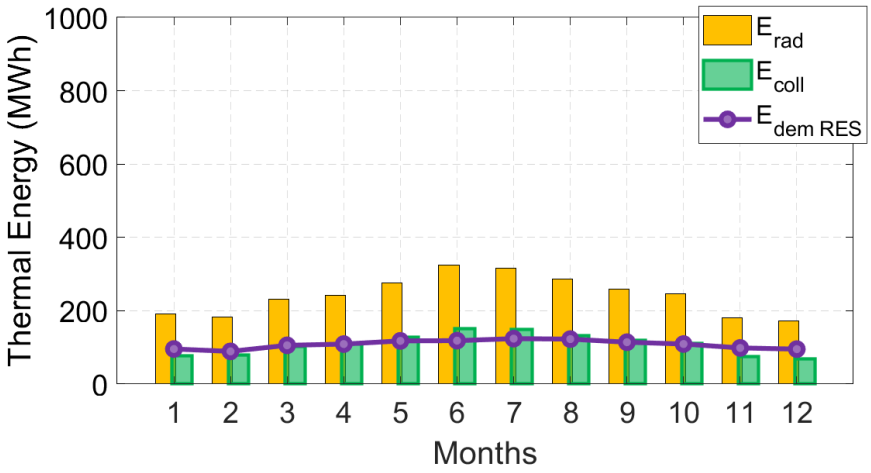

(a) *Residential*

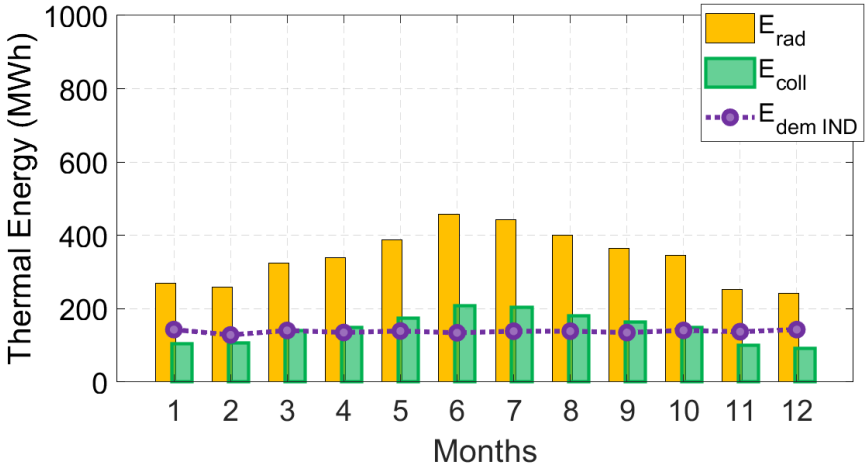

(b) *Industrial*

Figure 4.15: *Monthly simulation results for CRS at Giza condition.*

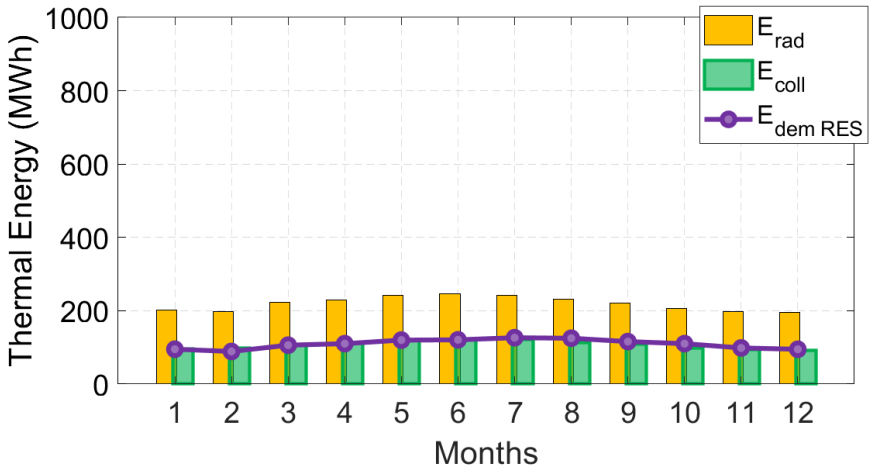

(a) *Residential*

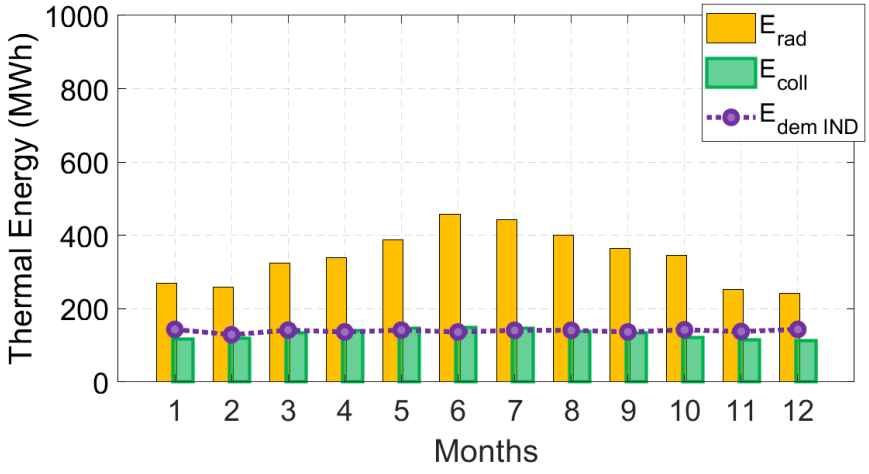

(b) *Industrial*

Figure 4.16: *Monthly simulation results for CRS at Aswan condition.*

In order to globally evaluate the performance of the investigated configurations, the annual energy balance is reported in Table 4.7. It can be seen that the CSP plants based on CRS require a lower amount of solar energy (consequently, a lower aperture area) to meet both load profiles. This advantage is more noticeable for the ambient condition of Giza and in the industrial load case. The surplus of collected energy (requiring the defocussing of a fraction of solar devices) is higher for the plant configurations based on parabolic troughs.

Finally, the economic feasibility of the solutions is considered. According to the results in Tab. 4.6 the PTC are cheaper only for residential case in Aswan; introducing the LCOE function this benefit is canceled and the CRS results more convenient for all the case: for Giza, the advantage is about 30% (13.43 ¢$/kWh$ and 14.72 ¢$/kWh$ vs. 9.9 ¢$/kWh$) and is reduced to 5% at Aswan where a minimum cost of 6.57 ¢$/kWh$ is achieved for the industrial load.

Table 4.7: *Technical and economic annual performance for each combination considered.*

		Giza		Aswan	
		PTC	CRS	PTC	CRS
Residential					
Solar energy	(GWh)	5438.3	2908.3	2809.2	2636.3
Collected heat	(GWh)	2531.9	1299.9	1485.4	1286.7
Heat demand	(GWh)	1300.0		1312.2	
Energy surplus	(%)	102.2	6.3	20.4	1.4
LCOE	($/kWh$)	0.1343	0.0992	0.0705	0.0696
Industrial					
Solar energy	(GWh)	8008.9	4084.9	4166.4	4084.9
Collected heat	(GWh)	3728.7	1774.9	2203.0	1576.6
Heat demand	(GWh)	1655.8		1672.7	
Energy surplus	(%)	133.7	16	39.4	1.6
LCOE	($/kWh$)	0.1472	0.0988	0.0694	0.0657

CHAPTER 5

Power mix production systems

5.1 Introduction

The concern for the reduction of GHG emission brought countries and governments to diversify the energy portfolio. Most competitive countries realize that the investment on renewable energy is fundamental to guarantee a green energy production in the future [149]. Many governments plan, for the future of the energy mix, the introduction of large parts of renewable energy considering a very low energy cost scenario [150]. The development of renewable energy source has attracted great interest over the last decades thanks to the undeniable environmental and economic benefits. The high renewables energy potential of the MENA region faces with the low level of electricity generation from renewables. MENA countries have a huge amount of renewable sources, but their use is limited to only 3.5% of electricity generation and the region still contributes to 38% of the world GHG emission [151]. The IRENA report underlines that government policies play a crucial role to create a solid renewable strategy. Among the most ambitious plan in MENA region are cited the "*Integrated Sustainable Energy Strategy to 2035*" (ISES 2035) of Egypt and the UAE Energy Plan 2050 to cut carbon dioxide emissions, increasing the clean energy contribution by 42% and 50 % respectively [152, 153]. The study proposed by Hass [154] et al. deal with a possible 100% renewable grid solution in Chile at 2050 based on a detailed forecasting model. Also in the Euro-

pean region, with lower level of solar radiation, but interesting wind potentials, important studies reports electricity production totally covered by renewables [155].

The large renewables penetration causes an overproduction on the electric grid with large power variability in time and space. Nevertheless, the continue and non-uniform introduction of photovoltaic, coupled with the low level of LCOE achieved, force the scientific community to evaluate news, tailored and accurate solutions over the subsidies and policy support [35]. To solve the problem of a discontinuous energy production from the renewables, a large as possible interconnection of the electricity grid and the optimization of the system [156]. Inside this way, the paper proposed by Morten et al. [157] deal with a fully or highly renewable European power system and underline the importance of a proper control strategy of the grid and the availability of efficient energy storage and an optimized power mix. Recently, more hybrid renewable energy systems (HRES) are developed when the combination of more than one technology allows to reduce the costs and increase the reliability; Sezer and Koç stress on the over-sizing of the independent systems to guarantee the system reliability [158]. Murugaperumal et al. [159] underline that studies on HRE system highlighted the necessity of correctly size the system to to meet the forecasted load demand for reliable electrification. The large variability of the renewables production force the system to introduce higher level of energy store system (EES) especially in hybrid power mix as reported by de Sisternes et al. in [160]. The electric storage has been represented the limit of Photovoltaic and wind generation. The increasing of Li-Ion batteries production and, the consequent, economy of scale has led to a consistent cost reduction as confirmed in the Irena Report "Electricity storage and renewables: Costs and markets to 2030" [37]; however, the integration of thermal energy storage in the electricity production is still more convenient [161] . The main role of the storage is represented by island operation as reported by rural community or, supported by government vision, in futurist carbon free city. Determine a profitable layout of the hybrid renewable system requires an optimization of the capability and a detailed techno-economic evaluation; The best solution of a power mix based on the renewables is represented by reach almost the same LCOE of traditional technologies (close to 7 ¢USD/kWh [150]) with a consistent reduction in terms of CO_2 emission. Most common hybrid solution is based on solar PV and wind, as proposed by Ghorbani et al. [162]; however, the storage system challenges should represent an opportunity for CSP-PV hybrid plant: Servert et al. demonstrated that it is possible to increase the dispatchability [163]. In the review provided by Ju at al. it is underlined that the characteristic of electric power from steam turbines helps to control the grid stability, the CSP could improves the production quality reducing the impact of PV to the grid frequency [164]. Furthermore, Zaalouk observes that

the hybrid solution can reduce by 11% the LCOE and by 40% the CAPEX [165]. The system sizing is still an open question, mainly because the operative conditions, such as available DNI, environmental conditions and the output curves, have a great impact on the performance [166]. Liu et al. propose an integration between PV and CRS where the overproduction and the fluctuating electricity of PV system feed an electric heater contributing to the TES charge of the CRS. The CSP modulates its power production according to PV output to provide a constant power reaching a LCOE of 16.93 ¢$/kWh. Changing the delivering strategies the LCOE could be reduced to 12.80 ¢$/kWh [167]. Zhai et al. studies the different behavior of the system if a different dispatch strategies is adopted; results underline that integrate the PV and CSP output can increase the system capacity from 44% to 79% when a constant output is imposed [168].

This thesis section, starting from results and the assumption of the previous chapter 4, first introduce the modeling of the renewable hybrid power plant with detailed design and off-design component design, then a techno-economic analysis is provided to evaluate the performance and the flexibility of the system under a load-following delivery strategy. The work includes an accurate up to date cost analysis and perform a multi-variable optimization of the power mix (CSP-PV-wind) in term of minimum LCOE with a selected renewable fraction of 90%.

5.2 Design condition and assumption

In the light of the statements of the Egyptian Ministry of Electricity & Renewable Energy report [169] about the presence of a large number of isolated power plant, a techno-economic model has been developed to increase the electrification of mid-size off-grid communities. Starting from the remarks of Pierro et al. on the necessity to correctly predict the energy demand and production to assess the reserve [170], a model has been developed to evaluate the power mix plant performance in a load following control strategy. The electric loads daily trend, included in the model, have already been presented in detail in the previous chapter (section 4.2 - Fig. 4.1).

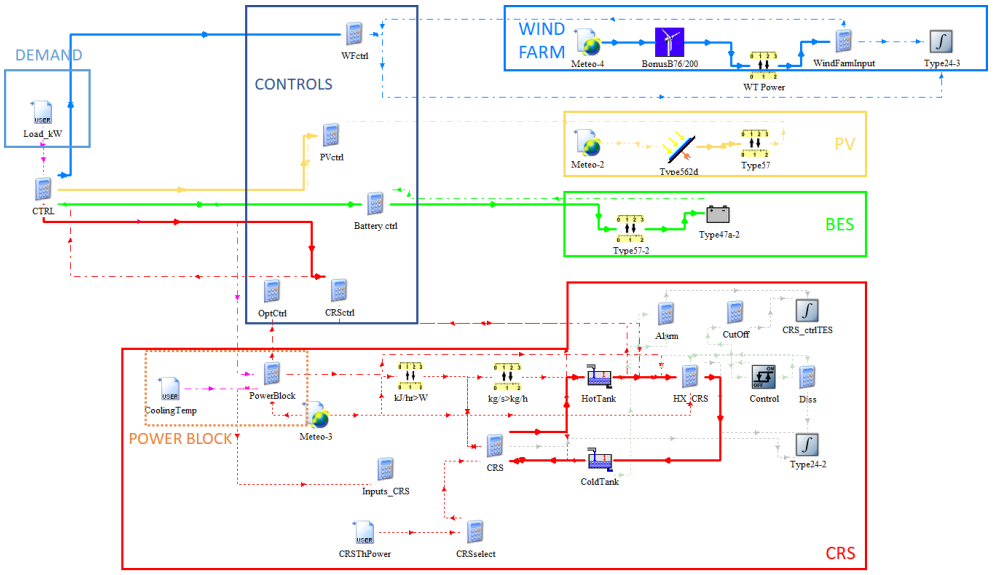

Figure 5.1: *Trnsys deck of the power mix plant.*

The simulation of the operation of the hybrid system and the optimization of the power mix have been carried out with the software Trnsys18. The developed model, shown in Fig. 5.1, includes the cooperation, under a load following control strategy, of three different power plant: photovoltaic, wind and concentrated solar power and the adoption of two different types of storage: thermal energy storage and electric energy storage.

The model of the hybrid renewable plant is based on an AC-bus as reported in Fig. 5.2. The CSP plant, based on the heliostat field that fed a Rankine power cycle with a molten salt thermal storage. The electric energy produced by the photovoltaic field and from the wind farm is transformed from DC to AC before the bus and, in case of overproduction, to the battery storage.. The EES is connected to the bus with an AC-to-DC inverter and a DC-to-AC rectifier. The efficiency of the inverter is set equal to 98% and the efficiency of the rectifier is equal to 82%. The battery is assumed based in the Li-Ion technologies and the round-trip efficiency is equal to 90% as reported by a manufacturer [171].

A diesel GenSet feed by biofuel is includes in the model in the aim of cover the residual load (10% annual) and supply the electricity in case of failure of the renewable power plants.

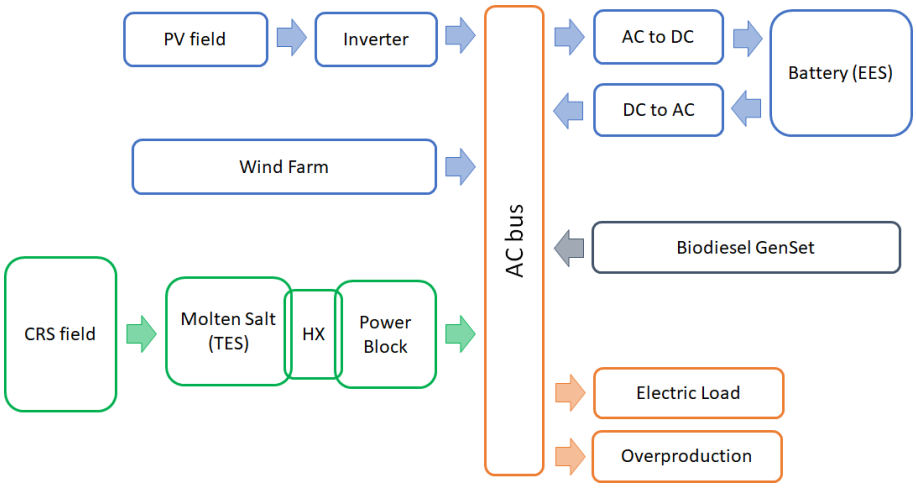

Figure 5.2: *Schematization of the multi-generation grid.*

The control strategy adopted in the model aim to maximize the self-consumption of electricity, as suggested by Zurita et al. [172], and a priority ranking is defined as follow:

1. Base load of steam turbine (if on)
2. PV and Wind farm directly to the AC bus
3. Battery
4. CSP

First of all, to ensure continuous operation of the steam turbine, the electric renewable subsystem (PV+Wind) must satisfy the electric load net of the base load of the steam turbine (if is running). In case of PV+Wind overproduction the surplus is delivered to the battery (EES) according to the power limit (charge and discharge); if the battery is at full state of charge the excess of production is delivered to the grid. In the event of electric load deficit after all the renewable production system, the difference is covered by the auxiliary diesel GenSet.

The model does not include the time response (ramp speed) of the components and of the storages, anyway, the ramp of all the components (including the steam turbine) can be considered within one time step (0.125 hour) [173].

5.3 Methods and tools

Analogously to the previous CSP system study, the hybrid plant has been located in the MENA region and the two location compared are Giza and Aswan, in the Arab Republic of Egypt. The meteo data, based on Meteonorm database [174], has been included in the development of the Trnsys model. A locations comparison is proposed in the figures 5.3 and 5.4, where the annual amount of renewable resources is reported. The high resource availability of the location, coupled with the low temperature, improve the operation of the solar-based plant. Furthermore, the lower ambient temperature coupled with the stable level of the relative humidity allow to a better performance of the solar plants (Fig. 4.5a) [175]. The DNI profile has a huge impact on the selection of design parameters [176]. From the available data of Meteonorm database, the annual amount GHI and DNI are respectively 2457 kWh/m^2 and 3058 kWh/m^2 for Aswan, and 2069 kWh/m^2 and 2097 kWh/m^2 for Giza. Thanks to the high irradiance level, the integration of CSP in hybrid system is encouraged. The figure 5.4 reports the duration curve of the wind intensity; the potential of the location is well represented by the number of windy hours during the year greater than 5500 with wind velocity at least of 3 m/s. Moreover, the government propose a substantial contribution (12%) of the wind generation in the country [100].

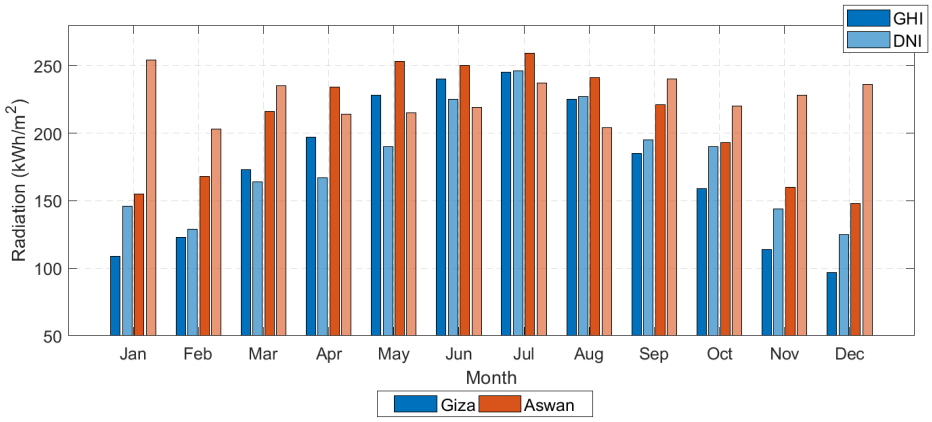

Figure 5.3: *Global and direct radiation in Giza and Aswan.*

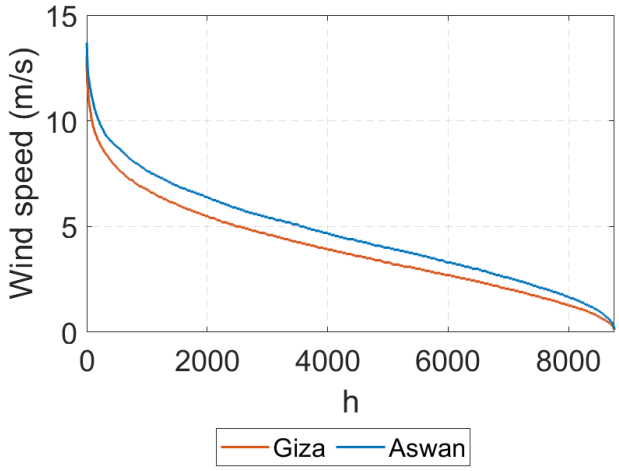

Figure 5.4: *Duration curve of wind speed in Giza and Aswan.*

5.3.1 Renewable plant model

The Trnsys model includes numerous component available on the specific TESS libraries and homemade routines in order to model and simulate user-defined plant components. A transient simulation has been carried out with a time step of 0.125 hour. The selected value of time step required a large computation time but ensure the evaluation of fast transient operation linked to the thermal energy storage. The numerical simulation reproduces the behavior of the plant under real operation conditions over one-year period.

PV model

The photovoltaic field model was based on a manufacturer data-sheet and include the performance derating related to the temperature variation and radiation off-design. Table 5.1 reports the main parameter of the selected photovoltaic model. The photovoltaic field was modeled as a cluster of 100 kW_{dc} fields. The model includes the losses between the field and the AC bus: 2% transportation losses, 18% power factor and 2% inverter according the design literature.

Table 5.1: *PV module specifications (mod. Solarworld poly250).*

Performance characteristic	unit	value
Maximum power (P_{max})	W	250
Open circuit voltage V_{oc}	V	37.6
Maximum power point voltage V_{mpp}	V	30.5
Short circuit corrent I_{sc}	A	8.81
Maximum power point current I_{mpp}	A	8.27
Module efficiency η_m	%	14.91
Thermal Characteristic		
Nominal operating cell temp (NOCT)	$°C$	46
Temperature coefficient I_{sc}	$\%/°C$	0.051
Temperature coefficient U_{oc}	$\%/°C$	-0.31
Temperature coefficient P_{mpp}	$\%/°C$	-0.41

Wind farm model

The wind farm plant model is based on the performance curve of a reference wind turbine provided by the manufacturer. The nominal capacity of the wind turbine is 2 MW and the main characteristics and operating parameters are reported in Tab. 5.2. In Figure 5.5 is reported the wind turbine power curve with respect to the wind speed. The model evaluates the electricity production of the wind farm time-step by time-step. In case of a wind farm, the power production does not include a layout optimization and does not consider the interferences on downstream wind turbine.

Table 5.2: *Wind turbine specification.*

	unit	value
Rotor diameter	m	76
Swept area	m^2	4500
Rotor max speed	u/min	16
Tip speed	m/s	64
Power density	W/m^2	444.44

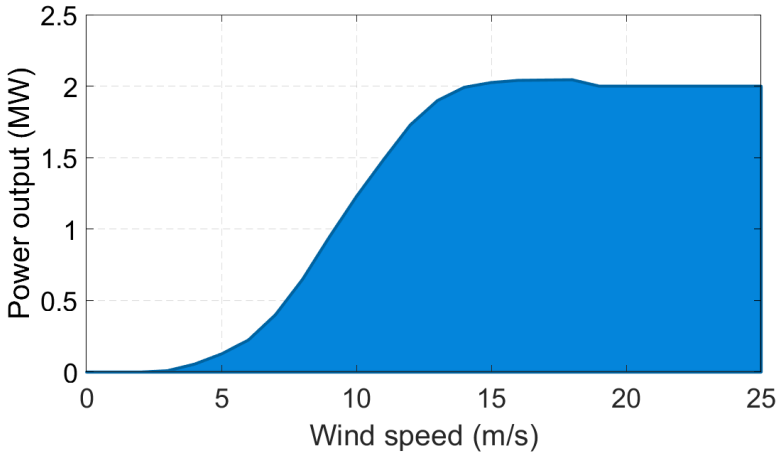

Figure 5.5: *Wind turbine output power curve.*

CSP model

The CSP model implemented in the hybrid system is based on the CRS technology: based on the results of the chapter 4, the tower has proven to have the best load-following capability. As already commented, the performance of the heliostat field is summarized with a map as function of design thermal power and solar zenith angle (Fig. 4.8). For further details on the configuration of CSP and on the efficiency map, please, refers to the previous chapter sections 4.2.1, 4.3.1 and to the appendix A.

5.3.2 Economic model

The model includes an up to date component budget cost analysis. In particular, an accurate literature review allows to improve the reliability of the economic evaluation.

The photovoltaic global installed cost are currently between 1100 $/kWdc and 1210 $/kWdc [177], the IRENA report ”Renewable Power Generation Costs in 2018” [178] predict a reduction up to 793 $/kWdc. The minimum LCOE reported is equal to 0.067 $/kWh with the operation and maintenance cost (O&M) equal to 9 $/kW.

The Wind farm cost varies consistently between land bases and off shore. The major energy institutions (IRENA and EIA) are in agreement on the cost of onshore wind farm of 1454-1600 $/kW [179], and the well-know software SAM confirmed these values; furthermore, the Irena annual report [178] propose a cost projection to 1000 $/kW that could provide an LCOE minimum value of 0.046 $/kWh considering an O&M of 20 $/kW.

The Electric Energy Store represents the main parameter in the future of the PV-based energy plant. The cost of the EES has shown a consistent decrement in the last years. The "2018 U.S. Utility-Scale Photovoltaics-Plus-Energy Storage System Costs Benchmark," listed an electric storage system cost equal to 380 $/kWh [180] where the share of the Li-Ion battery component is equal to 209 $/kWh. More recently, the declared battery cost reduced to 176 $/kWh and a constant reduction in battery system price (-15% year), as reported by Bloomberg (2019) [181], supports the adopted battery cost close to 325 $/kWh.

The complexity of the CSP plant based on the CRS receivers force the authors to adopt a different cost evaluation. The variables of the heliostat field-based plant includes in the optimization require a component cost evaluation (aperture area, steam turbine capacity and storage volume) despite the unit cost adopted with the other technologies. The unit cost of the CRS field is function of the reflective area, based on the analysis provided in previous chapter 4.4. The budget cost adopted in the study has already been commented in Tab 5.3; the sum of the terms represents the direct cost. The total installed cost of the technology includes also the indirect cost as Engineering, Procurement, and Construction (11%), Contingency (7%) and Taxes (4%). The total installed cost of the Irena Report 2018 [178] allows to reach a minimum LCOE of 0.11 $/kWh but recent statements lower the limit to 0.075 $/kWh. The software SAM has shown a CRS O&M cost divided in fixed (66 $/kW) and variables (0.0035 $/kWh).

According to the costs reported in the literature, a resume of the adopted cost (installation budget and Operation and Maintenance) is reported in Table 5.3 and Table 5.4.

Table 5.3: *Installation costs of the renewable plants.*

Energy source			Installation cost
Photovoltaic		$\$/kW$	793
Wind farm		$\$/kW$	1000
Battery storage (Lit-Ion)		$\$/kWh$	325
CRS			
	Heliostat field	$\$/m^2$	$324 - 2.74 \cdot 10^{-5} \cdot A_{refl}$
	Molten salt storage	$\$/kWh$	22
	Steam power block	$\$/kW_e$	$15587 \cdot P_{PB}^{-0.232}$

Table 5.4: *Operation and maintenance costs of the renewable plants.*

Energy source	O&M	
	Fixed ($/kW)	Variables ($/MWh)
Photovoltaic	9	
Wind farm	44	
Battery storage (Lit-Ion)	10	3.1
CRS	66	3.5

The main economic parameter adopted by the scientific community, in order to assess a technologies comparison, is the Levelized Cost of Electricity (LCOE). In this work the LCOE has been selected as the term of comparison in the aim of select the best power mix combination. The LCOE evaluation, based on the equation 5.1, includes a technology lifespan project (each single plant represents a separate entity on the economical point of view). In particular, the LCOE evaluation was based on the technologies lifespan energy production (Tab. 5.5). The energy production includes the annual performance degradation of the components as reported in Tab. 5.5. The degradation of the PV modules has been considered in the value of 1%/year according to the PV data sheet. The wind farm annual degradation was well analyzed in [182] and the value adopted reflect the conclusion of the study. Battery lifetime and degradation effects are reported and analyzed by J. Haas and al. in [154]. The battery lifetime is considered equal to 7 year according to large DOD (depth of discharge) [183] and the maximum capacity loss of the battery equal to 20% at the end of component life.

The CRS degradation has been set to 0.5%/y. The values derived from different studies [184, 185] and include optical degradation, load losses in the pipes, mirror and receiver aging.

Table 5.5: *Lifespan and annual degradation.*

Energy source	Lifetime (LT)	Annual degradation (%/y)
Photovoltaic	20	1
Wind farm	25	0.7
Battery storage (Lit-Ion)	10	3
CRS	30	0.5

The power mix LCOE was computed as a weighted average of the single technologies LCOE as reported in the Eq. 5.1 and represent a new approach with respect the standard LCOE evaluation. In this case the LCOE value considers the LCOE of the component separately, every component with a specific lifetime and aging degradation. This mean that, at the end of the PV operativity, the PV plant will be replaced with a new one without affect the CSP

lifespan.

The equation 5.2 evaluate, as example, the lifetime global production of the PV field (PV_{prod}). The terms PV_{LTprod} (Eq. 5.3) represent the lifetime global derating as the average of the annual derating ($PV_{der,n}$) from the year of installation and the last year of operation. The term $PV_{prod,y}$ is the annual PV field energy production computed according to the load following control strategy in the first year of operation. The term PV_{LT} represent the lifetime of the technology. The single technology LCOE was computed according the equation 5.4, the canonical formula includes the global plant cost ($C_{plant,PV}$), the technology RF factor and the annual energy production ($PV_{prod,y}$, $batt_{prod,y}$, $WF_{prod,y}$, $PTC_{prod,y}$ respectively). The LCOE evaluation includes also the O&M cost dived into fixed and variable costs as listed in the Table 5.4. The RF factor, reported in the equation 5.5 starting from the technology lifespan (Ny) and the interest rate (i). The interest rate has been fixed at 8% of the 50% of the cost. The value of RF factor has been computed for each technology according the lifetime.

$$\begin{aligned} LCOE(\$/kWh_e) = (&LCOE_{PV} \cdot PV_{prod} + LCOE_{WF} \cdot WF_{prod} + \\ &LCOE_{batt} \cdot batt_{prod} + LCOE_{CRS} \cdot CRS_{prod}) / \\ &(PV_{prod} + WF_{prod} + batt_{prod} + CRS_{prod}) \end{aligned} \tag{5.1}$$

$$PV_{prod}(kWh_e) = PV_{LTprod} \cdot PV_{prod,y} \cdot PV_{LT} \tag{5.2}$$

$$PV_{LTprod} = \frac{1}{PV_{LT}} \sum_{1}^{n} PV_{der,n} \tag{5.3}$$

$$LCOE_{PV} = \frac{RF_{PV} \cdot C_{plant,PV}}{PV_{prod,y}} + OM \tag{5.4}$$

$$RF_{PV} = \frac{i(1+i)^{N_y}}{(1+i)^{N_y} - 1} \tag{5.5}$$

5.4 Methods

The model of the power generation plant was optimized using the software GenOpt, developed by the Berkley University, coupled with Trnsys. The optimization tool (GenOpt) minimized an objective function, reported in Eq. 5.6 under the constrains and select the best solution [186], as presented in the appendix B. The optimization procedure was based on the global Levelized Cost of Electricity (LCOE) minimization under the limit of a Renewable Factor (RF) equal to 90%. The residual part 10% has been supposed covered by a biofuel gen-set. The selected RF limit leads to a high penetration of renewables but prevent an excessive oversizing of the component to fully satisfy the demand even in the most disadvantaged situations (e.g. when the demand is high but

the radiation is low due to clouds); moreover, in this way, each power solution is left free to choose how to manage the deficit. A penalty factor has been included in the LCOE evaluation in order to force the optimization tool to reject the solutions under the selected Renewable Fraction. The function proposes a penalty as function of the annual electricity production in order to model a softer edge of the optimization limit during the second step of optimization (Hooke and Jeeves algorithm).

$$f_{min} = LCOE + Penalty_{(RF \leq 90\%)} \tag{5.6}$$

The optimization was performed in order to achieve the best configuration of a power mix plant where different technologies interact (i.e. PV, Wind turbine, EES and CSP with TES, as reported in table 5.6). In order to assess the convenience of the mixed solution, the configurations with the single technology are also considered: the optimal electric combination (PV + Wind + Battery) has been examined in addiction to the optimal CSP configuration (CRS + Steam Turbine + Molten Salt thermal storage) already optimized in the chapter 4. The selected layouts represent the common solution adopted in the renewables power integration.

Table 5.6: *Plant configurations.*

Configuration	Source	Storage
1 - electric	PV+Wind	Battery EES
2 - CSP	CRS	Molten salt TES
3 - mix	PV + Wind + CRS	Battery EES + molten salt TES

The variables (and their constraints) involved in the optimization procedure and reported in Table 5.7, represent the main parameter of the power mix.

The component degradation plays an important role in terms of lifetime electricity production. Furthermore, the adoption of a degradation parameter affects renewable fraction evaluation, the selected renewable fraction value is complete assessed the first year of simulation.

Table 5.7: *Optimization variables search space.*

Variable	Unit	Start value	Min value	Max value	Step
PV	MW_e	500	0	5000	10
Wind	MW_e	20	0	160	1
Battery capacity	MWh_e	500	0	1500	10
Solar field (A_{CRS})	km^2	0.86	0.5	4.2	0.1
Hours of storage (h_{tank})	h	12	6	24	1
Nominal power (P_{PB})	MW_e	75	20	150	2.5

5.5 Optimal configuration and results

The results of the optimization process in term of optimal component sizing of the three different plant configurations are studied for two load profile pattern (i.e. residential and industrial) and a sensitivity analysis on the available resource influence has carried out considering two locations with quite different characteristics: Giza and Aswan (as commented in sec. 5.3).

The best configuration for the residential load case are summarized in Table 5.8. It is worth noting that the fully electric solution (PV+W) is not convenient for both the location considered. Despite the lower radiation available in Giza, a minimum value of 20.13 $¢\$/kWh_e$ is achieved against the 22.13 $¢\$/kWh_e$ for Aswan: the installed PV area and the number of wind turbine are greater (total power of 627.5 MW_e) but the battery system with a capacity 40% smaller allows to contain the increase in costs. The high irradiance level of Aswan benefits the CSP solution that, with smaller components, guarantee a LCOE level of 6.96 $¢\$/kWh_e$ vs. the 9.80 $¢\$/kWh_e$ in Giza.

The adoption of the mixed solution cancel the support of the battery (since the cost is too high compared with the other components) and, starting from the CSP configuration, the tower system is reduce to be replaced mostly by the PV. Under Giza conditions, the electric technologies are more favored since the GHI and DNI values are similar but their cost is smaller. The design thermal power of the heliostat field is reduced by 100 MW_{th} and the tank is 30% smaller. Conversely, only a small fraction of PV is introduced in Aswan and the CSP design is nearly unchanged, unless a small reduction of the aperture field area (correspondent to a design thermal power of 50 MW_{th}). The mix configurations support a limited reduction of the LCOE: 0.63 $¢\$/kWh_e$ and 0.17 $¢\$/kWh_e$ in Giza and Aswan respectively.

Table 5.8: *Optimized component size of each combination for residential load case.*

Configuration		PV MW_e	Wind MW_e	Battery Capacity MWh_e	A_{CRS} km^2	h_{tank} MWh_{th}	P_{PB} MW_e	LCOE $\$/kWh_e$
Giza	PV + W	447.5	180	669	0	0	0	0.2013
	CRS	0	0	0	1.39	1141.41	75	0.0980
	MIX	56.6	4	0	1.17	793.75	63.5	0.0929
Aswan	PV + W	370	88	1020	0	0	0	0.2213
	CRS	0	0	0	0.86	682.5	65	0.0696
	MIX	19	0	0	0.76	715.00	65	0.0679

Table 5.9: *Optimized component size of each combination for industrial load case.*

Configuration		PV MW_e	Wind MW_e	Battery Capacity MWh_e	A_{CRS} km^2	h_{tank} MWh_{th}	P_{PB} MW_e	LCOE $\$/kWh_e$
Giza	PV + W	627	298	960	0	0	0	0.2265
	CRS	0	0	0	1.95	1563.75	90	0.0988
	MIX	53	25	0	1.63	1155.00	82.5	0.0976
Aswan	PV + W	482.5	186	1130	0	0	0	0.2122
	CRS	0	0	0	1.07	960.00	80	0.0657
	MIX	30.5	6	0	0.95	942.50	72.5	0.0660

Moving to the industrial case (Tab. 5.9), the penalization of the PV+Wind solution is still conspicuous but, compared to the residential load, the condition of Aswan are most favorable: the battery has a capacity 15% greater but the total power installed is only 668.5 instead of 925 MW_e achieving a LCOE of 21.22 ¢$/kWh_e$ (saving almost 1.5 ¢$/kWh_e$).

Compared to the residential case, the wind resource is more exploited, in fact, the bell shape of the residential load fits better with the trend of solar technologies; whilst, the industrial peak demand in later hours requires greater tank and the more uniform wind presence during the day helps the production.

The solution in Giza seem to benefit more from the hybrid configuration in term of component sizing: the aperture are is reduce by 0.32 km^2 (equivalent to almost 150 MW_{th}), the tank size by 26% (thanks to the contribute of the wind) and the nominal power of the steam turbine by 7.5 MW. The power mix case reduce the LCOE to 9.76 ¢$/kWh_e$. For Aswan, the CSP and the mix solutions are nearly equivalent (with LCOE around 6.6 ¢$/kWh_e$), emphasizing the great impact of direct radiation exceeding 3000 $kWh/m^2 - yr$ and with DNI peak in winter months: 50 MW_{th} from the heliostat field are replaced by 30.5 MW of PV and 6 MW of wind turbine and the steam turbine is 7.5 MW smaller.

5.5.1 Daily simulation results

In this section are reported the results of the transient simulation carried out for a one-year period. The charts 5.6, 5.7, 5.8, 5.9 report the details of two days in order to highlight the plants operations in summer, characterized by a high renewable resource availability, and winter season when the ambient conditions are the worst.

A general trend is observed for the fully electric solutions and the PV+WF plant performs similarly for both the demand. The contribute of the battery in summer is limited to few hours and the wind covers most of the overnight load (figures 5.6b, 5.7b, 5.8b and 5.9b); in winter the overproduction of PV feeds the battery to extend the production over the night (as long as possible). The

storage represents an important source of energy but non-sufficient to conclude the daily load and a nighttime Gen-set operation is needed.

The solutions with tower plants show the greatest variation with the location (i.e. the radiation) and the demand profile. In winter, especially due to Giza conditions, resource availability is more erratic and near-zero tower production could occur for up to 10 hours (Fig. 5.6c and 5.8c). On the contrary, in Aswan, the winter production is higher In summer period, for many hours (up to 6) per day a fraction of the troughs must be defocussed, since the hot storage tank is at the maximum capacity and the tank level is never lower than 40% ; however, only for the industrial case in Giza the CSP plant cover 100% of the load in summer months (Fig. 5.8d), for all the other case, the tower has an installed capacity (P_{PB}) lower than the demand level and a deficit fraction occurs also in summer.

Finally the electricity production of the power mix is considered. The chart evidences that the combination highlight strengths and weaknesses of the technologies adopted. In particular, the hybrid solutions works better than the single plants in summer days: the integration of PV and wind turbines increase the production mainly in central hours (where the tower was limited by the installed capacity). Whilst, in winter, with hard ambient condition, the mix perform worst than the single CSP. During winter period the reduction of CRS field aperture is not compensate by the photovoltaic and the wind (unpredictable) that have been incorporated, and the plant operation leads to a storage depletion. The reported chart shows the hardest operative condition but, on annual basis, the RF fraction is achieved anyway.

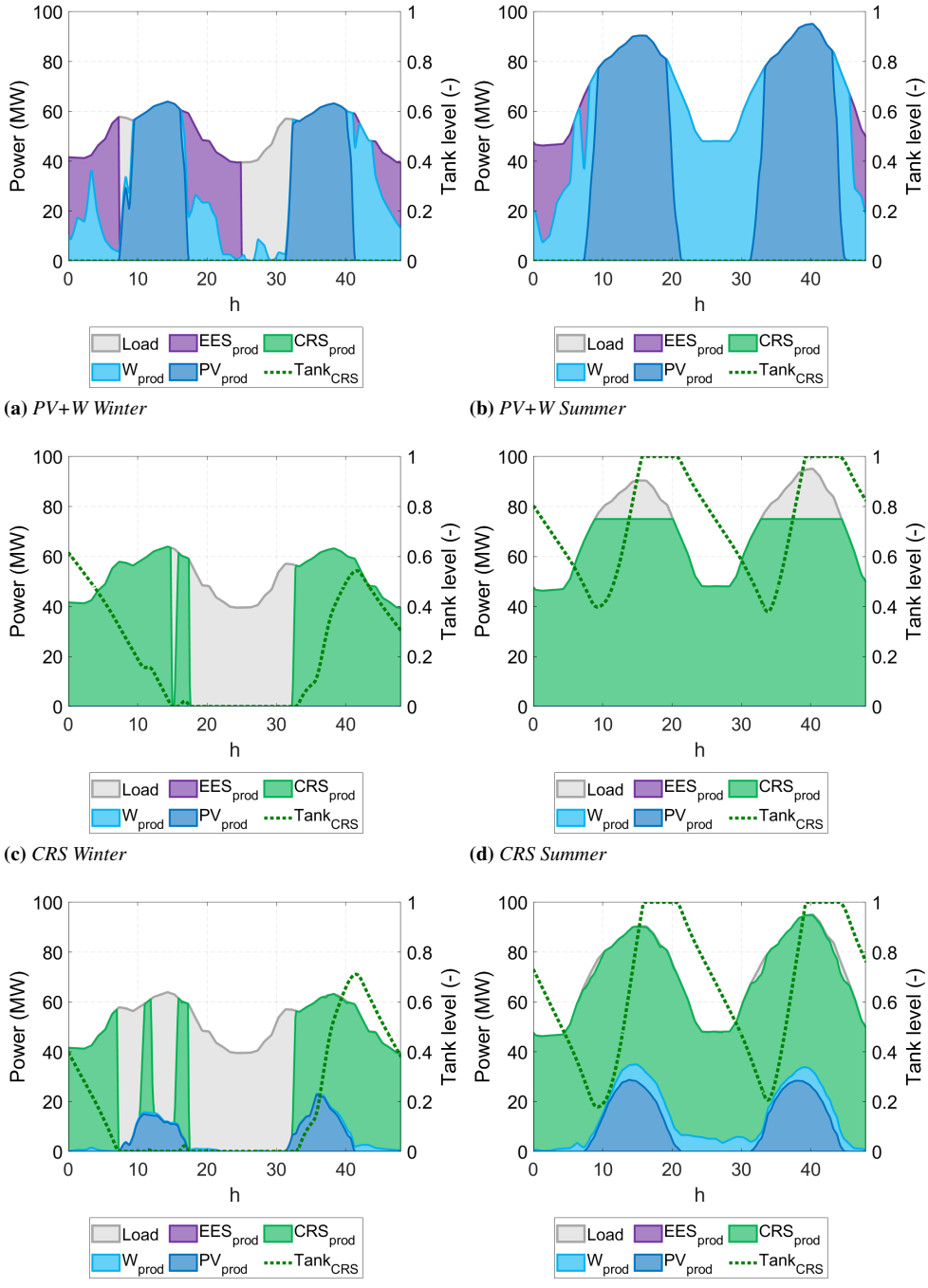

(a) *PV+W Winter*

(b) *PV+W Summer*

(c) *CRS Winter*

(d) *CRS Summer*

(e) *MIX Winter*

(f) *MIX Summer*

Figure 5.6: *Daily simulation results for residential case in Giza.*

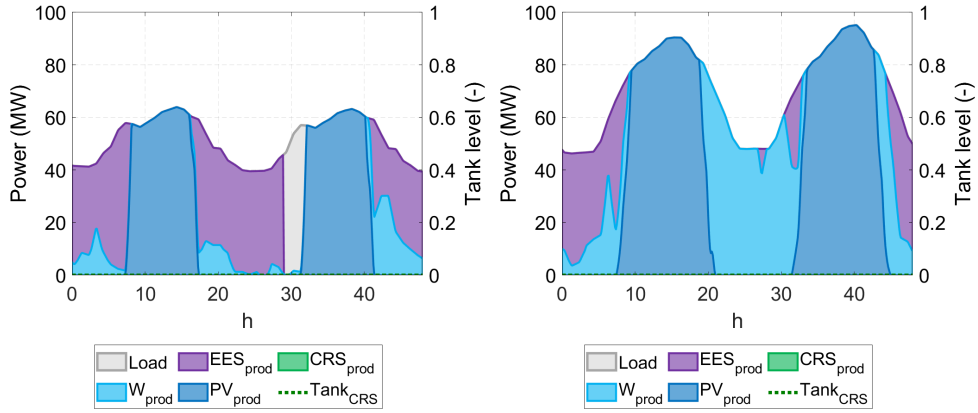

(a) *PV+W Winter*

(b) *PV+W Summer*

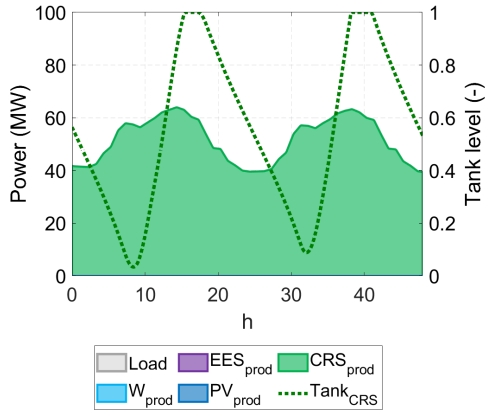

(c) *CRS Winter*

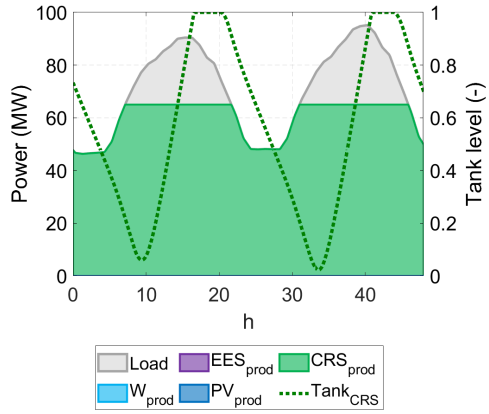

(d) *CRS Summer*

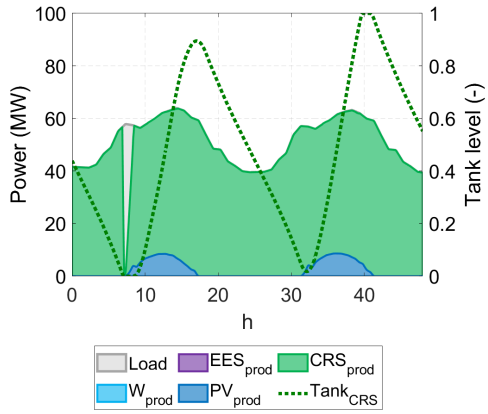

(e) *MIX Winter*

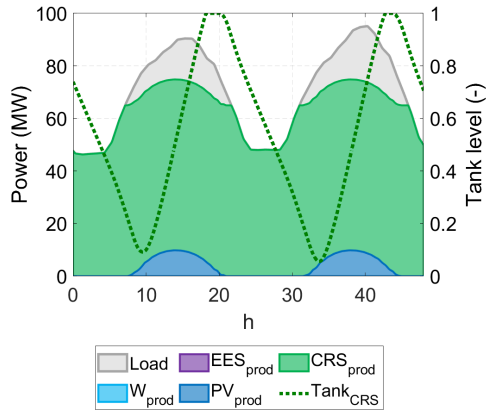

(f) *MIX Summer*

Figure 5.7: *Daily simulation results for residential case in Aswan.*

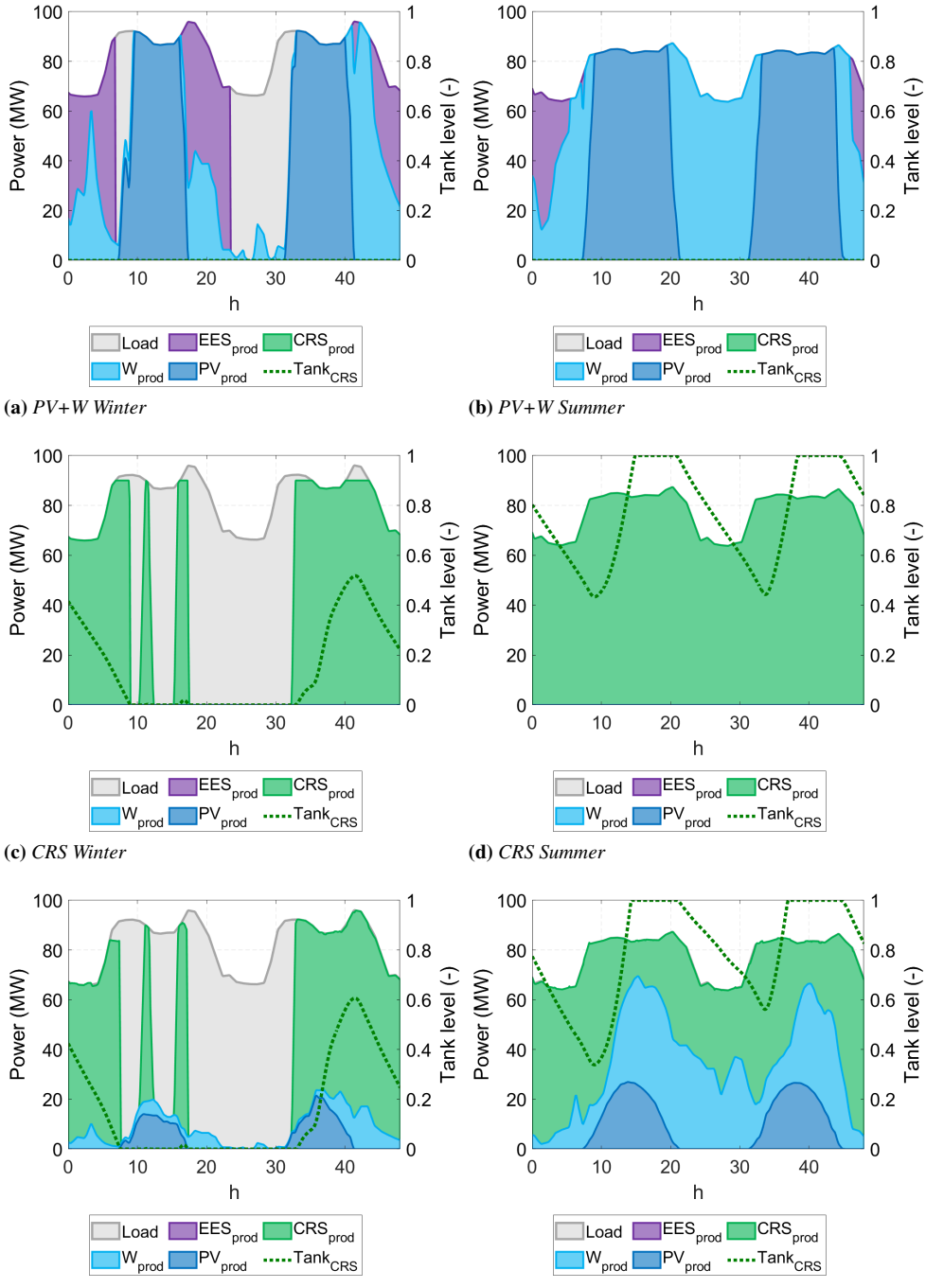

(a) *PV+W Winter*

(b) *PV+W Summer*

(c) *CRS Winter*

(d) *CRS Summer*

(e) *MIX Winter*

(f) *MIx Summer*

Figure 5.8: *Daily simulation results for industrial case in Giza.*

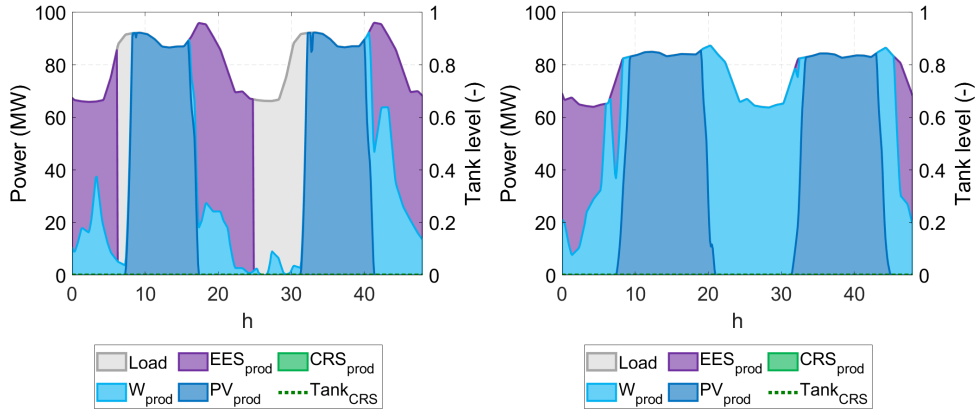

(a) *PV+W Winter*

(b) *PV+W Summer*

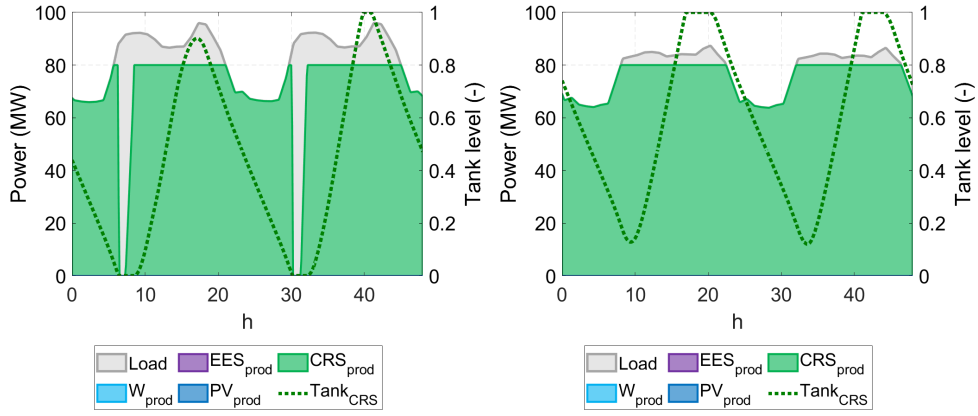

(c) *CRS Winter*

(d) *CRS Summer*

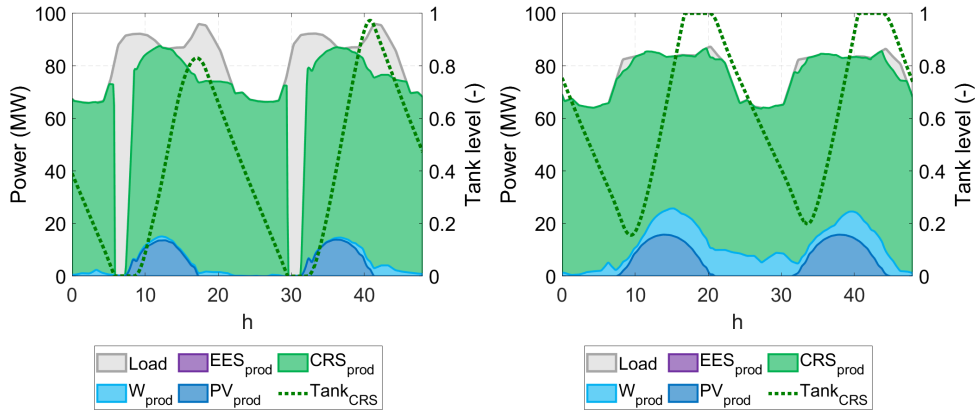

(e) *MIX Winter*

(f) *MIX Summer*

Figure 5.9: *Daily simulation results for industrial case in Aswan.*

5.5.2 Monthly and yearly performance

The tables 5.10 and 5.11 report the annual electricity production for all the cases considered. The electricity overproduction and the defocus in term of electricity for CSP plant are also mentioned. In the residential case, in the full electric solution, the PV provide 50% of the demand and only 10-15% is given by the wind, the remaining part is left to the battery. It is worth noting the high level of overproduction (65% and 48% for Giza and Aswan, respectively). whilst, considering the CRS plants, the defocus fraction is limited to less than 10%. The power mix perform better and the overproduction drop to 8% and 1% (for the two location). The production is mainly provided by CSP and PV with a marginal part is left to PV and WF and a complete reduction of the EES. Similarly, in the industrial case (Tab. 5.11), the contribution of each technology is almost unchanged but the overproduction is significantly increased.

Table 5.10: *Electric production contribution from each technology (%) and over production for residential case.*

Configuration		PV	Wind	Battery	CRS	PV-W over	CRS over
Giza	PV + W	49	15	25	-	65	-
	CRS	-	-	-	90	-	10
	MIX	12	2	0	77	0	8
Aswan	PV + W	49	10	32	-	48	-
	CRS	-	-	-	90	-	8
	MIX	5	0	0	86	0	1

Table 5.11: *Electric production contribution from each technology (%)and over production for industrial case.*

Configuration		PV	Wind	Battery	CRS	PV-W over	CRS over
Giza	PV + W	45	18	27	-	85	-
	CRS	-	-	-	90	-	17
	MIX	9	8	0	74	0	15
Aswan	PV + W	45	14	32	-	61	-
	CRS	-	-	-	90	-	4
	MIX	6	2	0	82	0	2

The figure 5.10 and 5.10 shows the monthly production of the tree configurations compared with the electric load. The bar chart reports that the PV+W configuration, under Giza condition, report a constant production across the year as suggested from the daily trend; an analogous trend is observed for the CSP based configuration in Aswan. The Mix configurations seasonal production, in the residential case, reflect the layout composition with high productiv-

ity in summer and good productivity in winter months. In the industrial load case, the CRS and the mix configurations shows a similar behavior in summer, whilst the mix increases or decreases the production in winter, for Giza and Aswan respectively.

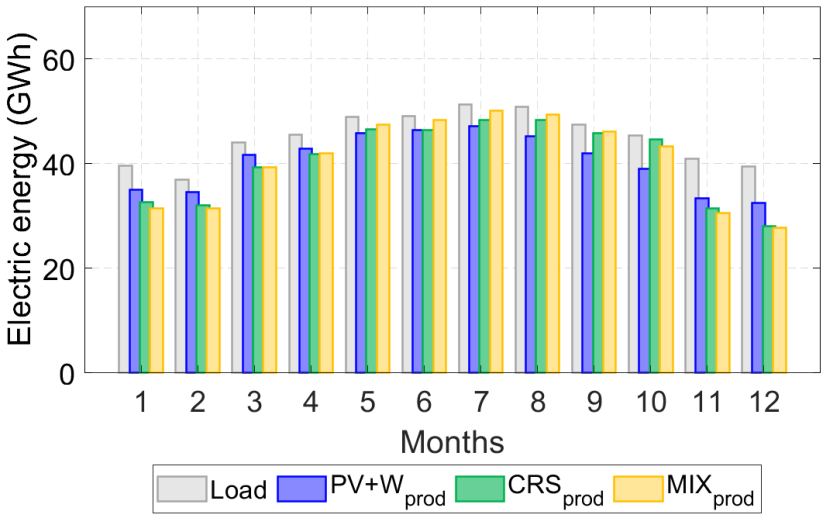

(a) *Giza*

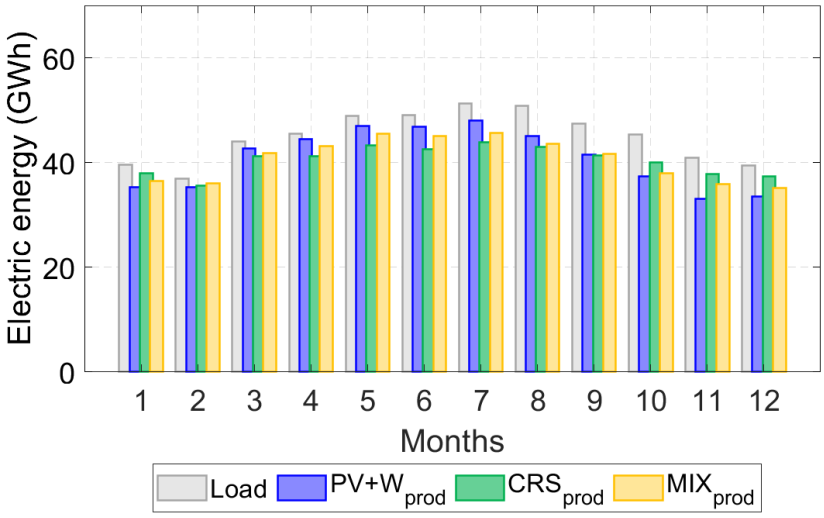

(b) *Aswan*

Figure 5.10: *Monthly simulation results for residential load.*

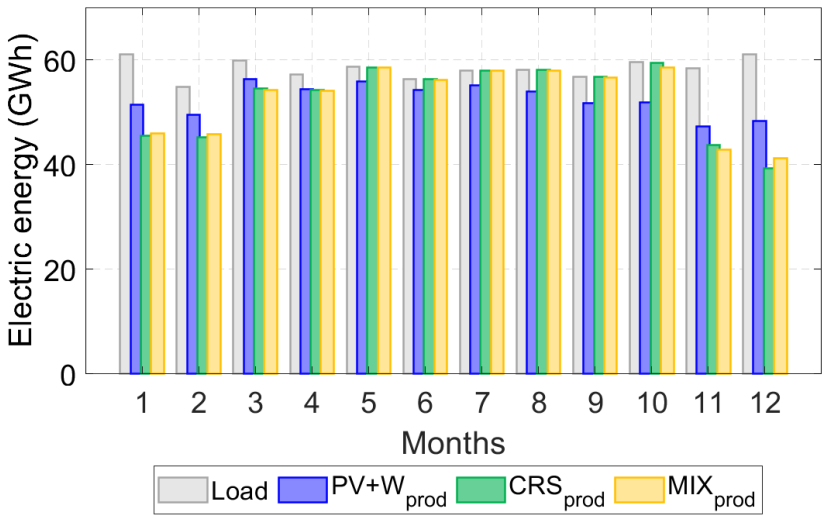

(a) *Giza*

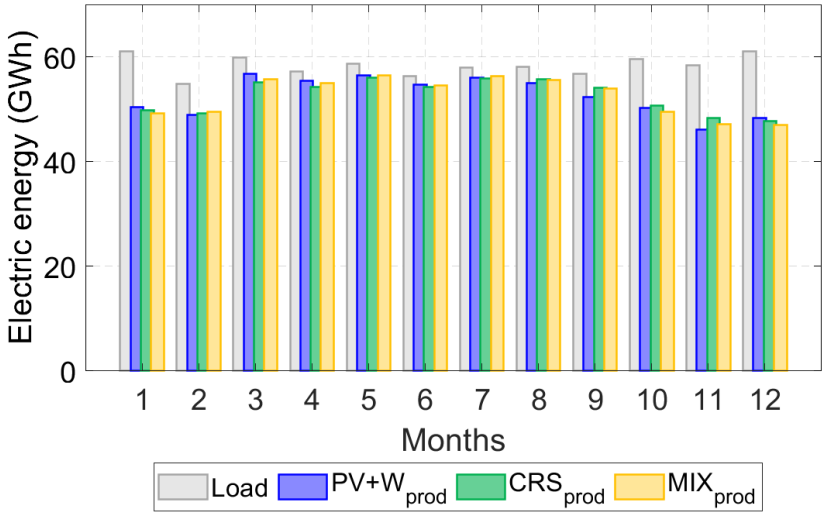

(b) *Aswan*

Figure 5.11: *Monthly simulation results for industrial load.*

5.5.3 LCOE analysis

The optimization result shows, as presented in tables 5.12 and 5.13, the LCOE variation moving from a single technology solution to an optimized power mix. Nevertheless, the value highlight that, under the constraint of a very high renewable fraction, the CSP solution shows a better result compared to the full electric one (PV+Wind+Battery) due to the high unit cost of EES. The LCOE

reported from CSP-based layout is 2-5% higher with respect the mix, but 50-60% lower with respect the PV-W-based one. Furthermore, the LCOE composition is also investigated. The PV+W solutions show that the battery, with an LCOE close to 0.40 $\$/kWh$, is the components responsible for the high cost of the electricity produced (higher than 20 ¢$\$/kWh$). In order to assess the selected RF, the plants require a larger capacity with high level of overproduction that increases the cost of each technology; moreover, the wind farm LCOE is penalized by the unpredictability of the resource. Despite the higher capital cost, the CRS plants have shown a better load following capability that allows to highly reduce the LCOE cost. The mixed configurations benefit from the low-cost storage of TES with the advantages of sunny hours production from PV plants: the LCOE of the PV and from the wind farm represent the component that reduce the global cost of the electricity whilst the CSP and the battery, on the other side, are essentially to ensure the night operation and the Renewable fraction achieved.

Under the assumption of selling to the grid the surplus of energy that cannot be exploited, the variation of LCOE of each solution is reported in the tables. Since the full electric solutions are characterized by the higher fraction of surplus would benefit most from the revenue (up to 2 ¢$\$/kWh$) but it is not enough to make the solution convenient compared to other configurations.

Table 5.12: *LCOE composition and revenue for residential case configurations.*

Configuration		LCOE	PV	Wind	Battery	CRS	Revenue	Δ LCOE
			(¢$\$/kWh_e$)				($M\$$)	(¢$\$/kWh_e$)
Giza	PV + W	0.2013	0.1248	0.1982	0.3548	-	9.88	0.0204
	CRS	0.0980	-	-	-	0.0980	0.59	0.0012
	MIX	0.0929	0.0660	0.0828	0	0.0972	0.50	0.0010
Aswan	PV + W	0.2213	0.1035	0.1544	0.4245	-	7.31	0.0149
	CRS	0.0696	-	-	-	0.0696	0.48	0.0010
	MIX	0.0679	0.0571	0	0	0.0685	0.07	0.0001

Table 5.13: *LCOE composition and revenue for industrial case configurations.*

Configuration		LCOE	PV	Wind	Battery	CRS	Revenue	Δ LCOE
			(¢$\$/kWh_e$)				($M\$$)	(¢$\$/kWh_e$)
Giza	PV + W	0.2265	0.1482	0.2169	0.3638	-	16.66	0.0265
	CRS	0.0988	-	-	-	0.0988	1.39	0.0022
	MIX	0.0976	0.0660	0.0828	0	0.1027	1.21	0.0019
Aswan	PV + W	0.2122	0.1149	0.1753	0.3666	-	11.88	0.0188
	CRS	0.0657	-	-	-	0.0657	0.31	0.0005
	MIX	0.0660	0.0571	0.0828	0	0.0662	0.20	0.0003

Conclusions

This thesis dealt with the development of models for the evaluation and the optimization of solar tower plants in term of single component and entire system. Due to the higher penetrability of non-programmable renewable technologies, it is important to promote the development of CSP plants which have characteristics of reliability and flexibility that allow to replace fossil resources in a remote or weakly interconnected grid.

In the first part of the work, a detailed analysis of the design and the component size of the CRS field system has been provided. The algorithm relies on a comprehensive model that simulates each single heliostat and evaluates the optical performance of a mirror field coupled with a central receiver on the tower top.

The influence of the main geometrical parameters has been assessed in order to increase the performance of CRS solar field and different design strategies were considered to increase the competitiveness. Mirror layout and tower height have been optimized for two different field sizes (i.e. 400 and 6400 heliostats, corresponding to a design thermal power of 30 and 500 MW_{th} respectively) and for two target functions: maximum efficiency and minimum LCOE.

The optimization procedure provides the best combination of radial spacing (ΔR) for the heliostat rings and tower height in order to achieve the best technical and economic performance. A taller tower leads to a more expanded optimal solution and the target function modify the best tower height. In the small case, the value that maximize the efficiency is clearly identified; on the contrary, the efficiency curve vs. Ht has an asymptotic trend in the large field. The optimization based on minimum LCOE leads to plant configurations with smaller towers and first mirror rows closer to the tower.

The main novelty introduced is the analysis of the impact of the design period on the performance of the layout: three different design periods, i.e. March, June, and December, are investigated and discussed. The design period does not influence significantly the optimal radial spacing, but the mirror rings' organization is strongly affected. Assuming for all the cases an external cylindrical receiver and a surrounding field, for months with a high design Zenith angle (i.e. June) the more effective layout has an uniform heliostat distribution over 360°, while conversely for December the optimized layout still allocates most of the heliostats in the north region of the field. The higher is the Solar Zenith angle, the higher is the field efficiency in the design conditions; nevertheless, the annual performance is enhanced for a design Zenith of about 20°(March solar conditions). Changing the solar altitude, the annual average efficiency has a deviation in the range $\pm 1.5\%$

The design period affects significantly also the efficiency seasonal variation: the layouts generated to maximize power production in winter exhibit lower annual energy yields but with limited efficiency variations during the year. The configurations designed for June conditions have the maximum efficiency values in summer months and the minimum efficiency values in winter. The layouts based on March as design period allow to maximize the annual yield.

A sensitivity analysis has shown that the unit costs of heliostats and tower have a relevant impact on the optimum layout configurations for the small size CRS plants, while limited for the large ones. Moreover, the heliostat dimension has been varied and it was found that smaller mirrors ensure a better efficiency especially for lower tower height and an aspect ratio of 2/3 maximize the efficiency compared with the square geometry.

Similarly to the layout analysis, a receiver optimization is performed for the technical and economic function. When the receiver is included in the analysis, the efficiency curves become flatter for different tower heights. A clear optimum design dimension that maximize the absorption efficiency are identified and a bigger receiver is required when the tower height is increasing. Introducing the economic evaluation, the smallest receiver that satisfies the flux limit becomes the best solution. This demonstrates that the receiver cost has a greater impact on the LCOE than the system performance, and the flux constraints imposes the minimum allowable size.

When the power of the system is low (i.e. the small case), a cavity receiver structure has been proved to be a cheaper alternative to the most common external solution. The cavity configuration slightly penalize the optical efficiency of the field but the absorber surface more sheltered ensure a better η_{abs}. With the attention to the seasonal behavior of the performance, it is observed a penalization in summer period whilst a nearly constant efficiency is achieved from September to March. The cavity configuration could increase the load-

following capability of a small-scale plant in the case of peak demand in winter months.

In the second part of the thesis, the load following capability of full-solar CSP plants has been assessed and the operation of the whole system has been investigated on annual basis. The properties of CRS are compared with the more diffuse PTCs and the investigation has been carried out for two power demand patterns, namely industrial and residential load and for two different ambient condition: Giza with high humidity and lower temperature, and Aswan with high DNI level and an irradiance peak in winter. This analysis is limited to the solar field with the hypothesis that the steam turbine is always able to deliver the required power, according to the minimum and maximum operation limits (neglecting the ramp rate can be consistent with an adequate amplitude of the time step considered).

Starting from the results of the analysis of the first part an economic optimization of the tower system has been carried out for a set of nominal powers. It was found that the efficiency of different tower field is mainly function of the size and of the solar zenith angle and can be approximated with a map that is provided to the plant model.

An optimization procedure has been developed in order to find the aperture area, the storage capacity and the nominal power of the power block that minimize the cost of the system.

The different tracking system of the two CSP technologies (1-axis and 2-axis) involves two seasonal efficiency behavior and introduce an extra degree of freedom in the load following consideration: the comparison between the demand and the production patterns. The CRS plant configuration allows fulfilling the power demand minimizing the investment costs, for both electric load patterns. Thanks to a flatter efficiency curve and a more constant production throughout the year, the solar tower plant shows a better load-following capability: this feature is emphasized with the industrial load, which has small seasonal variations. The CSP plants based on parabolic troughs, on the contrary, need an over-sizing of the solar field area, because of the low optical efficiency in winter. This leads to a large surplus of collected heat in summer, thus requiring the defocussing of several troughs. This issue is particularly evident with the industrial load pattern. The residential load profile is more in-phase with the PTC efficiency curve: this reduces the difference in investment cost compared to the tower plant configuration. For all the considered cases, the role of a large TES system is fundamental to operate the CSP plant according to a load following strategy. The comparison between the two location underlines the great influence of the radiation level not only in terms of aperture area but also of tank size.

Once assessed the superiority of CRS in load-following application, the re-

newable hybrid power plant configuration is introduced to assess the production flexibility when different technologies are called to operate simultaneously to provide a fixed renewable energy fraction. A combination of photovoltaic panels and wind farm ensures a more uniform production throughout the year but it is not the most profitable solution due to the high cost of the electric storage and the high overproduction forces to dissipate a large fraction of energy. On the other hand, the PV could support the CSP with the daily production and helps to reduce the cost.

The ambient condition of the location and the irradiance seasonal trend show different impact with the demand profile: the high DNI level in winter of Aswan benefit most the CRS plant, whilst a typical industrial load is strongly penalized in Giza, where the irradiance is more in phase with the residential demand. Furthermore, a low irradiance level (like for Giza) leads to an increase in deployment of wind energy and benefits more from the hybrid configuration.

In conclusion, it has been proven that the structure of central receiver system guarantees a low-cost production flexibility mainly thanks to the built-in thermal storage. Moreover, the load-following capability can be further improved with special attention during the design process, which promises greater technological development.

APPENDIX $\mathcal{A}$

Economic optimized configuration of tower solar system

Table A.1: *Geometrical parameters of the CRS configuration for different design power.*

P_{des}	H_t	N_{helio}	dR_2	dR_3	dR_4	k	D_{rec}	H_{rec}	HD	A_{rec}
MW_{th}	m	-	-	-	-	-	m	m	-	m^2
300	160	3197	0.866	1.714	3.000	2.0	11.5	13.8	1.2	498.6
350	180	3709	0.866	1.929	3.000	2.0	13	14.3	1.1	584.0
400	190	4247	0.866	1.850	3.000	2.0	14.5	14.5	1.0	660.5
450	200	4842	0.866	2.067	3.000	2.0	14.5	15.95	1.1	726.6
500	210	5354	0.866	1.633	3.000	2.0	15.5	17.05	1.1	830.2
550	210	5993	0.866	1.633	3.667	2.0	16	17.6	1.1	884.7
600	230	6546	0.866	1.850	3.000	2.0	16	19.2	1.2	965.1
650	230	7114	0.866	1.633	4.000	2.0	17.5	19.25	1.1	1058.3
700	230	7789	0.866	1.633	4.000	2.0	18	19.8	1.1	1119.7
750	240	8420	0.866	1.650	3.000	2.0	18.5	20.35	1.1	1182.7
800	240	9156	0.866	1.650	3.000	2.0	19	20.9	1.1	1247.5
850	270	9486	0.866	1.800	3.000	2.0	20	22	1.1	1382.3
900	260	10211	0.866	1.400	3.500	2.0	20.5	22.55	1.1	1452.3
950	260	10940	0.866	1.400	3.500	2.0	20.5	22.55	1.1	1452.3
1000	270	11641	0.866	1.400	3.000	2.0	20	24	1.2	1508.0

Table A.2: *Performance of the CRS configuration for different design power.*

P_{des}	η_{field}	η_{abs}	$Flux$	$Cost$	A_{land}
MW_{th}	-	-	MW/m^2	$M\$$	km^2
300	0.6224	0.5631	1.099	177.79	2.53
350	0.6251	0.5655	1.095	204.43	3.08
400	0.6230	0.5638	1.086	230.17	3.42
450	0.6137	0.5559	1.068	257.26	3.98
500	0.6171	0.5583	1.078	283.31	3.93
550	0.6050	0.5481	1.092	310.29	4.76
600	0.6043	0.5475	1.065	337.89	5.29
650	0.6027	0.5457	1.092	364.30	5.73
700	0.5916	0.5361	1.082	392.69	6.55
750	0.5866	0.5319	1.073	420.29	6.81
800	0.5747	0.5214	1.076	451.01	7.73
850	0.5901	0.5343	1.099	474.54	6.71
900	0.5798	0.5252	1.064	502.95	7.56
950	0.5696	0.5172	1.088	529.26	8.33
1000	0.5631	0.5116	1.099	559.05	8.63

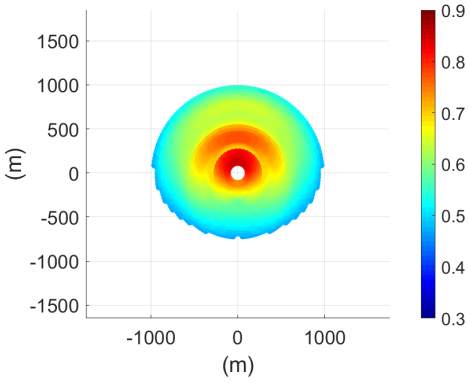

(a) *300* MW_{th}

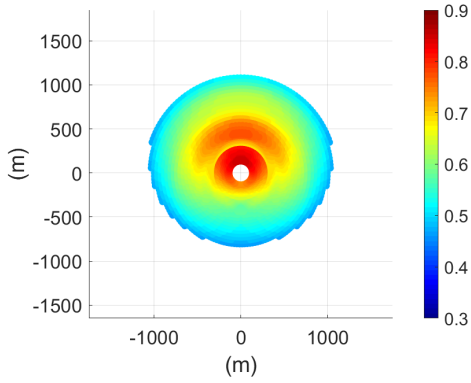

(b) *350* MW_{th}

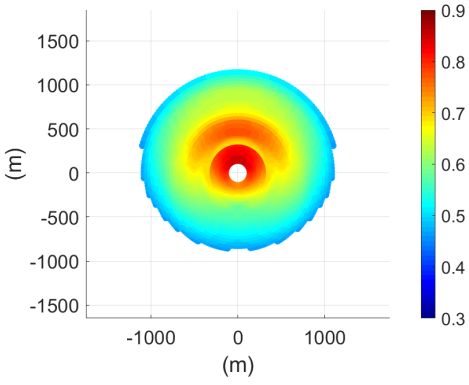

(c) *400* MW_{th}

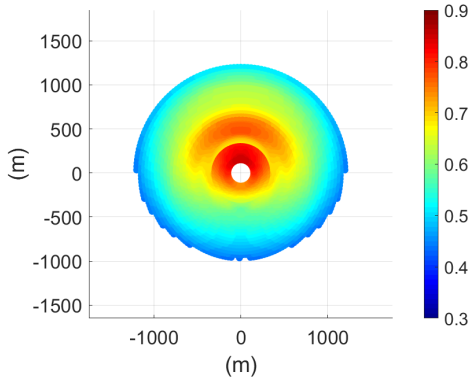

(d) *450* MW_{th}

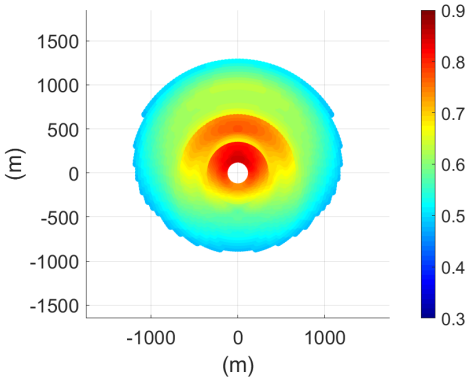

(e) *500* MW_{th}

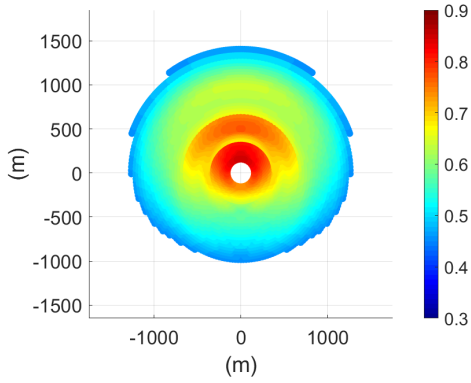

(f) *550* MW_{th}

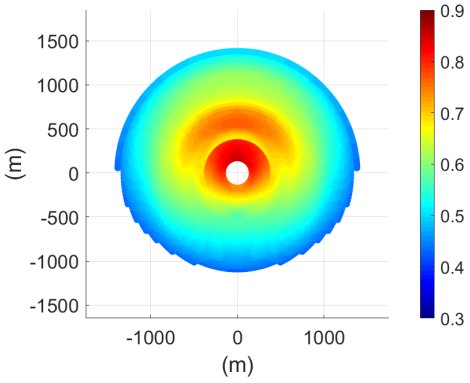

(g) *600* MW_{th}

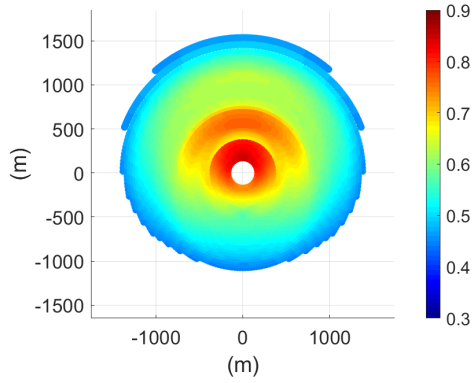

(h) *650* MW_{th}

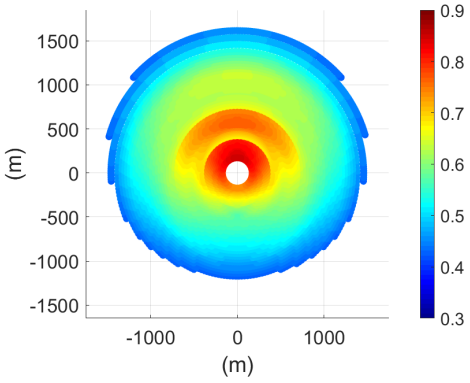

(i) *700* MW_{th}

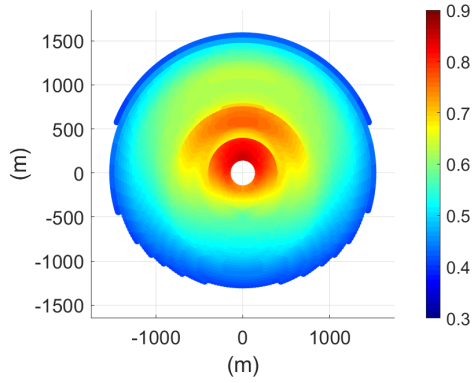

(j) *750* MW_{th}

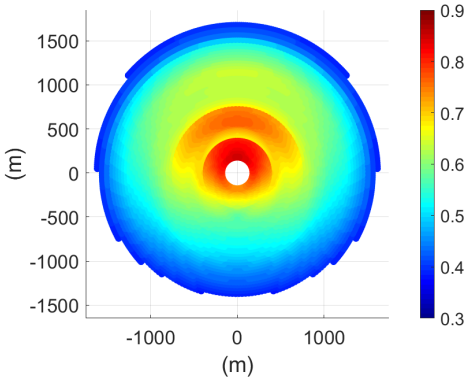

(k) *800* MW_{th}

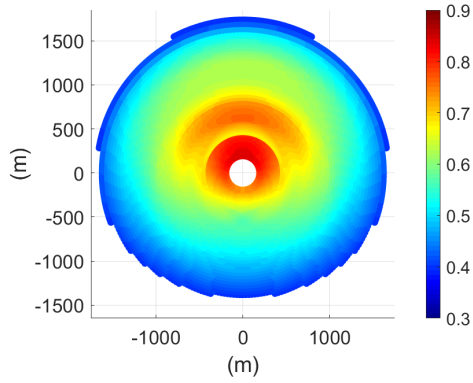

(l) *850* MW_{th}

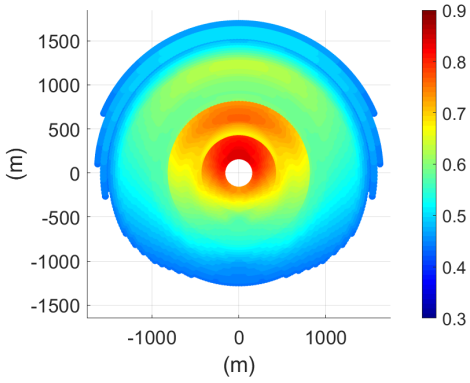

(m) *900* MW_{th}

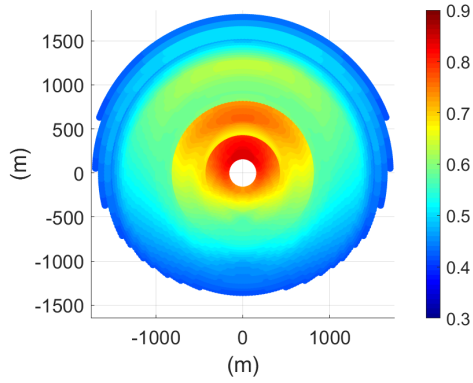

(n) *950* MW_{th}

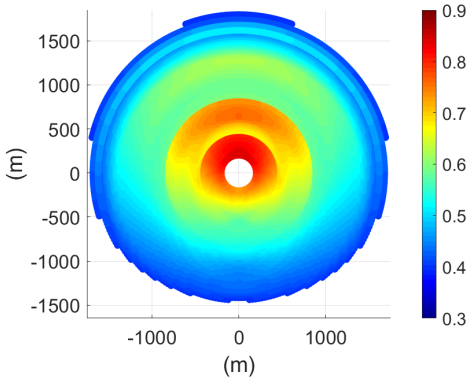

(o) *1000* MW_{th}

Figure A.1: *Optimized layout and design heliostat performance for different design power.*

APPENDIX B

Optimization algorithm with Trnsys

The full-solar/solar hybrid production systems, proposed in chapter 4 and 5, are optimized using the GenOpt® (Generic Optimization Program) software developed by the University of California (Lawrence Berkeley National Laboratory).

The GenOpt software is called by the TrnOpt plug-in for Trnsys software. The process starts, as shown in Figure B.1, from the model developed in Trnsys and modifies to work with the optimization software. The Trnsys file (.dck) has been called and edited by the TrnOpt plug-in that starts numerous annual Trnsys simulation in the aim of asses the best power mix combinations under the constraints and the objective function (i.e. the cost or the LCOE of the system).

The optimization procedure was based on the Particle Swarm algorithm (PSO) coupled with the Hooke and Jeeves algorithm (HJ). This hybrid global optimization algorithm (Fig. B.2) initializes the HJ algorithm using the continuous independent variables of the particle with the lowest function value; the adoption of a double-step optimization improves the identification of local and global optimum solutions.

The parameters involved in the optimization of each production system are specified in respective section with their variation range, that reflect the limits of good operation and design of the plant. The size of the variation (step size) is also predetermined.

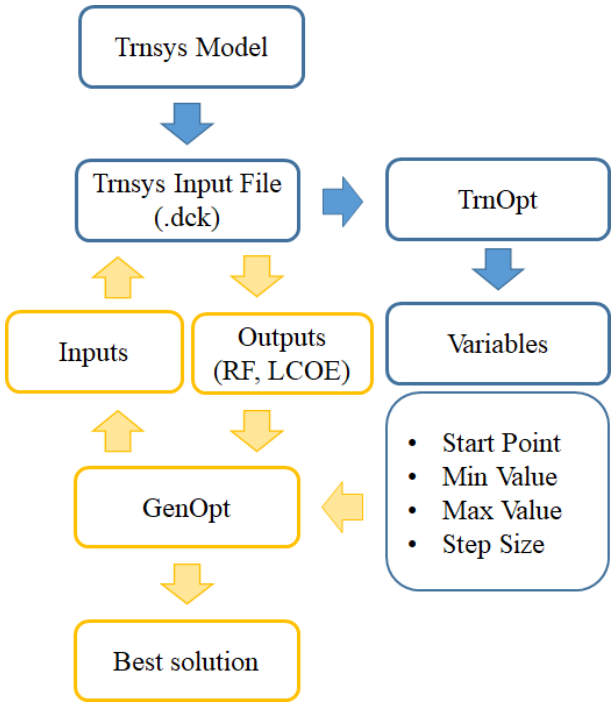

Figure B.1: *Optimization procedure of TrnOpt and GenOpt.*

B.1 Particle swarm optimization algorithm

The particle swarm is a population-based algorithm, presented by Kennedy and Eberhart [187]. A set of particles, that represent the potential solution of the problem, are moved throughout a region. The algorithm randomly generated the initial set and assigns a velocity for each particle, and the objective function is evaluated for the entire population. The velocity and the position of the each particles are updated based on the current velocity and two acceleration, a cognitive and a social component: the first is a function of the particle's best position pbest, and the latter of the best position of nearby particles gbest. When the stopping criteria are reached the iterations are interrupted.

$$v_i(t+1) = m \cdot v_i(t) + c_1 r_1 (pbest_i(t) - x_i(t)) + c_2 r_2 (gbest_i(t) - x_i(t)) \tag{B.1}$$

$$x_i(t+1) = x_i(t) + v_i(t+1) \tag{B.2}$$

B.2 Hooke-Jeeves algorithm

The "Hooke and Jeeves" is a direct search algorithm based on a series of preliminary simulations. Starting from the initial value of the variables, the algorithm explores around the point to determine the best search path (with negative

or positive direction). Ended this preliminary step, repeated for each parameters, the optimization process goes ahead changing the parameters according to the green diagram in figure B.2.

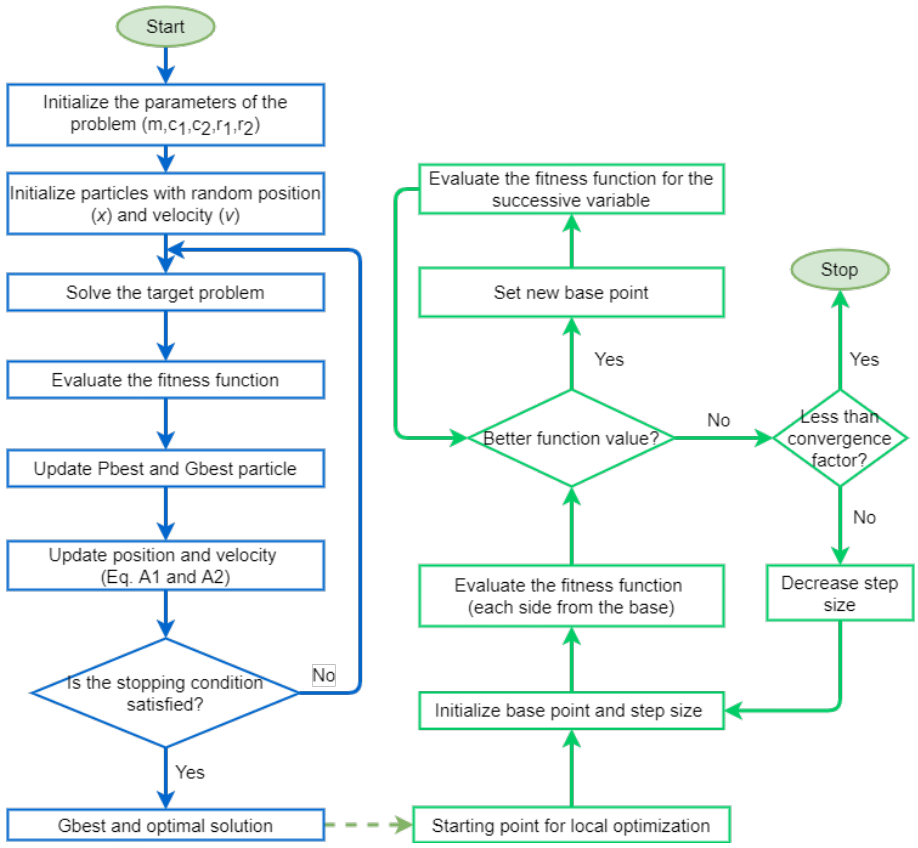

Figure B.2: *Hybrid optimization algorithm flow chart (particle swarm and Hooke-Jeeves, first and second step respectively).*

B.3 Optimization example results

Especially when the variable to maximize are more numerous and different combinations could present similar performance, it is important to determine which are the independent variables.

The Particle Swarm algorithm produce a list of optimal combinations that reach the imposed renewable fraction. The combination of the graphs shows that there are a large number of variables combinations that achieve the RF required with a small spread from the minimum LCOE: in a few hundredths of LCOE variation there are hundreds of valid combinations. The figures B.3 and B.4 show the relationship between the objective functions and some of the optimization variables for two cases (residential and industrial) reported in the

thesis; thanks to the color bar, it is possible to highlight possible interaction between two variables. The thermal nominal power of the solar tower field shows a clearly optimum definition, close to 350 and 550 for the two cases. The steam turbine and PV nominal power (Fig. B.3b and B.3c) present a large cloud of points that suggest a less significant effect on the LCOE; moving to the industrial case, a greater influence of the steam turbine capacity is observed (Fig. B.4b). The battery (Fig. B.3d), even with small capacities, greatly increases the cost of the plant. Finally, also the wind farm does not show any significant benefit to the power mix performance; a possible explanation is linked to the less predictability of the resource which makes the load following management more difficult.

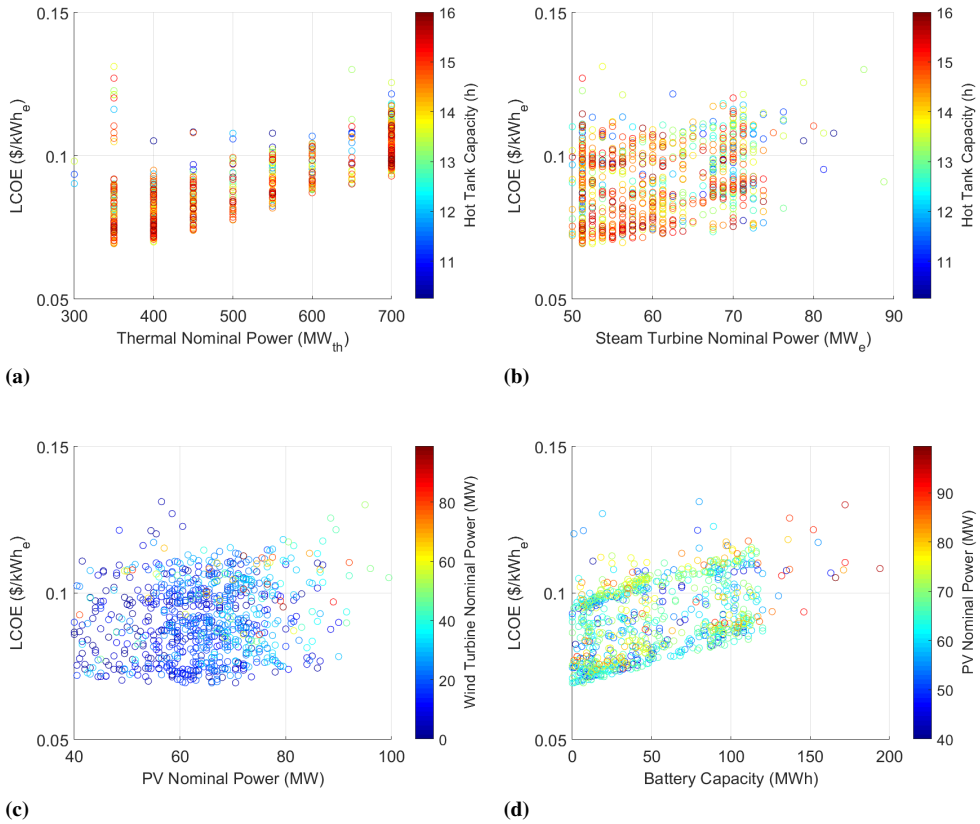

Figure B.3: *Optimization point distribution examples (Residential case)*

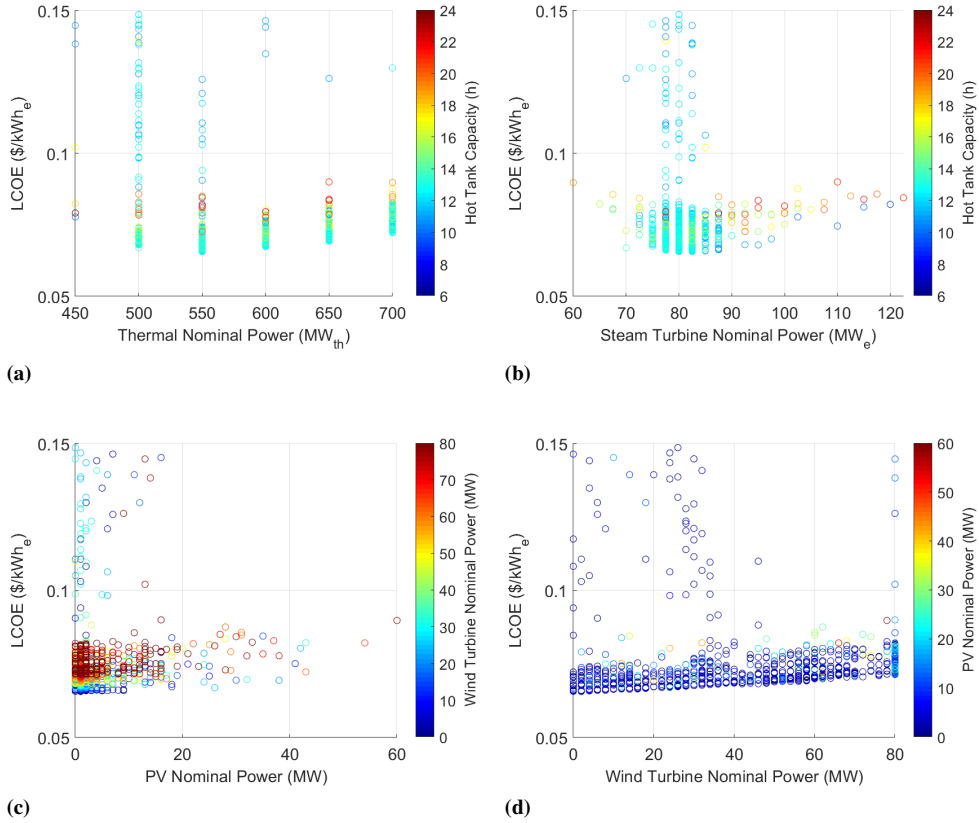

Figure B.4: *Optimization point distribution examples (Industrial case)*

Bibliography

[1] A. Giostri, M. Binotti, C. Sterpos, and G. Lozza, "Small scale solar tower coupled with micro gas turbine," *Renewable Energy*, vol. 147, pp. 570–583, mar 2020.

[2] Lewis S. Nathan, "Research opportunities to advance solar energy utilization," *Science*, vol. 351, no. 6271, pp. aad1920–1–9, 2016.

[3] P. Gauché, J. Rudman, M. Mabaso, W. A. Landman, T. W. von Backström, and A. C. Brent, "System value and progress of CSP," *Solar Energy*, vol. 152, pp. 106–139, 2017.

[4] V. Quaschning, "Technical and economical system comparison of photovoltaic and concentrating solar thermal power systems depending on annual global irradiation," *Solar Energy*, vol. 77, no. 2, pp. 171–178, 2004.

[5] Q. Zhang, Z. Wang, X. Du, G. Yu, and H. Wu, "Dynamic simulation of steam generation system in solar tower power plant," *Renewable Energy*, vol. 135, pp. 866–876, 2019.

[6] EIA, "Levelized Cost and Levelized Avoided Cost of New Generation Resources in the Annual Energy Outlook 2016," pp. 1–21, 2016.

[7] F. Magrassi, E. Rocco, S. Barberis, M. Gallo, and A. Del Borghi, "Hybrid solar power system versus photovoltaic plant: A comparative analysis through a life cycle approach," *Renewable Energy*, vol. 130, pp. 290–304, jan 2019.

[8] I. E. Agency, "Solar Thermal Electricity Plants," tech. rep., 2014.

[9] A. Khaliq, "Energetic and exergetic performance investigation of a solar based integrated system for cogeneration of power and cooling," *Applied Thermal Engineering*, vol. 112, pp. 1305–1316, 2017.

[10] S. Ravelli, G. Franchini, and A. Perdichizzi, "Comparison of different CSP technologies for combined power and cooling production," *Renewable Energy*, vol. 121, pp. 712–721, 2018.

[11] M. Mehos, C. Turchi, J. Vidal, M. J. Wagner, Z. Ma, C. Ho, W. Kolb, C. Andraka, and A. Kruizenga, "Concentrating Solar Power Gen3 Demonstration Roadmap," Tech. Rep. January, 2017.

[12] A. Gilmanova, Z. Wang, A. P. Pachioni, Q. Yu, and G. Yuan, "The role of concentrated solar power in the internet of energy," *AIP Conference Proceedings*, vol. 2126, no. July, 2019.

[13] J. T. Hinkley, J. A. Hayward, B. Curtin, A. Wonhas, R. Boyd, C. Grima, A. Tadros, R. Hall, and K. Naicker, "An analysis of the costs and opportunities for concentrating solar power in Australia," *Renewable Energy*, vol. 57, pp. 653–661, 2013.

[14] G. Brumana, G. Franchini, and E. Ghirardi, "Investigation of the Load-Following Capability of CSP Plants," *Energy Procedia*, vol. 148, pp. 615–622, 2018.

[15] R. Singhai, N. D. Banker, and Harender, "Theoretical Investigation of Aspect Ratio of Heliostat to Minimize Capital Cost of Solar Tower Plant," *Applied Engineering Research*, vol. 13, no. 18, pp. 13652–13659, 2018.

[16] R. Singhai and N. Banker, "Heliostat design for Low Wind Terrain," in *Thermal Engineering: Theory and application*, pp. 2–4, 2019.

[17] IRENA, "Renewable Power Generation Costs in 2017. IRENA - International Renewable Energy Agency," tech. rep., IRENA, 2018.

[18] T. Telsnig, G. Weinrebe, J. Finkbeiner, and L. Eltrop, "Life cycle assessment of a future central receiver solar power plant and autonomous operated heliostat concepts," *Solar Energy*, vol. 157, pp. 187–200, 2017.

[19] M. J. Emes, M. Arjomandi, and G. J. Nathan, "Effect of heliostat design wind speed on the levelised cost of electricity from concentrating solar thermal power tower plants," *Solar Energy*, vol. 115, no. 2015, pp. 441–451, 2015.

[20] X. Wei, Z. Lu, Z. Wang, W. Yu, H. Zhang, and Z. Yao, "A new method for the design of the heliostat field layout for solar tower power plant," *Renewable Energy*, vol. 35, no. 9, pp. 1970–1975, 2010.

[21] J. Barberena, A. Mutuberria Larrayoz, M. Sánchez, and A. Bernardos, "State-of-the-art of Heliostat Field Layout Algorithms and their Comparison," *Energy Procedia*, vol. 93, no. March, pp. 31–38, 2016.

[22] F. Arbes, W. Landman, G. Weinrebe, M. Wöhrbach, D. Gebreiter, J. M. Estebaranz, D. Pereira, and A. Jurado, "Multi tower systems and simulation tools," *SOLARPACES 2018: International Conference on Concentrating Solar Power and Chemical Energy Systems*, vol. 2126, no. July, p. 030004, 2019.

[23] S. Kiwan and A. L. Khammash, "Optical Performance of a Novel Two-Receiver Solar Central Tower System," *Journal of Solar Energy Engineering*, vol. 142, no. 1, pp. 1–13, 2020.

[24] P. Schöttl, T. Zoschke, C. Frantz, Y. Gilon, A. Heimsath, and T. Fluri, "Performance assessment of a secondary concentrator for solar tower external receivers," *SOLARPACES 2018: International Conference on Concentrating Solar Power and Chemical Energy Systems*, vol. 2126, no. July, p. 030052, 2019.

[25] S. Kiwan and S. Al Hamad, "Optimum optical performance of hillside solar central tower systems using spiral distribution," *Journal of Solar Energy Engineering*, vol. 141, no. February, pp. 1–12, 2018.

[26] J. Coventry and J. Pye, "Heliostat cost reduction - Where to now?," *Energy Procedia*, vol. 49, pp. 60–70, 2013.

[27] F. J. Collado and J. Guallar, "Quick design of regular heliostat fields for commercial solar tower power plants," *Energy*, vol. 178, pp. 115–125, 2019.

[28] Q. Yu, Z. Wang, E. Xu, X. Li, and M. Guo, "Modeling and dynamic simulation of the collector and receiver system of 1MWe DAHAN solar thermal power tower plant," *Renewable Energy*, vol. 43, pp. 18–29, jul 2012.

[29] M. Saghafifar and M. Gadalla, "Improvement in Spiral Heliostat Field Layout Thermo-Economic Performance by Field Zoning Implementation," in *ASME 2016 10th International Conference on energy sustainability*, ASME, jun 2016.

[30] O. Farges, J. J. Bézian, and M. El Hafi, "Global optimization of solar power tower systems using a Monte Carlo algorithm: Application to a redesign of the PS10 solar thermal power plant," *Renewable Energy*, vol. 119, pp. 345–353, 2018.

[31] G. Srilakshmi, N. S. Suresh, N. C. Thirumalai, and M. A. Ramaswamy, "Preliminary design of heliostat field and performance analysis of solar tower plants with thermal storage and hybridisation," *Sustainable Energy Technologies and Assessments*, vol. 19, pp. 102–113, 2017.

[32] E. Carrizosa, C. Domínguez-Bravo, E. Fernández-Cara, and M. Quero, "Optimization of multiple receivers solar power tower systems," *Energy*, vol. 90, pp. 2085–2093, 2015.

[33] F. J. Collado and J. Guallar, "Two-stages optimised design of the collector field of solar power tower plants," *Solar Energy*, vol. 135, pp. 884–896, 2016.

[34] A. Ramos and F. Ramos, "Strategies in tower solar power plant optimization," *Solar Energy*, vol. 86, no. 9, pp. 2536–2548, 2012.

[35] W. Cole and A. W. Frazier, "Impacts of increasing penetration of renewable energy on the operation of the power sector," *The Electricity Journal*, vol. 31, pp. 24–31, dec 2018.

[36] K. E. Okedu and W. Z. A. L. Salmani, "Smart Grid Technologies in Gulf Cooperation Council Countries: Challenges and Opportunities," vol. 3, no. June, 2019.

[37] IRENA, *Electricity storage and renewables: Costs and markets to 2030*. No. October, 2017.

[38] I. E. Agency and Iea, "Technology Roadmap: Solar Photovoltaic Energy," *SpringerReference*, 2014.

[39] R. Chen, Z. Rao, and S. Liao, "Determination of key parameters for sizing the heliostat field and thermal energy storage in solar tower power plants," *Energy Conversion and Management*, vol. 177, no. October, pp. 385–394, 2018.

[40] Y. Luo, T. Lu, and X. Du, "Novel optimization design strategy for solar power tower plants," *Energy Conversion and Management*, vol. 177, pp. 682–692, dec 2018.

[41] A. B. Awan, M. Zubair, and K. V. Chandra Mouli, "Design, optimization and performance comparison of solar tower and photovoltaic power plants," *Energy*, vol. 199, p. 117450, 2020.

[42] A. Khosravi, S. Syri, M. Assad, and M. Malekan, "Thermodynamic and economic analysis of a hybrid ocean thermal energy conversion/photovoltaic system with hydrogen-based energy storage system," *Energy*, vol. 172, pp. 304–319, apr 2019.

[43] M. J. Wagner, W. T. Hamilton, A. Newman, J. Dent, C. Diep, and R. Braun, "Optimizing dispatch for a concentrated solar power tower," *Solar Energy*, vol. 174, no. June, pp. 1198–1211, 2018.

[44] M. Ramesh and R. P. Saini, "Dispatch strategies based performance analysis of a hybrid renewable energy system for a remote rural area in India," *Journal of Cleaner Production*, vol. 259, p. 120697, 2020.

[45] P. O. Oviroh and T. C. Jen, "The energy cost analysis of hybrid systems and diesel generators in powering selected base transceiver station locations in Nigeria," *Energies*, vol. 11, no. 3, pp. 7–9, 2018.

[46] The Red Sea Development Company, "The Red Sea - Smart and Sustainable," 2019.

[47] M. Saghafifar, M. Gadalla, and K. Mohammadi, "Thermo-economic analysis and optimization of heliostat fields using AINEH code: Analysis of implementation of non-equal heliostats (AINEH)," *Renewable Energy*, vol. 135, pp. 920–935, 2019.

[48] E. Carrizosa, C.-A. Domínguez-Bravo, E. Fernández-Cara, and M. Quero, "An optimization tool to design the field of a solar power tower plant allowing heliostats of different sizes," *International Journal of Energy Research*, vol. 41, pp. 1096–1107, jun 2017.

[49] S. L. Lutchman, P. Gauché, and A. Groenwold, "On Selecting a Method for Heliostat Field Layout Optimization." 2014.

[50] I. Les, A. Mutuberria, P. Schöttl, P. Nitz, E. Leonardi, and L. Pisani, "Optical performance comparison between heliostat field generation algorithms," *AIP Conference Proceedings*, vol. 2033, no. November, 2018.

[51] F. J. Collado and J. Guallar, "Campo: Generation of regular heliostat fields," *Renewable Energy*, vol. 46, pp. 49–59, 2012.

[52] E. Carrizosa, C. A. Domínguez-Bravo, E. Fernández-Cara, and M. Quero, "A heuristic method for simultaneous tower and pattern-free field optimization on solar power systems," *Computers and Operations Research*, vol. 57, pp. 109–122, 2015.

[53] S. Kim, I. Lee, and B. J. Lee, "Development of performance analysis model for central receiver system and its application to pattern-free heliostat layout optimization," *Solar Energy*, vol. 153, pp. 499–507, 2017.

[54] S. M. Besarati, D. Yogi Goswami, and E. K. Stefanakos, "Optimal heliostat aiming strategy for uniform distribution of heat flux on the receiver of a solar power tower plant," *Energy Conversion and Management*, vol. 84, pp. 234–243, 2014.

[55] P. Garcia, A. Ferriere, and J. J. Bezian, "Codes for solar flux calculation dedicated to central receiver system applications: A comparative review," *Solar Energy*, vol. 82, no. 3, pp. 189–197, 2008.

[56] W. Huang and L. Yu, "Development of a new flux density function for a focusing heliostat," *Energy*, vol. 151, pp. 358–375, 2018.

[57] A. Sánchez-González and D. Santana, "Solar flux distribution on central receivers: A projection method from analytic function," *Renewable Energy*, vol. 74, pp. 576–587, 2015.

[58] N. C. Cruz, J. L. Redondo, M. Berenguel, J. D. Álvarez, and P. M. Ortigosa, "Review of software for optical analyzing and optimizing heliostat fields," *Renewable and Sustainable Energy Reviews*, vol. 72, no. May 2016, pp. 1001–1018, 2017.

[59] A. Ramos and F. Ramos, "Heliostat blocking and shadowing efficiency in the video-game era." 2014.

[60] N. C. Cruz, R. Ferri-García, J. D. Álvarez, J. L. Redondo, J. Fernández-Reche, M. Berenguel, R. Monterreal, and P. M. Ortigosa, "On building-up a yearly characterization of a heliostat field: A new methodology and an application example," *Solar Energy*, vol. 173, no. June, pp. 578–589, 2018.

[61] F. W. Lipps and L. L. Vant-Hull, "A cellwise method for the optimization of large central receiver systems," *Solar Energy*, vol. 20, no. 6, pp. 505–516, 1978.

[62] B. L. Kistler, "A User's Manual for DELSOL3: A Computer Code for Calculating the Optical Performance and Optimal System Design for Solar Thermal Central Receiver Plants.," tech. rep., 1986.

[63] M. Atif and F. A. Al-Sulaiman, "Optimization of heliostat field layout in solar central receiver systems on annual basis using differential evolution algorithm," *Energy Conversion and Management*, vol. 95, pp. 1–9, 2015.

[64] F. J. Collado and J. Guallar, "A review of optimized design layouts for solar power tower plants with campo code," *Renewable and Sustainable Energy Reviews*, vol. 20, pp. 142–154, apr 2013.

[65] G. Sassi, "Some notes on shadow and blockage effects," *Solar Energy*, vol. 31, no. 3, pp. 331–333, 1983.

[66] W. Huang, L. Li, Y. Li, and Z. Han, "Development and evaluation of several models for precise and fast calculations of shading and blocking in heliostats field," *Solar Energy*, vol. 95, pp. 255–264, 2013.

[67] J. Wang, L. Duan, Y. Yang, and L. Yang, "Rapid design of a heliostat field by analytic geometry methods and evaluation of maximum optical efficiency map," *Solar Energy*, vol. 180, no. August 2018, pp. 456–467, 2019.

[68] F. Eddhibi, M. Ben Amara, M. Balghouthi, and A. Guizani, "Design and analysis of a heliostat field layout with reduced shading effect in southern Tunisia," *International Journal of Hydrogen Energy*, vol. 42, pp. 28973–28996, nov 2017.

[69] J. Polo, J. Alonso-Montesinos, G. López-Rodriguez, J. Ballestrín, J. L. Bosch, J. Barbero, E. Carra, J. Fernández-Reche, and F. J. Batlles, "Modelling atmospheric attenuation at different AOD time-scales in yield performance of solar tower plants," *AIP Conference Proceedings*, vol. 2033, no. November, 2018.

[70] M. Gadalla and M. Saghafifar, "Thermo-economic and comparative analyses of two recently proposed optimization approaches for circular heliostat fields: Campo radial-staggered and biomimetic spiral," *Solar Energy*, vol. 136, pp. 197–209, 2016.

[71] F. J. Collado and J. Guallar, "Fast and reliable flux map on cylindrical receivers," *Solar Energy*, vol. 169, no. February, pp. 556–564, 2018.

[72] F. J. Collado, A. Gómez, and J. A. Turégano, "An analytic function for the flux density due to sunlight reflected from a heliostat," *Solar Energy*, vol. 37, no. 3, pp. 215–234, 1986.

[73] P. Schwarzbözl, M. Schmitz, and R. Pitz-Paal, "Visual HFLCAL - A software tool for layout and optimisation of heliostat fields," *SolarPACES Conference*, 2009.

[74] W. Huang, L. Yu, and P. Hu, "An analytical solution for the solar flux density produced by a round focusing heliostat," *Renewable Energy*, vol. 134, pp. 306–320, 2019.

[75] M. J. Wagner and T. Wendelin, "SolarPILOT: A power tower solar field layout and characterization tool," *Solar Energy*, vol. 171, no. June, pp. 185–196, 2018.

[76] F. J. Collado, "One-point fitting of the flux density produced by a heliostat," *Solar Energy*, vol. 84, no. 4, pp. 673–684, 2010.

[77] C. Li, R. Zhai, H. Liu, Y. Yang, and H. Wu, "Optimization of a heliostat field layout using hybrid PSO-GA algorithm," *Applied Thermal Engineering*, vol. 128, pp. 33–41, 2018.

[78] K. Chong, C. Lim, and C. Hiew, "Cost-effective solar furnace system using fixed geometry Non-Imaging Focusing Heliostat and secondary parabolic concentrator," *Renewable Energy*, vol. 36, pp. 1595–1602, may 2011.

[79] J. Ballestrín and A. Marzo, "Solar radiation attenuation in solar tower plants," *Solar Energy*, vol. 86, no. 1, pp. 388–392, 2012.

[80] M. Zhang, L. Yang, C. Xu, and X. Du, "An efficient code to optimize the heliostat field and comparisons between the biomimetic spiral and staggered layout," *Renewable Energy*, vol. 87, pp. 720–730, 2016.

[81] M. Astolfi, M. Binotti, S. Mazzola, L. Zanellato, and G. Manzolini, "Heliostat aiming point optimization for external tower receiver," *Solar Energy*, vol. 157, pp. 1114–1129, 2017.

[82] A. Boretti, S. Castelletto, and S. Al-Zubaidy, "Concentrating solar power tower technology: present status and outlook," *Nonlinear Engineering*, vol. 8, no. 1, pp. 10–31, 2018.

[83] A. Sánchez-González, C. Caliot, A. Ferrière, and D. Santana, "Determination of heliostat canting errors via deterministic optimization," *Solar Energy*, vol. 150, pp. 136–146, 2017.

[84] A. Sánchez-González, M. R. Rodríguez-Sánchez, and D. Santana, "Aiming factor to flatten the flux distribution on cylindrical receivers," *Energy*, vol. 153, no. June, pp. 113–125, 2018.

[85] M. J. Wagner, *Simulation and Predictive Performance Modeling of Utility-Scale Central Receiver System Power Plants*. PhD thesis, 2008.

[86] J. Wang, L. Duan, and Y. Yang, "An improvement crossover operation method in genetic algorithm and spatial optimization of heliostat field," *Energy*, vol. 155, pp. 15–28, 2018.

[87] A. Steinfeld and M. Schubnell, "Optimum aperture size and operating temperature of a solar cavity-receiver," *Solar Energy*, vol. 50, no. 1, pp. 19–25, 1993.

[88] Z. Yao, Z. Wang, Z. Lu, and X. Wei, "Modeling and simulation of the pioneer 1MW solar thermal central receiver system in China," *Renewable Energy*, vol. 34, pp. 2437–2446, nov 2009.

[89] S. S. Mostafavi Tehrani and R. A. Taylor, "Off-design simulation and performance of molten salt cavity receivers in solar tower plants under realistic operational modes and control strategies," *Applied Energy*, vol. 179, pp. 698–715, oct 2016.

[90] X. Li, W. Kong, Z. Wang, C. Chang, and F. Bai, "Thermal model and thermodynamic performance of molten salt cavity receiver," *Renewable Energy*, vol. 35, pp. 981–988, may 2010.

[91] F. Rinaldi, M. Binotti, A. Giostri, and G. Manzolini, "Comparison of linear and point focus collectors in solar power plants," in *Energy Procedia*, 2014.

[92] J. Lilliestam and R. Pitz-Paal, "Concentrating solar power for less than USD 0.07 per kWh: finally the breakthrough?," *Renewable Energy Focus*, 2018.

[93] P. Schöttl, S. Rohani, E. Leonardi, L. Pisani, I. Les, A. Mutuberria, and P. Nitz, "Solar field heliostat selection based on polygon optimization and boundaries," *AIP Conference Proceedings*, vol. 2126, no. July, p. 030053, 2019.

[94] E. Leonardi, L. Pisani, I. Les, A. M. Larrayoz, S. Rohani, and P. Schöttl, "Techno-economic heliostat field optimization: Comparative analysis of different layouts," *Solar Energy*, vol. 180, no. December 2018, pp. 601–607, 2019.

[95] S. Kiwan and S. Al Hamad, "On Analyzing the Optical Performance of Solar Central Tower Systems on Hillsides Using Biomimetic Spiral Distribution," *Journal of Solar Energy Engineering*, vol. 141, p. 011010, sep 2019.

[96] N. C. Cruz, S. Salhi, J. L. Redondo, J. D. Álvarez, M. Berenguel, and P. M. Ortigosa, "Design of a parallel genetic algorithm for continuous and pattern-free heliostat field optimization," *Journal of Supercomputing*, vol. 75, no. 3, pp. 1–16, 2018.

[97] M. Saghafifar and M. Gadalla, "Selecting a proper design period for heliostat field layout optimization using Campo code," in *Next Generation Technologies for Solar Energy Conversion VII*, vol. 9937, p. 99370V, 2016.

[98] P. Talebizadeh, M. A. Mehrabian, and H. Rahimzadeh, "Optimization of Heliostat Layout in Central Receiver Solar Power Plants," *Journal of Energy Engineering*, vol. 140, p. 04014005, dec 2014.

[99] A. Poullikkas, C. Rouvas, I. Hadjipaschalis, and G. Kourtis, "Optimum sizing of steam turbines for concentrated solar power plants," *International Journal of Energy and Environment*, vol. 3, no. 1, pp. 9–18, 2012.

[100] RES4MED, "RES4MED Country profile: Egypt," 2015.

[101] J. Remund, S. Müller, S. Kunz, and C. Schilter, *Meteonorm Handbook part II: Theory*. No. May, 2012.

[102] A. Pfahl, J. Coventry, M. Röger, F. Wolfertstetter, J. F. Vásquez-Arango, F. Gross, M. Arjomandi, P. Schwarzbözl, M. Geiger, and P. Liedke, "Progress in heliostat development," *Solar Energy*, vol. 152, pp. 3–37, 2017.

[103] C. S. Turchi and G. A. Heath, "Molten Salt Power Tower Cost Model for the System Advisor Model (SAM)," no. February, 2013.

[104] G. Augsburger and D. Favrat, "Modelling of the receiver transient flux distribution due to cloud passages on a solar tower thermal power plant," *Solar Energy*, vol. 87, pp. 42–52, 2013.

[105] M. Gadalla and M. Saghafifar, "A concise overview of heliostat fields-solar thermal collectors: Current state of art and future perspective," *International Journal of Energy Research*, vol. 42, no. 10, pp. 3145–3163, 2018.

[106] F. Arbes, M. Wöhrbach, D. Gebreiter, and G. Weinrebe, "Towards high efficiency heliostat fields," *AIP Conference Proceedings*, vol. 1850, 2017.

[107] M. Balz, V. Göcke, T. Keck, F. Von Reeken, G. Weinrebe, and M. Wöhrbach, "Stellio - Development, construction and testing of a smart heliostat," *AIP Conference Proceedings*, vol. 1734, 2016.

[108] J. B. Blackmon, "Parametric determination of heliostat minimum cost per unit area," *Solar Energy*, vol. 97, pp. 342–349, 2013.

[109] J. Coventry, M. Arjomandi, J. Barry, M. Blanco, G. Burgess, J. Campbell, P. Connor, M. Emes, P. Fairman, D. Farrant, F. Ghanadi, V. Grigoriev, C. Hall, P. Koltun, D. Lewis, S. Martin, G. Nathan, J. Pye, A. Qiu, W. Stuart, Y. Tang, F. Venn, and J. Yu, "Development of the ASTRI heliostat," *AIP Conference Proceedings*, vol. 1734, no. May, 2016.

[110] A. Pidaparthi and J. Hoffmann, "Effect of heliostat size on the levelized cost of electricity for power towers," in *AIP Conference Proceedings*, vol. 1850, 2017.

[111] P. K. Falcone, *A handbook for solar central receiver design*. 1986.

[112] A. Hassan, "Solar tower power plant optimization : a review," Tech. Rep. November, 2016.

[113] M. R. Rodríguez-Sánchez, A. Sánchez-González, and D. Santana, "Feasibility study of a new concept of solar external receiver: Variable velocity receiver," *Applied Thermal Engineering*, vol. 128, pp. 335–344, 2018.

[114] W.-Q. Wang, Y. Qiu, M.-J. Li, F. Cao, and Z.-B. Liu, "Optical efficiency improvement of solar power tower by employing and optimizing novel fin-like receivers," *Energy Conversion and Management*, vol. 184, pp. 219–234, mar 2019.

[115] A. Fleming, C. Folsom, H. Ban, and Z. Ma, "A general method to analyze the thermal performance of multi-cavity concentrating solar power receivers," *Solar Energy*, vol. 150, pp. 608–618, 2017.

[116] V. Venkatesh, B. S. Rao, G. Srilakshmi, N. C. Thirumalai, and M. A. Ramaswamy, "Correlation between central receiver size and solar field using flat heliostats," *Applied Solar Energy*, vol. 53, no. 3, pp. 258–266, 2017.

[117] R. Flesch, C. Frantz, D. Maldonado Quinto, and P. Schwarzbözl, "Towards an optimal aiming for molten salt power towers," *Solar Energy*, vol. 155, pp. 1273–1281, 2017.

[118] C. Gertig, A. Delgado, C. Hidalgo, and R. Ron, "SoFiA - A novel simulation tool for Central Receiver Systems," *Energy Procedia*, vol. 49, pp. 1361–1370, 2013.

[119] Y.-L. He, K. Wang, Y. Qiu, B.-C. Du, Q. Liang, and S. Du, "Review of the solar flux distribution in concentrated solar power: non-uniform features, challenges, and solutions," *Applied Thermal Engineering*, vol. 149, no. October 2018, pp. 448–474, 2019.

[120] T. Ashley, E. Carrizosa, and E. Fernández-Cara, "Optimisation of aiming strategies in Solar Power Tower plants," *Energy*, vol. 137, no. November, pp. 285–291, 2017.

[121] J. Servert, A. González, J. Gil, D. López, J. F. Funes, and A. Jurado, "Sensitivity analysis of heliostat aiming strategies and receiver size on annual thermal production of a molten salt external receiver," in *AIP Conference Proceedings*, vol. 030047, p. 030047, 2017.

[122] F. J. Collado and J. Guallar, "A two-parameter aiming strategy to reduce and flatten the flux map in solar power tower plants," *Solar Energy*, 2019.

[123] D. Cocco, L. Migliari, and M. Petrollese, "A hybrid CSP-CPV system for improving the dispatchability of solar power plants," *Energy Conversion and Management*, vol. 114, pp. 312–323, 2016.

[124] F. Abdelrahim, "The Rise of Renewable Energy in the MENA Region : An Investigation into the Policies Governing Energy Resources," 2019.

[125] U. Desideri, F. Zepparelli, V. Morettini, and E. Garroni, "Comparative analysis of concentrating solar power and photovoltaic technologies: Technical and environmental evaluations," *Applied Energy*, vol. 102, pp. 765–784, 2013.

[126] M. M. Roni, I. U. Hoque, and T. Ahmed, "Comparative Study of Levelized Cost of Electricity (LCOE) for Concentrating Solar Power (CSP) and Photovoltaic (PV) Plant in the Southeastern Region of Bangladesh," *2nd International Conference on Electrical, Computer and Communication Engineering, ECCE 2019*, pp. 1–6, 2019.

[127] J. Servert, E. Cerrajero, F. J. Comas, A. R. Rocha, J. M. Estebaranz, R. Durán, E. Stavropoulou, M. Kourasi, P. Markopoulos, A. Dimeas, and A. Vaiani, "Smart renewable hubs: Multi-hybridization to achieve high RE penetration in a grid-friendly manner," *AIP Conference Proceedings*, vol. 2033, no. November, 2018.

[128] P. Palenzuela and D. C. Alarcón-Padilla, "Concentrating Solar Power and Desalination Plants," pp. 327–340, 2019.

[129] M. Mahlooji, L. Gaudard, B. Ristic, and K. Madani, "The importance of considering resource availability restrictions in energy planning: What is the footprint of electricity generation in the Middle East and North Africa (MENA)?," *Science of The Total Environment*, p. 135035, nov 2019.

[130] R. Guédez, J. Spelling, and B. Laumert, "Thermoeconomic optimization of solar thermal power plants with storage in high-penetration renewable electricity markets," *Energy Procedia*, vol. 57, no. 0, pp. 541–550, 2014.

[131] U. Herrmann, B. Kelly, and H. Price, "Two-tank molten salt storage for parabolic trough solar power plants," *Energy*, vol. 29, no. 5-6, pp. 883–893, 2004.

[132] D. Kearney, U. Herrmann, P. Nava, B. Kelly, R. Mahoney, J. Pacheco, R. Cable, N. Potrovitza, D. Blake, and H. Price, "Assessment of a Molten Salt Heat Transfer Fluid in a Parabolic Trough Solar Field," *Journal of Solar Energy Engineering*, vol. 125, no. 2, p. 170, 2003.

[133] C. K. Ho, "Advances in central receivers for concentrating solar applications," *Solar Energy*, vol. 152, pp. 38–56, 2017.

[134] O. Ogunmodimu and E. C. Okoroigwe, "Concentrating solar power technologies for solar thermal grid electricity in Nigeria: A review," *Renewable and Sustainable Energy Reviews*, vol. 90, pp. 104–119, jul 2018.

[135] G. Iaquaniello, W. Montanari, and A. Salladini, "Standalone CSP-DG system for electrification of remote areas and desalinated water supply," *Solar Energy*, vol. 157, no. April, pp. 1056–1063, 2017.

[136] A. Rovira, C. Sánchez, M. Valdés, R. Abbas, R. Barbero, M. J. Montes, M. Muñoz, J. Muñoz-Antón, G. Ortega, and F. Varela, "Comparison of different technologies for integrated solar combined cycles: Analysis of concentrating technology and solar integration," *Energies*, vol. 11, no. 5, 2018.

[137] A. Al Zahrani, A. Bindayel, A. Al Rished, A. Perdichizzi, G. Franchini, and S. Ravelli, "Comparative analysis of Different CSP plant configurations in Saudi Arabia," *2016 Saudi Arabia Smart Grid Conference, SASG 2016*, pp. 1–7, 2017.

[138] M. Shepero, D. van der Meer, J. Munkhammar, and J. Widén, "Residential probabilistic load forecasting: A method using Gaussian process designed for electric load data," *Applied Energy*, vol. 218, no. January, pp. 159–172, 2018.

[139] M. J. Wagner, A. M. Newman, W. T. Hamilton, and R. J. Braun, "Optimized dispatch in a first-principles concentrating solar power production model," *Applied Energy*, vol. 203, pp. 959–971, 2017.

[140] A. Grandjean, J. Adnot, and G. Binet, "A review and an analysis of the residential electric load curve models," *Renewable and Sustainable Energy Reviews*, vol. 16, no. 9, pp. 6539–6565, 2012.

[141] A. Vaghefi, F. Farzan, and M. A. Jafari, "Modeling industrial loads in non-residential buildings," *Applied Energy*, vol. 158, pp. 378–389, 2015.

[142] H. Price, D. Kearney, F. Redell, R. Charles, and F. Morse, "Dispatchable solar power plant," vol. 040032, p. 040032, 2018.

[143] A. Perdichizzi, G. Barigozzi, G. Franchini, and S. Ravelli, "Peak shaving strategy through a solar combined cooling and power system in remote hot climate areas," *Applied Energy*, vol. 143, pp. 154–163, 2015.

[144] A. Van Deventer, "South African power system status overview," *64th AMEU Convention 2014*, no. October, pp. 87–89, 2014.

[145] G. Franchini, A. Perdichizzi, and S. Ravelli, "Performance prediction of solarized CC power plants operating in a load-following strategy," in *Power-Gen Africa 2016*, (Johannesburg, South Africa), pp. 1–12, 2016.

[146] F. Lippke, "Simulation of the part-load behaviour of a 30 MW SEGS plant Frank Lippke," tech. rep., Sandia National Laboratories, 1995.

[147] T. A. Moss and D. A. Brosseau, "Final test results for the Schott HCE on a LS-2 collector.," Tech. Rep. July, 2005.

[148] J. García-Barberena, A. Mutuberria, L. G. Palacin, J. L. Sanz, D. Pereira, A. Bernardos, M. Sanchez, and A. R. Rocha, "Coupled optical and thermal detailed simulations for the accurate evaluation and performance improvement of molten salts solar towers," *AIP Conference Proceedings*, vol. 1850, 2017.

[149] R. Poudineh, A. Sen, and B. Fattouh, "Advancing renewable energy in resource-rich economies of the MENA," *Renewable Energy*, vol. 123, pp. 135–149, aug 2018.

[150] Z. Said, A. A. Alshehhi, and A. Mehmood, "Predictions of UAE's renewable energy mix in 2030," *Renewable Energy*, 2018.

[151] S. Timmerberg, A. Sanna, M. Kaltschmitt, and M. Finkbeiner, "Renewable electricity targets in selected MENA countries – Assessment of available resources, generation costs and GHG emissions," *Energy Reports*, 2019.

[152] IRENA, *Renewable Energy Outlook: Egypt*. 2018.

[153] Renewable Energy Agency International IRENA, *Renewable Energy Market Analysis: GCC 2019*. 2019.

[154] J. Haas, F. Cebulla, W. Nowak, C. Rahmann, and R. Palma-Behnke, "A multi-service approach for planning the optimal mix of energy storage technologies in a fully-renewable power supply," *Energy Conversion and Management*, vol. 178, no. September, pp. 355–368, 2018.

[155] D. Heide, L. von Bremen, M. Greiner, C. Hoffmann, M. Speckmann, and S. Bofinger, "Seasonal optimal mix of wind and solar power in a future, highly renewable Europe," *Renewable Energy*, vol. 35, pp. 2483–2489, nov 2010.

[156] M. Á. Lynch, R. S. Tol, and M. J. O'Malley, "Optimal interconnection and renewable targets for north-west Europe," *Energy Policy*, vol. 51, pp. 605–617, dec 2012.

[157] M. G. Rasmussen, G. B. Andresen, and M. Greiner, "Storage and balancing synergies in a fully or highly renewable pan-European power system," *Energy Policy*, vol. 51, pp. 642–651, dec 2012.

[158] N. Sezer and M. Koç, "Development and performance assessment of a new integrated solar, wind, and osmotic power system for multigeneration, based on thermodynamic principles," *Energy Conversion and Management*, vol. 188, no. January, pp. 94–111, 2019.

[159] K. Murugaperumal, S. Srinivasn, and G. R. Satya Prasad, "Optimum design of hybrid renewable energy system through load forecasting and different operating strategies for rural electrification," *Sustainable Energy Technologies and Assessments*, vol. 37, no. November 2018, p. 100613, 2020.

[160] F. J. de Sisternes, J. D. Jenkins, and A. Botterud, "The value of energy storage in decarbonizing the electricity sector," *Applied Energy*, vol. 175, pp. 368–379, 2016.

[161] M. D. Leonard, E. E. Michaelides, and D. N. Michaelides, "Energy storage needs for the substitution of fossil fuel power plants with renewables," *Renewable Energy*, vol. 145, pp. 951–962, jan 2020.

[162] N. Ghorbani, A. Kasaeian, A. Toopshekan, L. Bahrami, and A. Maghami, "Optimizing a hybrid wind-PV-battery system using GA-PSO and MOPSO for reducing cost and increasing reliability," *Energy*, vol. 154, pp. 581–591, jul 2018.

[163] J. F. Servert, D. López, E. Cerrajero, A. R. Rocha, D. Pereira, and L. Gonzalez, "Solar hybrid power plants: Solar energy contribution in reaching full dispatchability and firmness," *AIP Conference Proceedings*, vol. 1734, no. May 2016, 2016.

[164] X. Ju, C. Xu, Y. Hu, X. Han, G. Wei, and X. Du, "A review on the development of photovoltaic/concentrated solar power (PV-CSP) hybrid systems," *Solar Energy Materials and Solar Cells*, vol. 161, pp. 305–327, mar 2017.

[165] O. A. Zaalouk, *Identifying opportunities for developing CSP and PV-CSP hybrid projects under current tender conditions and market perspectives in MENA – benchmarking with PV-CCGT*. PhD thesis, 2016.

[166] Bizon and Thounthong, "Energy Efficiency and Fuel Economy of a Fuel Cell/Renewable Energy Sources Hybrid Power System with the Load-Following Control of the Fueling Regulators," *Mathematics*, vol. 8, p. 151, jan 2020.

[167] H. Liu, R. Zhai, J. Fu, Y. Wang, and Y. Yang, "Optimization study of thermal-storage PV-CSP integrated system based on GA-PSO algorithm," *Solar Energy*, vol. 184, pp. 391–409, may 2019.

[168] R. Zhai, H. Liu, Y. Chen, H. Wu, and Y. Yang, "The daily and annual technical-economic analysis of the thermal storage PV-CSP system in two dispatch strategies," *Energy Conversion and Management*, vol. 154, pp. 56–67, dec 2017.

[169] M. o. E. &. R. Energy, "Summary for Policymakers," in *Climate Change 2013 - The Physical Science Basis* (Intergovernmental Panel on Climate Change, ed.), vol. 53, pp. 1–30, Cambridge: Cambridge University Press, 2018.

[170] M. Pierro, M. De Felice, E. Maggioni, D. Moser, A. Perotto, F. Spada, and C. Cornaro, "Residual load probabilistic forecast for reserve assessment: A real case study," *Renewable Energy*, vol. 149, pp. 508–522, 2020.

[171] Tesla, "Tesla Powerpack Datasheet," 2020.

[172] A. Zurita, C. Mata-Torres, C. Valenzuela, C. Felbol, J. M. Cardemil, A. M. Guzmán, and R. A. Escobar, "Techno-economic analysis of a hybrid CSP+PV plant integrated with TES and BESS in Northern Chile," *AIP Conference Proceedings*, vol. 2033, no. November, pp. 1262–1277, 2018.

[173] M. Hummon, "Modelling Concentrating Solar Power with Thermal Energy Storage for Integration Studies," tech. rep., NREL, 2013.

[174] J. Remund, S. Müller, S. Kunz, B. Huguenin-Landl, C. Studer, D. Klauser, C. Schilter, and R. Lehnherr, *Meteonorm Handbook*. No. May, 2012.

[175] N. Hanrieder, M. Sengupta, Y. Xie, S. Wilbert, and R. Pitz-Paal, "Modeling beam attenuation in solar tower plants using common DNI measurements," *Solar Energy*, vol. 129, no. March 2018, pp. 244–255, 2016.

[176] R. P. Praveen, "Performance analysis and optimization of central receiver solar thermal power plants for utility scale power generation," *Sustainability (Switzerland)*, vol. 12, no. 1, 2020.

[177] R. Fu, D. Feldman, and R. Margolis, "U . S . Solar Photovoltaic System Cost Benchmark : Q1 2018," *Nrel*, no. Novmnber, pp. 1–47, 2018.

[178] IRENA, "Renewable Power Generation Costs in 2018," tech. rep., 2019.

[179] U.S. Energy Information Institution, "Annual Energy Outlook 2018 with projections to 2050," *Annual Energy Outlook 2018 with projections to 2050*, vol. 44, no. 8, pp. 1–64, 2018.

[180] R. Fu, T. Remo, R. Margolis, R. Fu, T. Remo, and R. Margolis, "2018 U . S . Utility-Scale Photovoltaics- Plus-Energy Storage System Costs Benchmark," Tech. Rep. November, 2018.

[181] L. Goldie-Scot, "A Behind the Scenes Take on Lithium-ion Battery Prices," 2019.

[182] I. Staffell and R. Green, "How does wind farm performance decline with age?," *Renewable Energy*, vol. 66, pp. 775–786, jun 2014.

[183] X. Han, L. Lu, Y. Zheng, X. Feng, Z. Li, J. Li, and M. Ouyang, "A review on the key issues of the lithium ion battery degradation among the whole life cycle," *eTransportation*, vol. 1, p. 100005, aug 2019.

[184] M. Röger, E. Lüpfert, S. Caron, and S. Dieckmann, "Techno-economic analysis of receiver replacement scenarios in a parabolic trough field," in *AIP Conference Proceedings*, vol. 1734, p. 030030, 2016.

[185] R. V. Padilla, *Simplified Methodology for Designing Parabolic Trough Solar Power Plants*. PhD thesis, 2011.

[186] M. Wetter, "Generic Optimization Program," in *Energy*, no. c, pp. 1998–2009, 2009.

[187] J. Kennedy and R. Eberhart, "Particle swarm optimization," in *Proceedings of ICNN'95 - International Conference on Neural Networks*, vol. 4, pp. 1942–1948, IEEE, 2016.

List of Figures

List of Tables

Nomenclature

Acronyms

CRS	Central receiver system
CSP	Concentrated solar power
DNI	Direct Normal Irradiance (W/m^2)
EES	Electric energy storage
EPC	Engineering procurement and construction cost
GHI	Global horizontal radiation (kW/m^2)
$HRES$	Hybrid renewable energy system
$LCOE$	Levelized cost of electricity (c$/kWhe)
$MENA$	Middle East and North Africa
OM	Operation and Maintenance costs (c$/kWhe)
PB	Power Block
PTC	Parabolic through collector
PV	Photovoltaic modules
SF	Solar Fraction
SM	Solar Multiple (-)
TES	Thermal energy storage

W	Wind turbines
EIA	U.S. Energy Information Administration
LT	Life time

Greek symbols

α	Azimuthal position (rad)
Δ	Difference/Increment
η	Efficiency
ρ	Mirror reflectivity
σ	Standard error deviation
θ	Incident angle of sunrays on heliostat surface and azimuthal angle of the receiver mesh point
ε_T	Elevation angle of the reflected beam (rad)

Nomenclature

$\vec{n}$	Normal to the heliostat surface
$\vec{S}$	Vectors pointing to the sun from the heliostat center
$\vec{T}$	Vectors pointing to the receiver surface from the heliostat center
A	Area (m^2)
a	Heliostat dimension at receiver plane (m)
BR	Radius of the reflected beam (m)
C	Capital cost ($)
D	Diameter (m)
d	Distance (m)
DH	Heliostat diagonal (m)
DM	Heliostat horizontal projection (m)
dR	Ratio coefficient of ΔR and DM
E	Energy (kWh)
f	Optical factor
H	Height (m)

h	Convective coefficient (W/m^2K) or Hours of tank
HX	Heat exchanger
I	Current
i	Interest rate
lm	Heliostat Height (m)
N	Number of heliostats (-)
Ny	Years of lifetime
P	Nominal power (MW)
p	Penalty
R	Radius/Radial (m)
$Tank$	Tank level (%)
V	Voltage
wm	Heliostat Width (m)
zR	Vertical displacement of the aiming point

Subscript

abs	Absorbed
AC	Alternating current
ann, w	Annual weighted
att	Atmospheric attenuation factor
$coll$	Collected
cos	Cosine effect
DC	Direct current
dem	Demand
e	Total deviation
el	Electric
f	Fixed
fc	Forced convection

$field$	Heliostat field
h	Heliostat
hr	Slant range
i	Group
inc	Incident
ind	Industrial
k	Aim factor
m^2	Square meter
min	Minimum
mix	Mixed natural and forced convection
mpp	Maximum power point
nc	Natural convection
oc	Open circuit
opt	Optical heliostat
PB	Power block
$Plant$	Total CRS system
rad	Radiative
rec	Receiver
res	Residential
sb	Shadowing and blocking
sc	Short circuit
sep	Security
slp	Mirror slope
$spill$	Interception/ spillage
sun	Sun-shape
t	Tower
trk	Tracking
v	Variable